AIX-MARSEILLE UNIVERSITÉ

ECOLE DOCTORALE 352

INSTITUT FRESNEL / UMR 7249

Thèse présentée pour obtenir le grade universitaire de docteur

Discipline : Physique et science de la matière
Spécialité : Optique, photonique et traitement d'image

Xavier AUDIER

Spectroscopie Raman stimulée rapide et imagerie hyperspectrale

Ultra-fast stimulated Raman scattering and hyperspectral imaging.

Soutenue le 13/12/2018 devant le jury composé de :

Randy A. BARTELS, Ph.D.	Colorado State University	Rapporteur
Thomas R. HUSER, Ph.D.	University of Bielefeld	Rapporteur
Nicolas FORGET, Ph.D.	Fastlite	Examinateur
Sophie BRASSELET, Ph.D.	Aix Marseille Univ	Examinatrice
Hervé RIGNEAULT, Ph.D.	Aix Marseille Univ	Directeur de thèse

Numéro national de thèse/suffixe local : 2018AIXM0580/078ED352

Résumé

En combinant des techniques de microscopie et de spectroscopie, il est possible de réaliser des images résolues spectralement. Ces images apportent des réponses à de nombreux problèmes en chimie, biologie, et médecine. La diffusion Raman cohérente (CRS) s'est révélée capable de surpasser la diffusion Raman spontanée dans l'analyse chimique d'échantillons, en offrant une meilleure résolution spatiale et un temps d'acquisition plus faible. La vitesse d'acquisition de l'information spectrale demeure toutefois un facteur limitant en imagerie CRS, et de nombreuses recherches se concentrent sur le développement de nouvelles méthodes d'acquisition. Le présent travail s'inscrit dans cette démarche. En combinant la diffusion Raman stimulée (une branche de la CRS), la focalisation spectrale d'impulsions optiques, ainsi qu'une ligne à délai acousto-optique, nous réalisons les premières mesures à de telles vitesses d'acquisition. Le cadre théorique, technologique, ainsi que l'ingénierie nécessaire pour parvenir à ce résultat sont détaillés. Cette technique d'acquisition rapide est illustrée par le suivi de réaction chimique, le contrôle qualité pharmaceutique, en biologie, et en histologie.

Mots clés : Spectroscopie Raman Stimulée, Imagerie hyperspectrale, Ligne à délai acousto-optique.

Abstract

Combining microscopy and spectroscopy, one can achieve spectrally resolved imaging, and provide a solution to various chemical, biological, or medical challenges. Coherent Raman Scattering (CRS) has proven extremely valuable in providing chemical information, with a higher resolution and shorter acquisition time than spontaneous Raman scattering. The acquisition rate of the spectral information from a sample remains the limiting factor of CRS imaging, and several experimental schemes are being investigated to push the technology toward higher imaging frame rates. This work develops one such scheme. Combining Stimulated Raman Scattering (a CRS technique), spectral focusing with chirped pulses, and a fast acousto-optic delay line, we achieved unprecedented spectral acquisition rates. The theoretical, technological, and engineering frameworks enabling such acquisition are described in details. The application to pharmaceutical quality control, time resolved chemical transformations, biology, and histology are demonstrated.

Keywords: Stimulated Raman Spectroscopy, Hyperspectral imaging, Acousto-optic delay line.

Contents

List of Figures

List of Tables

1 Introduction

1.1 Motivation

1.1.1 Colors and spectroscopy

Numerous species across the animal kingdom possess various types of photo-receptor cells, from which they gain the ability to detect and discriminate different optical wavelengths. The most complex visual system ever discovered is that of the mantis shrimp. With 12 to 16 different types of photo-receptor cells, a mantis shrimp can perceive wavelengths ranging from deep ultraviolet to far red, and even sense light polarization. The reasons for such complex visual functions are not yet understood, but the variability across species is usually correlated with their evolutionary pressure. Humans, for instance, usually have three types of photo-receptor cells sensitive to what we refer to as visible light. The evolution of this trait in humans may be correlated with the evolution of specific colored fruits in tropical forests [1]. As the ancestors of modern monkeys, apes, and humans switched to diurnal activity and began consuming fruits and leaves from flowering plants, this color sensitivity may have provided evolutionary advantages. With the ability to discriminate between millions of colors, our visual system not only provides spatial information about our environment, but additionally performs basic spectroscopic imaging with visible light. Given a certain context, we can therefore easily recognize certain molecules based on their color, assuming they have a color.

This color sensitivity is rendered insufficient when analyzing molecules that do not absorb visible light which occurs with most molecules. Biological molecules do not have specific absorption spectra in the visible range, apart from a few exceptions such as pigments or hemoglobin, and it is impossible to identify them with such light. With infrared light, however, one can probe vibrational energies of molecules and obtain a very specific spectroscopic signature for each molecular bond. With such information, one can retrieve the equivalent of color vision in the infrared range. The ability to perform spectroscopic imaging is extremely valuable in various fields, in particular when imaging biological samples.

1.1.2 Bioimaging

Looking at thin biological samples under an optical microscope usually provides a gray scale image with limited contrast. This type of sample is mostly transparent, as small light-scattering structures produce most of the information that can be retrieved. White light microscopy is usually sufficient to image individual cells, but fails to provide high quality images in denser tissues. Even

if some structural information can be retrieved, such images lack the chemical information that is necessary in most biological applications.

One needs a contrast mechanism to retrieve adequate chemical information and to differentiate chemical species. Conventionally, microbiologists use some form of label such as dyes, stains, or fluorescent labels. Fluorescent labeling adds foreign chemical species that have specific optical properties. These chemicals will co-localize with the molecules that needs to be imaged and provide critical information such as its position. This technique is used routinely in biological analysis. Despite their efficacy, contrast dyes generally require thorough fixation and time-consuming preparation of samples which renders them incompatible with performing live imaging. Our work investigates vibrational imaging as an alternative way to analyze biological samples as it provides both chemical and structural information that can exceed that of chemical labeling. We illustrate this technique in the context of histology.

1.2 Histology

Histology is the branch of medicine focused on the study of biological tissues. Biological tissues are the way in which cells of varying types are organized locally to compose an organ. Histology is of particular importance to the study of cancer and in cancer diagnosis. In cancerous formations of tissues, or tumors, the tissue structure is locally altered from a well-organized cellular matrix.

1.2.1 Gold standard

The current gold standard for cancer detection is a biopsy combined with histological diagnosis [2]. For biopsy, a physician must excise the tissue under investigation. This tissue sample is then frozen, or embedded, in a polymer matrix which provides rigidity for slicing and analysis of the sample. Sample slices are then processed with stains which help reveal the chemical composition of the tissue: typically Hematoxylin (a violet, positively charged stain) and Eosin (a pink, negatively charged stain) (H&E). Hematoxylin will bind easily to negatively charged molecules, such as DNA, and label the nuclei of the cells in violet. Eosin similarly will bind easily to positively charged amino acid side chains and therefore stain most of the cytoplasm and membranes of the cells, giving them a light pink color. By analyzing H&E images, a histopathologist will judge the level of organization of the tissue, the number of dividing cells, and other factors, to establish a diagnosis.

1.2.2 Limitations

Even though histology has been a well established standard for 200 years, it suffers from a lot of drawbacks. The most limiting factor of histological analysis and biopsy of tissues is that the process is heavily invasive. Additionally, histological analysis and biopsy are time-consuming. The full procedure takes on average 16 hours and requires multiple steps for staining. Such limitations restrict the practicality of this method clinically and otherwise. In particular, it cannot be used during surgical biopsies or excisions of tumors to identify tumor margins or obtain a prognostic diagnosis.

Additionally, there is a finite amount of information that can be obtained with H&E staining. The dyes have affinities for positively and negatively charged molecules, but do not allow for much more quantitative information. The metabolism and chemical composition of cancer cells can differ significantly from that of healthy cells. A wide variety of molecular species could be monitored and imaged to provide a richer diagnosis than that obtained by solely imaging nuclei and cell bodies [2].

Spectroscopic imaging would represent a massive improvement in technique, due to the limited information yield of histology, the variability in laboratory protocols, and the subjective quality of data which mostly relies on the experience of the pathologist.

1.3 Spectroscopic imaging

1.3.1 Infrared imaging

Biological molecules usually do not absorb visible light and consequently appear transparent under a standard optical microscope. However, by using infrared light we can detect absorption at certain frequencies that are characteristic of the rotational and vibrational modes of each molecule. This provides more extensive information on the molecular bonds present in the molecules and about their chemical composition.

Although analysis with infrared light is more powerful, it has several critical drawbacks that make it impractical for biological imaging.

First, the wavelength of interest for IR absorption spectroscopy ranges from $3\,\mu\mathrm{m}$ to $20\,\mu\mathrm{m}$, taking into account vibrational modes only. Optical setups with such wavelengths are particularly cumbersome, with cooled detectors and metal alloys optics. Additionally, water has a non-zero absorption across the whole range of IR frequencies. Considering the prevalence of water molecules in biological samples, it is impossible to measure an IR absorption signal from such sample, other than that of water, without first dehydrating it. Furthermore, the highest imaging resolution that can be obtained via IR is of several microns, which is insufficient for bio-imaging.

1.3.2 Spontaneous Raman spectroscopy

To circumvent the problems faced by IR absorption spectroscopy, vibrational spectroscopy is usually performed in an indirect way through Raman spectroscopy.

Raman and co-workers discovered spontaneous Raman scattering in the 1920s[3] which has provided scientists with a way to elucidate vibrational modes of molecules using visible light. By illuminating a sample with visible light, one can detect a small fraction of inelastically scattered light at a higher wavelength. The energy difference between the incoming and the scattered photons corresponds to the energy absorbed by the molecules during a vibration transition. Therefore, by using monochromatic light and analyzing the spectrum of the scattered light, one can retrieve the vibrational spectrum of the molecules without having to dry or fixate a sample. Such imaging is most relevant to chemical labeling as it does not interfere with biological functions and can be performed on live tissues. In theory, spontaneous Raman imaging is a suitable candidate for chemical imaging of biological samples.

Experimentally, the Raman process is inefficient. The Raman cross section is typically of $10^{-30}\ \mathrm{cm}^2$ per molecule, around 10^{11} less efficient than IR absorption. The time required to obtain a suitable Raman spectrum can be tens or hundreds of milliseconds, which means a single image can take minutes to hours to acquire. This acquisition time makes the live imaging of dynamic processes impossible with such a technique, and, within the context of histology, the additional chemical information provided by spontaneous Raman imaging is not sufficient to compensate for such a low acquisition speed.

1.3.3 Coherent Raman Scattering (CRS)

Two complementary techniques have been developed : Coherent Anti-Stokes Raman scattering (CARS) and Stimulated Raman scattering (SRS) as solutions to the inefficiency of analysis with spontaneous Raman scattering. By using nonlinear optics, one can drive the vibrational modes coherently and increase the Raman signal by several orders of magnitude. A classical picture of both spontaneous and coherent Raman scattering will be described in chapter 2. Microscopic analysis systems based on these two schemes have been developed and are starting to be used to tackle biologically relevant problems [4].

CARS and SRS each involve two types of lasers : a pump laser at angular frequency ω_p, and a Stokes laser at ω_s. When their electric fields arrive simultaneously on a sample, the beat frequency of the two lasers $\Omega = \omega_p - \omega_s$ can drive the molecules in the sample to oscillate at a vibrational resonance. Once driven, the oscillating molecules can effectively interact a second time with the electric field to: a) generate a new optical frequency through CARS or b) convert a pump photon into a Stokes photon via SRS. The strength of these two coherent Raman processes is dependent on the presence of a molecular vibration resonance, so

that a vibrational spectrum can be acquired by probing multiple values of Ω.

1.3.4 Historical Review

The discovery of Coherent Anti-Stokes Raman scattering (CARS) took place in 1965 at Ford Motor Company [5] but the name wasn't coined until 10 years later by Begley and co-workers [6] . The first CARS microscope was built in 1982 by Duncan et al [7]. Later, in 1999, the scientific community regained interest in CARS when Zumbusch and co-workers built the first Coherent Raman microscope using two synchronized femtosecond lasers with high repetition-rates, collinear beams, and tight-focusing geometry [8].

In 2005, CARS imaging reached video-rate [9] and is still being improved upon in order to obtain faster images and greater spectral information. Although the CARS spectrum contains the same information that the SRS spectrum does, the non-resonant background distorts the CARS spectrum and makes retrieval of spectral information less straightforward.

SRS was discovered in 1962, prior to CARS [10]. Only in 2007 with the work of Ploetz et al., was SRS used for imaging with spectral resolution [11]. SRS comes in the form of a small gain (respectively loss) of photons in the probe (resp. pump) field. The relative intensity change, which is usually very minor ($\approx 10^{-6}$) is typically detected through amplitude modulation of one beam and lock-in amplification of another. This aspect will be covered in further detail in chapters 2 and 3.

CARS and SRS can be implemented simultaneously and each provide different advantages to a range of specific applications. In order to choose which system will be the most beneficial for analysis, one must weigh each system's strengths and weaknesses.

Quantitative analysis of a spectrum with CARS can be difficult due to its non-resonant background. Additionally, its signal depends quadratically on the concentration of molecules which further complexifies the quantitative analysis. The SRS system can also contain artifacts such as cross-phase modulation, transient-absorption, or photo-thermal effects [12]. Additionally, SRS detection is usually limited to the forward direction whereas CARS can provide decent signal in the epi direction. Overall, it is a simpler process to perform spectral measurements with broadband CARS than with broadband SRS since CARS photons can be detected directly with a spectrometer, while the SRS spectrum requires additional optical or electronic schemes to be retrieved.

1.3.5 Hyperspectral CRS microscopy

When probing a single Raman line, or a single vibrational frequency, one can obtain CARS images at video rates which illustrates the feasibility of live vibrational imaging and insinuates the possibility of further applications of the

technology. However, in order to obtain chemically relevant information, it is often necessary to simultaneously acquire multiple spectral components. Recent research efforts have been oriented towards increasing the amount of spectral information that can be obtained, while keeping the imaging speed as fast as possible.

There are three different ways to acquire spectral information using CARS and SRS. The first method consists of acquiring individual images sequentially at each Raman frequency. Using two synchronized picosecond lasers, one can selectively probe a Raman line with a resolution of a few wavenumbers (cm^{-1}). Changing the probed wavenumber implies changing one of the laser's frequencies, which is one major issue with this type of system. A change in laser frequency typically takes at least a few seconds and is not suitable to provide fast imaging. Another option to acquire spectral information is to combine two lasers, one with a large spectral range and a second with a short one. This process allows multiple vibrational modes to be excited simultaneously. A third, more common, way of proceeding is to use two lasers each with a large spectral range, but to add dispersion on the two pulses. This approach, called Spectral Focusing, recovers spectral resolution while making spectral scanning much more efficient than with narrow-band pulses. These 3 imaging schemes have been explored in depth, particularly over the past few years [13].

This manuscript and such research in nonlinear optics takes place in this context, as increasing technological advances are pushing coherent Raman to provide accelerated spectral imaging. This PhD studies Stimulated Raman Scattering by using two femtosecond pulses and recovering spectral information via spectral focusing. We will mainly study the Raman region around 2800 to $3100\,\mathrm{cm}^{-1}$, also referred to as the lipid band or CH-stretch region. This work aims to build the fastest SRS microscope with spectral resolution in order to obtain high quality and chemically resolved images of biological samples.

1.4 Manuscript outline

Chapter 2 provides the theoretical framework to understand the generation and detection of the SRS signal.

Chapter 3 focuses on understanding the signal to noise ratio in SRS from a theoretical and experimental point of view. Shot noise limited measurements are demonstrated, as well as several noise characterization procedures for SRS systems.

Chapter 4 describes in detail the spectral focusing technique. The spectral resolution and signal drop associated with the technique are modeled for our laser systems and demonstrated experimentally.

Chapter 5 introduces the fast delay line that will be used to increase the spectral acquisition speed.

Chapter 6 presents the main achievements of this work. We demonstrate unprecedented acquisition speed for spectrally resolved SRS in the lipid band. This technique is illustrated in the context of histology, pharmaceutical quality assessment, and dynamical processes in biology and chemistry.

2 Theory of SRS

The main focus of this work is the use of nonlinear optics, in particular stimulated Raman scattering. Ultimately, the goal is to image the spatial distribution of molecules using only light, while using a contrast mechanism to identify them. The fundamentals of light matter interactions are required to understand how and why stimulated Raman scattering provides a chemical contrast mechanism.

In this chapter, the elementary model for light matter interactions is introduced in the form of the elastically bound electron, also referred to as the Lorentz Oscillator. The effect of coupling between the electronic oscillations and the molecular vibration modes is illustrated while maintaining a classical description of light and matter. Here, various spectroscopic methods are derived: spontaneous Raman scattering, IR absorption, and coherent Raman scattering. Finally, Stimulated Raman Scattering is described in further detail. In the following chapters, we will assume the reader has a general understanding of this technique, and detail further its signal, noise, and detection scheme.

This chapter's content is predominantly based on preexisting research, as the theory of light matter interactions has been well established for over half of a century. This chapter revisits the different elements of light matter interactions, to establish the background for the rest of this work. The elements of SRS theory have been mainly derived from the book *Coherent Raman Scattering Microscopy* [4] as well as a tutorial article from Hervé Rigneault and Pascal Berto [14]. For the purpose of accessibility, only a classical description of matter and electromagnetic fields is developed here. Semi classical and quantum descriptions of matter and field have been derived in other work and will not be discussed here.

2.1 Harmonic oscillator

The simplest description one can make of matter is a set of positive and negative charges attracting one another. First, we consider a hydrogen atom seen as a Lorentz Oscillator, in one dimension (Figure 2.1).

2.1.1 Perfect oscillator

The atom consists of a positively charged (q) proton and a negatively charged ($-q$) electron. Since a proton is more massive than the electron by three orders of magnitude, we will consider that the proton is stationary, and call m the mass of the electron.

The electron is bound to the atom at a certain equilibrium distance x_0. Around the equilibrium position we make the approximation that the electron-proton

interaction will obey Hooke's law:

$$F_k = -kx(t) \tag{2.1}$$

By applying the fundamental principle of dynamics to the electron, we obtain the harmonic oscillator equation:

$$\frac{\mathrm{d}^2x}{\mathrm{d}t^2} + \omega_0^2 x = 0 \tag{2.2}$$

with the system resonant angular frequency $\omega_0 = \sqrt{k/m}$.

2.1.2 Damped oscillator

We now consider that the electron loses energy over time, and consequently we introduce a friction force:

$$F_\gamma = -2m\gamma\frac{\mathrm{d}x}{\mathrm{d}t} \tag{2.3}$$

Equation 2.2 now becomes:

$$\frac{\mathrm{d}^2x}{\mathrm{d}t^2} + 2\gamma\frac{\mathrm{d}x}{\mathrm{d}t} + \omega_0^2 x = 0 \tag{2.4}$$

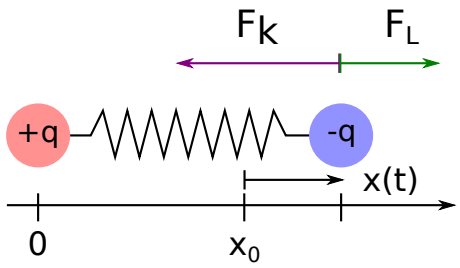

Figure 2.1 – Simple description of the hydrogen atom.

2.1.3 Driven oscillator

Light matter interactions relies on the electromagnetic force. A charge q with velocity $\vec{v}$ placed in an electromagnetic field $(\vec{E}, \vec{B})$ will be subject to the Lorentz force:

$$\vec{F_L} = q(\vec{E} + \vec{v} \times \vec{B}) \tag{2.5}$$

We restrict ourselves to studying the effect of the electric field, which is assumed to be aligned with the oscillator. Light is an oscillating electrical field,

therefore we take E to be of the form:

$$E(t) = 2A_p \cos(\omega_p t) \tag{2.6}$$

with ω representing the angular frequency of the field. For convenience, we use the complex notation ($\star$ represents the complex conjugate):

$$E(t) = A_p e^{-i\omega_p t} + A_p^\star e^{i\omega_p t} \tag{2.7}$$

The Lorentz force applied to the electron becomes:

$$F_L = -qE(t) = F_p e^{-i\omega_p t} + F_p^\star e^{i\omega_p t} \tag{2.8}$$

and Equation 2.4 becomes:

$$\frac{\mathrm{d}^2 x}{\mathrm{d}t^2} + 2\gamma \frac{\mathrm{d}x}{\mathrm{d}t} + \omega_0^2 x = \frac{F_p}{m} e^{-i\omega_p t} + \frac{F_p^\star}{m} e^{i\omega_p t} \tag{2.9}$$

We look for solutions through their Fourier transform $x(t) = \int x(\omega) e^{-i\omega t} \mathrm{d}\omega$. By replacing the solution in the previous equation we find the amplitude of the oscillations to be:

$$x(\omega) = \frac{1}{m} H(\omega) \Big(F_p \delta(\omega - \omega_p) + F_p^\star \delta(\omega + \omega_p) \Big) \tag{2.10}$$

with:

$$H(\omega) = \frac{1}{\omega_0^2 - \omega^2 - 2i\gamma\omega} \tag{2.11}$$

This displacement of charges corresponds to the creation of an electric dipole moment:

$$p(t) = -qx(t) \tag{2.12}$$

The field radiated by this dipole moment is called the Rayleigh scattering.

2.1.4 Polarization

Although it is interesting to look at a single charge and how it interacts with light to create an induced dipole, our analyses typically involve an ensemble of many dipoles.

With the effective medium approximation, we can define the density of dipoles P by adding n dipoles per unit volume:

$$P(t) = np(t) \tag{2.13}$$

with Equations 2.10 and 2.12 we get:

$$P(\omega) = \frac{nq^2/m}{\omega_0^2 - \omega^2 - 2i\gamma\omega} E(\omega) \tag{2.14}$$

also written as

$$P(\omega) = \epsilon_0 \chi(\omega) E(\omega) \tag{2.15}$$

with $\chi(\omega)$ the susceptibility of the material:

$$\chi(\omega) = \frac{\omega_p^2}{\omega_0^2 - \omega^2 - 2i\gamma\omega} \tag{2.16}$$

and:

$$\omega_p = \sqrt{\frac{nq^2}{\epsilon_0 m}} \tag{2.17}$$

2.1.5 Frequency analysis

In the simple picture that is described here, the polarization of the medium will be proportional to the electric field with a complex proportionality factor $\chi(\omega)$. This factor can be expressed as $\chi(\omega) = \rho(\omega)e^{i\phi(\omega)}$ where ρ represents the gain and ϕ the phase lag.

Under the condition that the damping effect is not too high ($\gamma \ll \omega_0$) the gain ρ will only be significant around resonance ($\omega \approx \omega_0$) and can be neglected elsewhere. The linewidth of this resonance is 2γ.

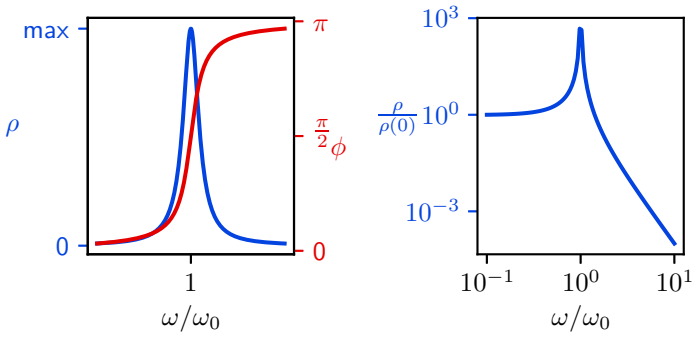

Figure 2.2 – Graphical view of the susceptibility assuming low damping. Left: Gain (ρ, blue) and Phase shift (ϕ, red) as functions of normalized angular frequency on a linear X-Y scale. Right: relative gain as a function of normalized angular frequency on a log-log scale. The model uses $\omega_0 = 1$ and $\gamma = 10^{-3}$

The driven harmonic oscillator can have three different behaviors depending on the driving frequency:

$\omega \ll \omega_0$: The oscillators are driven below the resonance, the motion of the dipoles will be oscillations of small amplitude, in phase ($\phi = 0$) with the incoming field.

$\omega = \omega_0$: The oscillators are driven at resonance, the motion of the dipoles will be oscillations of significant amplitude, in quadrature ($\phi = \pi/2$) with the incoming field.

$\omega \gg \omega_0$: The oscillators are driven past resonance, the motion of the dipoles will be oscillations of small amplitude, in opposition ($\phi = \pi$) with the incoming field.

2.2 Molecular vibrations

So far, this model provides an explanation of electronic resonances and Rayleigh scattering. It relies on electronic movements but does not take into account the fact that in the case of molecules, nuclear motion can be coupled with these electronic movements.

2.2.1 Simple classical model of a molecule

We now considering not an atom, but a molecule. This model serves as a purely educational resource. Here, spontaneous and coherent Raman are derived with a purely classical picture in order to illustrate the couplings that contribute to these phenomena. A purely classical picture is not sufficient or extensive enough to represent the reality of the interactions happening inside a molecule (or between a molecule and an electric field). A more rigorous model of light matter interactions has been previously derived by Eric Olaf Potma and Shaul Mukamel [4].

For simplification purposes, we picture the molecule as having a nuclear oscillator, meaning the nuclei of the molecule create a total charge $+q$ and effective mass M. This mass is bound to the center of mass of the molecule, at a distance $X_0 + X$, where X_0 is the equilibrium position. We add a damping term to this oscillator with the constant Γ as with the previous model. This nuclear charge is subject to several forces such as the external force from the electric field $F = +qE(t)$ and the potential force $F_1(x, X)$. We consider electronic charges q, of mass m, to be bound to the molecule from its center of mass at a distance $x_0 + x$, where x_0 is the equilibrium position. The forces applied to the electronic charges are the coulomb force $F = -qE(t)$, and the potential force $F_2(x, X)$.

With this model, we can easily write the equations for $x(t)$ and $X(t)$:

$$M\ddot{X} + 2\Gamma\dot{X} = +qE(t) + F_1(x, X) \tag{2.18}$$

$$m\ddot{x} + 2\gamma\dot{x} = -qE(t) + F_2(x, X) \tag{2.19}$$

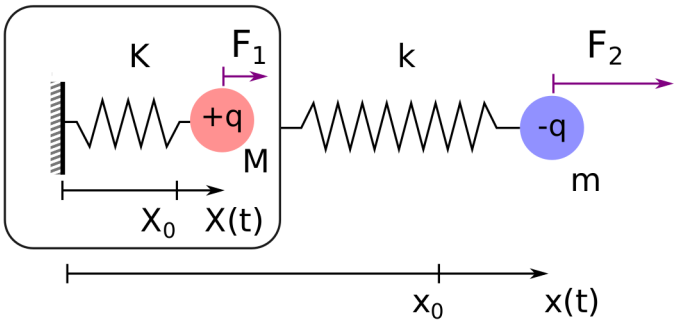

Figure 2.3 – Simplified model of a molecule. The nuclear charges are treated as an oscillator bound to the center of mass. The electronic charges are treated in the same way. The forces acting of the positive and negative charges are a function of the electric field as well as the position of the charges.

The next sections derive spontaneous Raman and coherent Raman scattering by developing the expression of F_1 and F_2.

2.2.2 Introduction to spontaneous Raman

We consider that the movement of the nuclear charges X and that of the electronic charges x are small. This allows one to expand the potential forces to the second order in x and X:

$$\begin{aligned} F_1(x,X) &= F_1(0,0) + x\frac{\partial F_1}{\partial x}|_{0,0} + X\frac{\partial F_1}{\partial X}|_{0,0} \\ &\quad + \frac{1}{2}[x^2\frac{\partial^2 F_1}{\partial x^2}|_{0,0} + xX\frac{\partial^2 F_1}{\partial x \partial X}|_{0,0} + X^2\frac{\partial^2 F_1}{\partial X^2}|_{0,0}] \\ F_2(x,X) &= F_2(0,0) + x\frac{\partial F_2}{\partial x}|_{0,0} + X\frac{\partial F_2}{\partial X}|_{0,0} \\ &\quad + \frac{1}{2}[x^2\frac{\partial^2 F_2}{\partial x^2}|_{0,0} + xX\frac{\partial^2 F_2}{\partial x \partial X}|_{0,0} + X^2\frac{\partial^2 F_2}{\partial X^2}|_{0,0}] \end{aligned}$$

These expansions can be simplified by noting that the forces are null at the equilibrium $(x = 0, X = 0)$, and by renaming the partial derivatives using variable names δ and η:

$$F_1(x,X) = \delta_x x + \delta_X X + \delta_{xx}x^2 + \delta_{xX}xX + \delta_{XX}X^2 \quad (2.20)$$

$$F_2(x,X) = \eta_x x + \eta_X X + \eta_{xx}x^2 + \eta_{xX}xX + \eta_{XX}X^2 \quad (2.21)$$

Using this second order expansion, the model becomes:

$$M\ddot{X} + 2\Gamma\dot{X} = +qE(t) + \delta_x x + \delta_X X + \delta_{xx}x^2 + \delta_{xX}xX + \delta_{XX}X^2 \tag{2.22}$$

$$m\ddot{x} + 2\gamma\dot{x} = -qE(t) + \eta_x x + \eta_X X + \eta_{xx}x^2 + \eta_{xX}xX + \eta_{XX}X^2 \tag{2.23}$$

The elastic terms binding the nuclear charges $\delta_X = -K$ and electronic charges $\eta_x = -k$ are essential for their oscillatory behavior. The linear coupling terms δ_x and η_X are not essential in this derivation: Nuclear motion happens at low frequency, so the effect on the electrons through η_X will not be seen at high frequency and is negligible in this case. Similarly, the electrons are driven at high frequencies, so they will not drive the nuclear charges through linear coupling δ_x which renders this term irrelevant as well. However, δ_x will be relevant when discussing stimulated Raman.

To derive spontaneous Raman, we can neglect most nonlinear terms. The only required term is the nonlinear coupling of nuclear motion onto electronic motion $\eta_{xX} \neq 0$. A common way of interpreting this coupling is to see this term as the nuclear motion modifying the electronic elastic constant k. Finally, we will assume that the nuclear charges are driven at resonance with a small force $f(t) = a_0 e^{-i\Omega_R t} + c.c.$ (c.c. is the complex conjugate of the previous term). This small driving force is required to mimic the fact that any quantum oscillator will always have a non-zero energy. The amplitude a_0 will also give its phase to the nuclear oscillation which will be essential in following calculations.

With these assumptions, the Equations 2.22 and 2.23 become:

$$M\ddot{X} + 2\Gamma\dot{X} + KX = +qE(t) + f(t) \tag{2.24}$$

$$m\ddot{x} + 2\gamma\dot{x} + kx = -qE(t) + \eta_{xX}xX \tag{2.25}$$

To solve these equations it is easier to write them in the Fourier space. When doing so the product of x and X becomes a convolution $\otimes$:

$$X(\omega) = G(\omega)\left(\frac{q}{M}E(\omega) + a_0\delta(\omega - \Omega_R) + c.c.\right) \tag{2.26}$$

$$x(\omega) = H(\omega)\left(\frac{-q}{m}E(\omega) + \frac{\eta_{xX}}{m}[x \otimes X](\omega)\right) \tag{2.27}$$

and:

$$\begin{aligned}
\Omega_R &= \sqrt{K/M} \\
\omega_0 &= \sqrt{k/m} \\
G(\omega) &= \frac{1}{\Omega_R^2 - \omega^2 - 2i\Gamma\omega} \\
H(\omega) &= \frac{1}{\omega_0^2 - \omega^2 - 2i\gamma\omega}
\end{aligned}$$

We assume that the incident field is monochromatic, with an angular frequency ω_p much higher that the nuclear resonance Ω_R:

$$E(t) = A_p e^{-i\omega_p t} + c.c.$$

Under this assumption, the nuclear motion will not be affected by the electric field:

$$\begin{aligned}
\int_{-\infty}^{+\infty} G(\omega)E(\omega)e^{-i\omega t}\mathrm{d}\omega &= \int_{-\infty}^{+\infty} G(\omega)\Big(A_p\delta(\omega-\omega_p) + A_p^\star\delta(\omega+\omega_p)\Big)e^{-i\omega t}\mathrm{d}\omega \\
&= G(\omega_p)A_p e^{-i\omega_p t} + c.c. \\
&\approx 0 \qquad \text{when } \omega_p \gg \Omega_R
\end{aligned}$$

We can then neglect the effect of the electric field on the nuclear motion (i.e. the term $G(\omega)E(\omega)$ in Equation 2.26). The nuclear motion is then, more simply, a small oscillation at the resonant frequency, with a random phase:

$$\begin{aligned}
X(\omega) &= G(\omega)\Big(a_0\delta(\omega-\Omega_R) + a_0^\star\delta(\Omega_R-\omega)\Big) \\
X(t) &= \int_{-\infty}^{+\infty} X(\omega)e^{-i\omega t}\mathrm{d}\omega \\
&= 2|X_0|\cos(\Omega_R t + \phi)
\end{aligned}$$

where $|X_0|$ and ϕ are the modulus and argument of the complexe amplitude X_0:

$$X_0 = a_0 G(\Omega_R) \tag{2.28}$$

Next, we solve the equation of electronic motion. As is commonly done with such equations, we will approach the following solutions in a perturbative manner. Consequently, we will address the solution $x^{(0)}(t)$ without the coupling term, before introducing a small deviation $x^{(1)}(t)$ from this solution:

$$x(t) = x^{(0)}(t) + x^{(1)}(t) \tag{2.29}$$

with:

$$x^{(0)}(\omega) = H(\omega)\frac{-q}{m}E(\omega) \tag{2.30}$$

$$x^{(1)}(\omega) = H(\omega)\frac{\eta_{xX}}{m}[x^{(0)} \otimes X](\omega) \tag{2.31}$$

$x^{(0)}$ is precisely the electronic movement we found in Equation 2.10, and is a driven harmonic oscillator. $x^{(1)}$ will be a small correction due to coupling between nuclear modes and electronic modes :

$$x^{(1)}(\omega) = \frac{-\eta_{xX}}{m}H(\omega)\Big[X_0 x^{(0)}(\omega_p)\delta(\omega - \omega_p - \Omega_R) \tag{2.32}$$

$$+ X_0^\star x^{\star(0)}(\omega_p)\delta(\omega + \omega_p + \Omega_R) \tag{2.33}$$

$$+ X_0^\star x^{(0)}(\omega_p)\delta(\omega - \omega_p + \Omega_R) \tag{2.34}$$

$$+ X_0 x^{\star(0)}(\omega_p)\delta(\omega + \omega_p - \Omega_R)\Big] \tag{2.35}$$

In the time domain:

$$\begin{aligned} x^{(1)}(t) &= \int \mathrm{d}\omega x^{(1)}(\omega)e^{-i\omega t} \\ &= \frac{-q\eta_{xX}A_p}{m^2}\Big[H(\omega_p + \Omega_R)H(\omega_p)X_0 e^{-i(\omega_p+\Omega_R)t} + c.c. \\ &+ H(\omega_p - \Omega_R)H(\omega_p)X_0^\star e^{-i(\omega_p-\Omega_R)t} + c.c.\Big] \end{aligned}$$

In most experimental cases, the different electric fields are below the electronic resonance: $\omega_p, \omega_p \pm \Omega_R \ll \omega_0$. We can then simplify $H(\omega) \approx \omega_0^{-2}$. We note the phase of the nuclear oscillator ϕ. The movement of the electrons becomes:

$$x(t) = \frac{-2qA_p}{m\omega_0^2}\cos(\omega_p t) + \frac{-2\eta_{xX}|X_0|qA_p}{m^2\omega_0^4}\Big[\cos\Big((\omega_p+\Omega_R)t+\phi\Big)+\cos\Big((\omega_p-\Omega_R)t-\phi\Big)\Big] \tag{2.36}$$

With this simplified model, we can see that the coupling between nuclear motion and electronic oscillations leads to the generation of novel frequencies, such as $\omega_p - \Omega_R$ (Stokes) and $\omega_p + \Omega_R$ (Anti-Stokes) that were not present in the incoming field. The dipoles oscillating at these frequencies will generate an electric field (meaning photons) at different wavelengths than the incoming one. This provides an understanding of the spontaneous Raman scattering process, which is the most common way to perform molecular spectroscopy. One gains access to all frequencies Ω_R at which the Raman process occurs by sending monochromatic light ω_p on a sample and measuring the spectrum of the resulting scattered light. The analysis of the many molecular resonances leads to knowledge of the sample chemical composition. One can identify a molecule on the basis of its spe-

cific Raman spectrum, and additionally perform spectral imaging by measuring Raman spectra at different points on an heterogeneous sample.

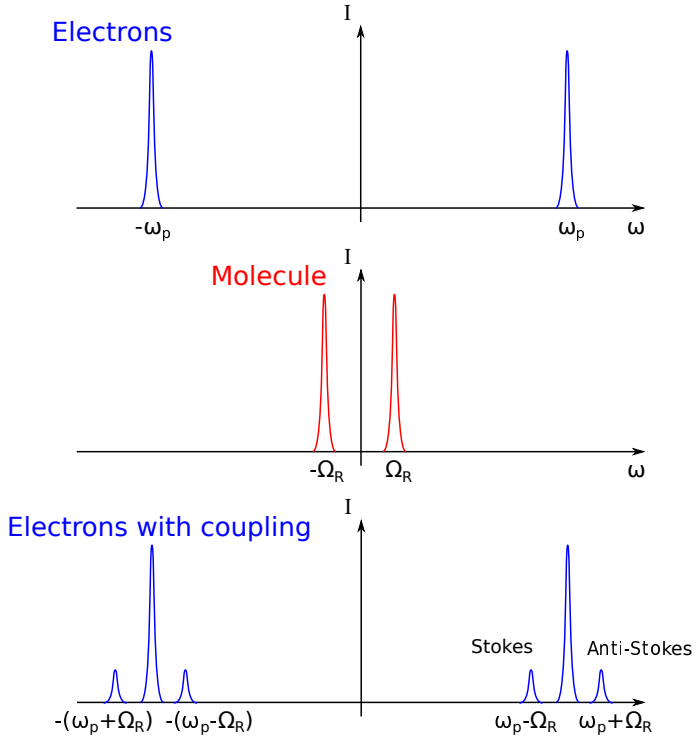

Figure 2.4 – Graphical solution to the coupled equations. The electrons are driven at frequency ω_p by the field. The molecule is oscillating at its resonance frequency Ω_R. The coupling term is the product of the two functions in time and is the convolution of the two functions in the frequency domain. The coupling is treated as a perturbation of the electronic movement, so we simply add it to the electronic movement to obtain the first order solution. We see the Stokes and Anti-Stokes frequency appear. This representation does not illustrate the phase of the fields or nuclear motion. The mathematical expression of the solution is necessary to take phases into account.

Strength and weakness of spontaneous Raman

Although spontaneous Raman is a powerful technique for molecular spectroscopy, it has several drawbacks. The main challenge to using spontaneous Raman is the lack of signal, or adequate number of scattered photons. The Raman cross section is limited, which means that, for an incoming set of photons, only a very small fraction will be scattered. In order to retrieve a proper signal to noise ratio, one would need to have an averaging time incompatible with live imaging. Additionally, spontaneous Raman is an incoherent process because the phase of

the molecular vibrations ϕ will be imprinted on the scattered field, as we can see from Equation 2.36. Since we do not probe single molecules, but molecule ensembles, the different fields scattered by each molecule will add incoherently on the detector. Coherent Raman scattering addresses this concept by ensuring that the molecular oscillators are all oscillating in phase. Consequently, the generated Raman signal from each oscillator will add coherently on the detector leading to a much higher signal.

2.2.3 Coherent Raman Scattering

We will now refine this model in order to illustrate the behaviors that are central to this work.

Referencing Equations 2.22 and 2.23, we are now interested in the case where the electronic motion is strong enough to take into account the nonlinear term $\eta_{xx}x^2$. We continue to neglect the nonlinear terms in nuclear motion and assume the nuclear motion to be small enough to neglect $\eta_{XX}X^2$.

The model becomes:

$$M\ddot{X} + 2\Gamma\dot{X} = +qE(t) + \delta_x x + \delta_X X \tag{2.37}$$
$$m\ddot{x} + 2\gamma\dot{x} = -qE(t) + \eta_x x + \eta_X X + \eta_{xx}x^2 + \eta_{xX}xX \tag{2.38}$$

As done previously, we rename the elastic constants $\delta_X = -K$ and $\eta_x = -k$ and move the elastic terms to the left side of the equation. We will forget about $\eta_X X$,since this contribution will only occur at low frequencies is not pertinent to the current case. In this section however we do not neglect $\delta_x x$ since it will be the driving force of the nuclear modes.

In the Fourier space, the Equations 2.37 and 2.38 become:

$$X(\omega) = G(\omega)\left(\frac{q}{M}E(\omega) + \frac{\delta_x}{M}x(\omega)\right) \tag{2.39}$$
$$x(\omega) = H(\omega)\left(\frac{-q}{m}E(\omega) + \frac{\eta_{xx}}{m}[x \otimes x](\omega) + \frac{\eta_{xX}}{m}[x \otimes X](\omega)\right) \tag{2.40}$$

To obtain a more accurate approximation of x that is simpler to compute, we can re-insert $x(\omega)$ from Equation 2.39 into itself, and neglect the higher order terms in η. We also simplify the equation by taking $H(\omega) = \omega_0^{-2}$.

$$x(\omega) = \frac{-q}{m\omega_0^2}E(\omega) + \frac{-q^2\eta_{xx}}{m^2\omega_0^6}[E \otimes E](\omega) + \frac{-q\eta_{xX}}{m^3\omega_0^4}[E \otimes X](\omega) \tag{2.41}$$

We treat the last term as a perturbation, therefore we write:

$$x(\omega) = x^{(0)}(\omega) + x^{(1)}(\omega) \tag{2.42}$$

with :

$$x^{(0)}(\omega) = \frac{-q}{m\omega_0^2}E(\omega) + \frac{-q^2\eta_{xx}}{m^3\omega_0^6}[E \otimes E](\omega) \tag{2.43}$$

$$x^{(1)}(\omega) = \frac{-q\eta_{xX}}{m^2\omega_0^4}[E \otimes X](\omega) \tag{2.44}$$

and $$X(\omega) = G(\omega)\left(\frac{q}{M}E(\omega) + \frac{\delta_x}{M}x^{(0)}(\omega)\right) \tag{2.45}$$

We can derive the solution of these equations, but a graphical approach gives a better understanding (Figure 2.5). In the case of coherent Raman scattering, we focus two lasers at two different frequencies ω_p and ω_s: The electric field contains frequencies $\pm\omega_p$ and $\pm\omega_s$. The electrons of the molecule will have a linear response to the field, and therefore contain frequencies $\pm\omega_p$ and $\pm\omega_s$ as well, which are in phase with the electric field.

Due to the nonlinearity in the electronic response, the electronic motion will also contain frequencies $\pm(\omega_p \pm \omega_s)$. In particular, $\pm(\omega_p - \omega_s)$ will be at relatively low frequencies.

The nuclear charges are only sensitive to frequencies at, or below Ω_R. Therefore, the contribution of the electric field and the linear response of the electrons will not drive the nuclear charges as their frequency is too high. However, as previously mentioned, the nonlinear response of the electrons can be at low frequencies $\pm(\omega_p - \omega_s)$.

For the case where $\omega_p - \omega_s = \Omega_R$, the nuclear charges are driven at resonance which leads to a strong nuclear motion $X(t)$ in quadrature with the driving electric field. The strong nuclear motion can now couple back into the electronic motion, just like previously in the case of spontaneous Raman scattering, and generate new frequencies in the electronic motion at $\omega_p \pm \Omega_R$ and $\omega_s \pm \Omega_R$. In other terms: $\omega_s - \Omega_R$, ω_s, ω_p, and $\omega_p + \Omega_R$.

As the frequencies $\omega_s - \Omega_R$ and $\omega_p + \Omega_R$ are not present in the incoming electric field, new photons will be generated at these frequencies and can be spectrally separated from the incoming lasers. This generation of new photons which can be spectrally separated is the basis of Coherent Stokes and Anti-Stokes Raman Scattering (CSRS and CARS) respectively. CARS photons have a higher energy than either the pump or Stokes photons. This makes their detection much easier than that of CSRS photons, and only CARS is used in vibrational imaging.

The frequencies ω_s and ω_p generated through electronic coupling with the nuclear resonance are already present in the incoming electric field. It is important to note that the phase of the nuclear motion is related to that of the electric fields, because it is driven by them.

This is the basis of stimulated Raman gain (SRG) and stimulated Raman loss (SRL), two complementary schemes that allow the measurement of a nuclear resonance by measuring gain or loss of photons. Quantitatively, the resonance

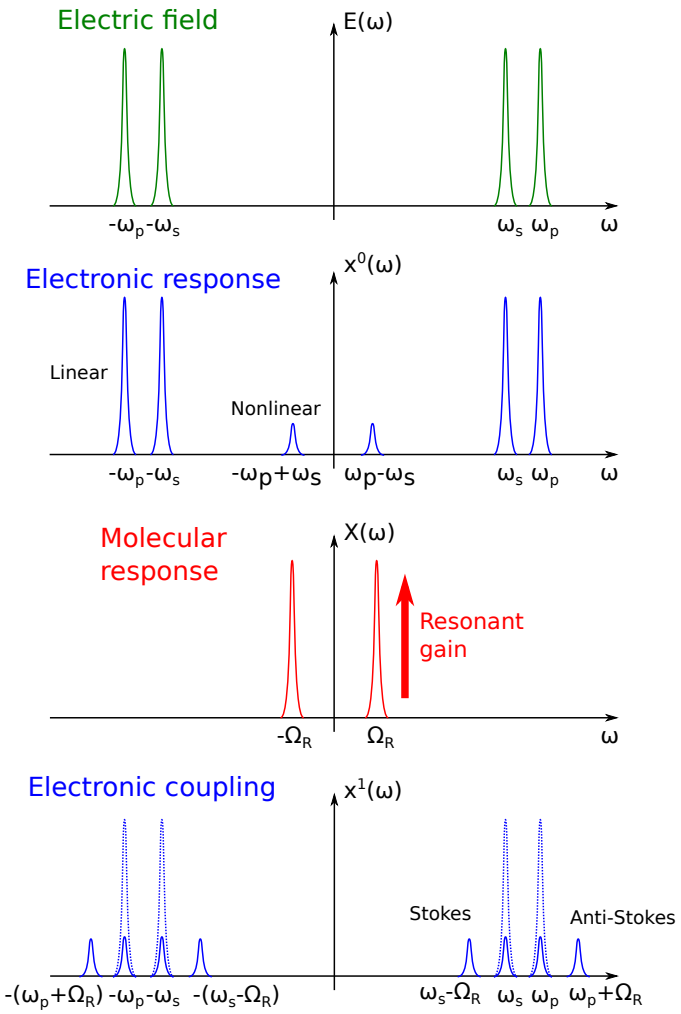

Figure 2.5 – Graphical solution to the coupled equations. The nonlinearity in the electronic response generates a low frequency component at the beating frequency of the two incoming fields. This low frequency can drive the nuclear motion at resonance. The nuclear oscillation can couple back into the electronic motion as described with spontaneous Raman scattering, in this case with a well defined phase relation with the fields.

introduces a phase shift of $+\pi/2$ (resp. $-\pi/2$) in the fields generated at ω_s (respectively ω_p). Additionally, the detection is performed in the far field, adding and extra $-\pi/2$ phase to the field generated by the dipole. *In fine*, the field at ω_s (respectively ω_p), which is generated by nonlinear interactions and mediated by the molecular resonance, is in phase (resp. in phase opposition) with the initial field at this frequency. The electric field will then add constructively (respectively destructively) with the incoming field and lead to a photon gain (respectively loss) at frequency ω_s (respectively ω_p).

2.3 Stimulated Raman Scattering

Our study focuses almost exclusively on SRS, most often performed by SRL. This section focuses more particularly on SRL and derives the dependence of the signal with respect to the relevant parameters.

As derived previously, the electronic motion can be expressed with the electric fields up to the third order (Equation 2.41 to 2.45):

$$\begin{aligned} x(t) = &\int_{-\infty}^{+\infty} \frac{-q}{m} H(\omega_1) E(\omega_1) e^{-i\omega_1 t} \mathrm{d}\omega_1 \\ &+ \int_{-\infty}^{+\infty} \int_{-\infty}^{+\infty} \frac{-q^2 \eta_{xx}}{m^3} H(\omega_1+\omega_2) H(\omega_1) H(\omega_2) E(\omega_1) E(\omega_2) e^{-i(\omega_1+\omega_2)t} \mathrm{d}\omega_1 \mathrm{d}\omega_2 \\ &+ \int_{-\infty}^{+\infty} \int_{-\infty}^{+\infty} \int_{-\infty}^{+\infty} \frac{-q^3 \eta_{xX} \eta_{xx} \delta_x}{m^5 M} H(\omega_1+\omega_2+\omega_3) H(\omega_3) G(\omega_1+\omega_2) \\ &H(\omega_1+\omega_2) H(\omega_1) H(\omega_2) E(\omega_1) E(\omega_2) E(\omega_3) e^{-i(\omega_1+\omega_2+\omega_3)t} \mathrm{d}\omega_1 \mathrm{d}\omega_2 \mathrm{d}\omega_3 \end{aligned} \tag{2.46}$$

In order to see the macroscopic effect of the electron motion, we need to add multiple oscillators with a dipole density of n dipoles per unit volume. This will provide an expression for the polarization of the medium. However, one needs to be careful when going from the simple molecular model presented here to a macroscopic behavior.

The model described previously has been simplified, focusing only on one dimensional cases in calculations. However, in practice, each electric field may have a different polarization, and different molecules may be oriented in different directions. Since previous calculations only considered a single molecule, we have assumed a preferred orientation, and as such we have broken the symmetry of the system.

If we were to add the contributions of N molecules to derive the polarization of the medium this would assume that the molecules all have the same orientation, which is not typically the case.

For instance, if we consider a molecule symmetric to the one in Figure 2.3 ($z \rightarrow -z$), the electronic motion would have the same exact expression as in Equation 2.46, except for the sign of the second term which would be flipped.

When summing multiple oscillators' contributions to polarization, we would need to make assumptions as to the distribution of their orientation. In most of the cases we will encounter in this work, it is reasonable to assume that the oscillators' orientations are isotropic. This will result in the cancellation of the second order susceptibility, as well as the addition of first and third order contributions.

The resulting expression for the polarization, is then [14]:

$$\begin{aligned} P(\omega) = \epsilon_0 \Bigg(& \int_{-\infty}^{+\infty} \chi^{(1)}(\omega, \omega_1) E(\omega_1) \mathrm{d}\omega_1 \\ & + 3 \int_{-\infty}^{+\infty} \int_{-\infty}^{+\infty} \int_{-\infty}^{+\infty} \chi^{(3)}(\omega, \omega_1, \omega_2, \omega_3) E(\omega_1) E(\omega_2) E(\omega_3) \mathrm{d}\omega_1 \mathrm{d}\omega_2 \mathrm{d}\omega_3 \Bigg) \\ = & P^{(1)}(\omega) + P^{(3)}(\omega) \end{aligned} \tag{2.47}$$

with the assumption that H is constant:

$$\chi^{(1)}(\omega, \omega_1) \propto n\delta(\omega - \omega_1) \tag{2.48}$$

$$\chi^{(3)}(\omega, \omega_1, \omega_2, \omega_3) \propto n\delta(\omega - \omega_1 - \omega_2 - \omega_3) G(\omega_1 + \omega_2) \tag{2.49}$$

Both linear and third order susceptibility are proportional to the dipole density, and the third order susceptibility contains the molecular spectral information $G(\omega)$. We focus on stimulated Raman loss and will derive the field propagation along the optical axis z, and detection scheme leading to the loss of photons. The electric field generated at frequency ω_p by the nonlinear interaction is written:

$$E_p^{(3)}(z, t) = A_p^{(3)} e^{i(k_p z - \omega_p t)} + c.c. \tag{2.50}$$

Under the slowly varying envelope approximation [15], the field propagates according to the Equation:

$$\frac{\partial A_p^{(3)}}{\partial z} = \frac{i\omega_p}{2 n_p \epsilon_0 c} P^{(3)}(\omega_p) e^{-ik_p z} \tag{2.51}$$

We write:

$$E_p(z, t) = A_p e^{i(k_p z - \omega_p t)} + c.c. \tag{2.52}$$

$$E_s(z, t) = A_s e^{i(k_s z - \omega_p s t)} + c.c. \tag{2.53}$$

With this definition of E_p and E_s, the expression of $P^{(3)}(\omega_p)$ is derived from Equation 2.47:

$$P^{(3)}(\omega_p) = 6\epsilon_0 \chi^{(3)}(\omega_p) |A_s|^2 A_p e^{ik_p z} \tag{2.54}$$

Where:

$$\chi^{(3)}(\omega_p) \propto G(\omega_p - \omega_s) \tag{2.55}$$

Injecting in Equation 2.51:

$$\frac{\partial A_p^{(3)}}{\partial z} = \frac{3i\omega_p}{n_p c}\chi^{(3)}(\omega_p)|A_s|^2 A_p \tag{2.56}$$

We note that in the case of SRS, the phase matching conditions are automatically met. Assuming that the nonlinear interaction occurs over a length L, and that the intensity of the pump and Stokes beam does not change significantly over this distance, the nonlinear field can be calculated by integrating Equation 2.56 over the interaction distance L:

$$A_p^{(3)} = \frac{3i\omega_p}{n_p c}\chi^{(3)}(\omega_p)|A_s|^2 A_p L \tag{2.57}$$

After the interaction, the nonlinear field and the incident field will interfere on the detector, leading to an optical intensity:

$$I_p^{SRL} = 2n_p\epsilon_0 c|A_p + A_p^{(3)}|^2 = 2n_p\epsilon_0 c\Big(|A_p|^2 + |A_p^{(3)}|^2 + 2\mathrm{Re}(A_p^\star A_p^{(3)})\Big) \tag{2.58}$$

The term $|A_p^{(3)}|^2$ is negligible in comparison to $|A_p|^2$, but the last term can be significant. Using Equation 2.57 and 2.58 we obtain:

$$I_p^{SRL} = 2n_p\epsilon_0 c|A_p + A_p^{(3)}|^2 = 2n_p\epsilon_0 c|A_p|^2\Big(1 - \frac{6i\omega_p L}{n_p c}|A_s|^2\mathrm{Im}(\chi^{(3)}(\omega_p))\Big) \tag{2.59}$$

Using the intensity $I_p = 2n_p\epsilon_0 c|A_p|^2$ of the incident pump beam and $I_s = 2n_s\epsilon_0 c|A_s|^2$ of the incident Stokes beam, one can further write:

$$I_p^{SRL} = I_p(1 - \beta) \tag{2.60}$$

Where β is the relative amplitude change (loss in this case) due to the presence of the nonlinear medium $\chi^{(3)}(\omega_p)$:

$$\beta = \frac{3i\omega_p L}{2n_s n_p\epsilon_0 c^2} I_s\mathrm{Im}(\chi^{(3)}(\omega_p)) \tag{2.61}$$

Equation 2.60 and 2.61 illustrates the fact that the pump beam effectively losses photons due to the presence on the non linear vibrations. A similar derivation would show that the Stokes beam gains photons as a result. Using the expression of $\chi^{(3)}(\omega_p)$ derived from the molecular model, we demonstrate that this non linear susceptibility is directly proportional to the molecular response $G(\omega_p - \omega_s)$ (Equation 2.55). Therefore, the measurement of the photon loss on the pump beam is a direct measurement of the molecular absorption spectrum at the angular frequency $\omega_p - \omega_s$, via the imaginary part of $G(\omega)$. The relative amplitude loss β is proportional to the number of molecules participating in the

process, and proportional to the intensity of the Stokes beam.

3 Signal and Noise in SRS

We will now revisit laser intensity noise in the context of stimulated Raman scattering (SRS), which has recently proved to be a key technique to provide label free images of chemical bonds in biological and medical samples. Contrary to most microscopy techniques, which detect a weak photon flux resulting from light matter interactions, SRS works in the high flux regime and happens as a weak modulation ($10^{-4} - 10^{-6}$) in a strong laser field. As a result, laser noise is a key issue in SRS detection. This Chapter will provide the tools to assess the amount of noise and the ultimate SRS detection limit in a conventional lock-in based SRS system.

First, we present a brief overview on noise in laser systems by deriving the expression of the power spectral density. Next, we describe a simple procedure to assess the sensitivity of an SRS system in terms of the relative intensity noise (RIN). A proper and easy way to measure the RIN is described in detail using commercially available electronics. Finally, we illustrate this measurement on two commercial laser systems and discuss the implications of such RIN measurements for SRS system developments.

3.1 Introduction

Over the last two decades, coherent Raman imaging has evolved as a mature, label-free, imaging technique with numerous applications in biology and medicine [16]. The seminal work of Zumbusch in 1999 revived coherent Anti-Stokes Raman scattering (CARS) [17] as a vibrational microscopic imaging modality [8]. Since then, the coherent Raman imaging field experienced a second revolution in 2008 when stimulated Raman scattering (SRS) [18] was also demonstrated as a powerful vibrational imaging scheme [19, 20]. Contrary to CARS, SRS is free of nonresonant background and scales linearly with the molecular concentration [14]. These key features initiated the development of SRS imaging technologies [21, 22, 23, 24, 25, 26, 12, 27] and facilitated their successful applications in biology [28, 29, 30, 31], chemistry [32, 33] and medicine [34, 35, 2] as a quantitative and label free chemical imaging modality.

Contrary to CARS, which detects faint generated photons at specific wavelengths, SRS is a pump-probe scheme that works in the high photon flux regime. It therefore manifests itself as a weak modulation ($10^{-4} - 10^{-6}$) that is transferred from an amplitude modulated laser (the pump) on an unmodulated laser beam (the probe) [19]. Note that the notion of pump beam in the context of SRS is ambiguous, as both SRS pump and Stokes beam can be used for modulation, and therefore referred to as pump in the sense of the pump-probe measurement. To avoid confusion we will use the notion of pump beam exclusively in the sense

of SRS, and use "modulated beam" for pump-probe measurements.

As a result of the weak modulation transfered to the probe beam, the laser noise and the detection of electronic noise are key components to achieve the ultimate SRS detection level [36, 37]. For instance, performing SRS with noisy fiber lasers requires the development of specific balanced detection schemes [27, 38] that are at best $3\,\mathrm{dB}$ above the shot noise limit. Although this is a key aspect of SRS, it appears that considerations on laser and detection noise in SRS imaging systems are still lagging behind when compared to the demonstrated technological and application advances. For instance, it is often not clear in published papers where the reported SRS detection ability sits as compared to the shot noise limit.

Here, we intend to provide the theoretical basics and a reliable experimental method to characterize the noise of a SRS system and compare it to the ultimate shot noise. We start by defining noise in the context of SRS and identifying the limiting experimental sources of noise. The equations relative to laser noise are briefly reminded. We then provide a simple experimental way to measure laser noise in a traditional lock-in based detection scheme and compare it to the theoretical shot-noise limit. We further introduce the relative intensity noise (RIN) as the proper figure of merit to discuss amplitude noise in a laser system. Key features of the RIN are illustrated, as well as its link with speed and sensitivity for SRS measurements. To illustrate our proposed noise characterization method, we measure the RIN of two commercial laser systems commonly used for SRS imaging. We finally discuss the implications of such measurements and additional means to further increase the signal to noise ratio (SNR)in SRS.

3.2 Noise and signal in stimulated Raman scattering (SRS)

In SRS, one measures the intensity fluctuation of a laser beam. This fluctuating intensity is converted into a photo-current via a detector. The output of this detector is typically sent to the input of a lock-in amplifier which provides a voltage as its output. Eventually, this voltage is digitized and used for further analysis. The whole concept of SRS measurements is to quantify how this acquired voltage changes over time, while scanning a sample for instance. This time-varying voltage can be a result of Raman gain, or loss, stemming from chemical bonds present in a sample (Chapter 2), in which case the fluctuation will be addressed to as *signal*. Voltage fluctuations may also result from undesired factors, in which case the they will be referred to as *noise*.

In the chain of events preceding the measurement of this fluctuating voltage, from the first light generation with a laser system to the final analog to digital converter, external noises can influence the signal through various ways (Figure 3.1). We call P_{noise} the electrical power associated to noise contributions.

P_{noise} is measured through its voltage root mean square error V_{rms} using a resistance R.

$$P_{noise} = \frac{V_{rms}^2}{R} \tag{3.1}$$

This noise sets the lower limit on the signal electrical power P_{signal} that can be detected, and therefore the SNR of the system.

$$SNR = \frac{P_{signal}}{P_{noise}} \tag{3.2}$$

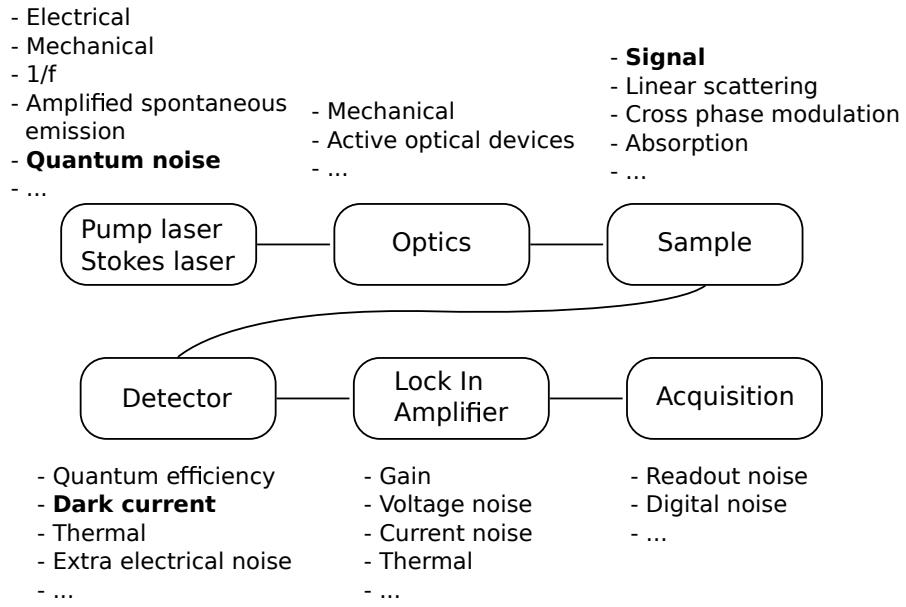

Figure 3.1 – Typical SRS flowchart indicating the origin and nature of various factors influencing the signal quality. The bold items are the ones that limit the signal to noise ratio in the optimal scenario.

Ultimately, the laser shot noise sets the physical limit to the measurement. To date, there is no report of sub shot noise SRS measurements. In addition to laser shot noise, there are usually other sources of noise limiting the SNR, such as the detector dark current and the laser excess noise.

Using a biased detector and a laser average intensity higher than a few milliwatts, one already reaches the point where the detector dark current is smaller than the laser shot noise. The detector dark current is therefore negligible in most experimental systems, and the noise limitation is set by the laser excess noise or shot noise.

Examples of laser excess noise are flicker noise that scales as 1/f (where f represents the frequency), amplified spontaneous emission, or noisy pump diode. In order to give a general understanding of laser noise, we model the optical

intensity of a laser by a time varying function $\mathcal{I}_{opt}(t)$. In this study, we will use the term *optical intensity*, rather than *optical power*, in order to avoid confusion when addressing electrical power. For simplicity, the laser will be assumed to be monochromatic. The electrical current $I(t)$, also called photo-current, generated by the detector through photoelectric conversion is:

$$I(t) = \frac{\eta q}{h\nu}\mathcal{I}_{opt}(t) \tag{3.3}$$

Where η is the detector quantum efficiency, ν the optical frequency, q the electron charge and h the Plank constant.

In the context of periodic illumination such as that found in pulsed laser systems, this function has an infinite time domain. To study such functions, it is useful to consider the finite-time Fourier transform [39] of $I(t)$:

$$\hat{I}_T(f) = \int_0^T I(t)e^{-2i\pi ft}\mathrm{d}t \tag{3.4}$$

The average electrical intensity and power are defined as:

$$I_{avg} = \lim_{T\to\infty}\frac{1}{T}\langle\hat{I}_T(0)\rangle \tag{3.5}$$

$$P_{avg} = RI_{avg}^2 \tag{3.6}$$

Where $\langle\cdot\rangle$ stands for the ensemble average.

We can then define the single-sided photo-current spectral density of such electrical signal, as well as the single-sided power spectral density (PSD) given an resistance R (with strictly positive frequencies only, hence the factor 2 in Equation 3.7):

$$S_I(f) = 2\lim_{T\to\infty}\frac{1}{T}\langle|\hat{I}_T(f)|^2\rangle \tag{3.7}$$

$$PSD_{laser}(f) = RS_I(f) \tag{3.8}$$

The PSD measures the amount of electrical power in the signal per unit of bandwidth and is expressed in $\mathrm{W/Hz}$. For instance, the amount of power coming from the frequency range with width Δf centered around f_0 is given by:

$$P_{\Delta f}(f_0) = \int_{f_0\pm\Delta f/2} PSD(f)\mathrm{d}f \approx PSD(f_0)\Delta f \tag{3.9}$$

In SRS measurements, it is expected that the laser remains as quiet as possible and ultimately has a power spectral density equal to zero in the range of frequency where the SRS signal is awaited. However, Equation 3.8 does not take into account the statistical nature of the photo-detection process. When describing the generated photo-current as a sum of random photo-detection events, one can derive the proper spectral density of the photo-current. The full mathe-

matical development is more fully described in the work of Quinlan et al. [40] and the PSD reads:

$$PSD_{laser}(f) = 2RqI_{avg} + R\,S_I(f) \tag{3.10}$$

This expression is made of two terms: The first refers to the shot noise and originates from the statistical fluctuations arising from the laser light photo-detection process. It increases linearly with the laser intensity with a well defined slope that does not depend on the laser system. The second one is the classical PSD described previously (Equation 3.8). It models the contribution of the classical fluctuations of the laser intensity and increases quadratically with the laser intensity. Contrary to the shot noise, the classical laser PSD can be theoretically be zero in a certain frequency range. However, the SRS signal will contribute to this term by being a classical fluctuation imprinted onto the probe laser through stimulated Raman gain or loss. In order to emphasize the quadratic dependence of the classical PSD with the photo-current, we introduce the relative intensity $\alpha(t)$:

$$I(t) = I_{avg}\alpha(t) \tag{3.11}$$

With this, we can rewrite the classical photo-current spectral density (Equation 3.7) as:

$$S_I(f) = I_{avg}^2 S_\alpha(f) \tag{3.12}$$

Where $S_\alpha(f)$ (excess relative intensity noise, see Section 3.4.1) is expected not to vary when the average photo-current increase. In the following, we will work under this hypothesis, but nonlinear effects such as saturation of the detector can break this assumption.

So far, we have considered only the laser light as the source of noise, but one can add the power spectral density coming from the detector dark current, or any excess electrical noise coming from the detection line. We model these other sources of noise as $K(f)$, a function that does not depend on laser intensity. Assuming the electronic noise is uncorrelated with the photo-current we can simply add the power spectral densities to obtain to total PSD:

$$\begin{aligned} PSD_{total}(f, I_{avg}) = &\, PSD_{laser,classical}(f, I_{avg}) \\ &+ PSD_{laser,shotnoise}(I_{avg}) \\ &+ PSD_{electronics}(f) \end{aligned} \tag{3.13}$$

where

$$PSD_{laser,classical}(f, I_{avg}) = S_\alpha(f) R I_{avg}^2 \tag{3.14}$$

$$PSD_{laser,shotnoise}(I_{avg}) = 2qRI_{avg} \tag{3.15}$$

$$PSD_{electronics}(f) = K(f) \tag{3.16}$$

3.3 Basic experimental measurement of noise

3.3.1 Model

Having described the power spectral density, one is able to know the nature of the noise limiting an SRS measurement. This can usually be done without major modification of a conventional SRS experiment. In a sense, a lock-in amplifier is optimally built for measuring the power spectral density; It filters the input electrical spectrum with a certain band pass filter of width Δf around the reference frequency f_0, amplifies it with a gain G, and centers it around the DC component. Typically, the bandwidth of a lock-in is narrow relatively to the center frequency ($\Delta f \ll f_0$). Under this condition, we can consider the PSD to be constant around f_0. As a result, the total electrical power that is expected as the output of the lock-in amplifier can be written:

$$P_{f_0,\Delta f}(I_{avg}) = G\Delta f PSD_{total}(f_0, I_{avg}) \tag{3.17}$$

Using Equations 3.13 to 3.16, we can see that $P_{f_0,\Delta f}$ is a second order polynomial in I_{avg} where each coefficients is associated with a specific type of noise.

$$P_{f_0,\Delta f}(I_{avg}) = G\Delta f\Big[K(f_0) + 2qRI_{avg} + S_\alpha(f_0)RI_{avg}^2\Big] \tag{3.18}$$

Following Equation 3.1, $P_{f_0,\Delta f}$ can be directly measured through the voltage root mean square error (rms) across a resistance R using an oscilloscope or any other voltage acquisition device:

$$P_{f_0,\Delta f}(I_{avg}) = \frac{V_{rms}^2(I_{avg})}{R} \tag{3.19}$$

In order to qualitatively assess the noise level in an SRS system, one can measure experimentally $P_{f_0,\Delta f}(I_{avg})$ and plot the result as a function of I_{avg} in a log-log plot (Figure 3.2). The resulting plot should have different slopes on the logarithmic scale depending on which noise dominates the measurement. Electronic noise, shot noise, or excess classical laser noise will have slopes of 0, 1, or 2, respectively. The following section describes a more quantitative approach and illustrates it on two different SRS imaging setups using different laser systems.

3.3.2 Method

Proper characterization of the lock-in system is important to measure the parameters in Equation 3.18 and to ensure a quantitative comparison of the model with experimental data. We used a commercially available detector and lock-in amplifier (APE LIA, Berlin). The integration τ time was set to $20\,\mu s$. An analog

lock-in amplifier such as this has a passive RC filter, and its bandwidth is linked to the integration time τ by:

$$\Delta f = \frac{1}{2\pi\tau} = 8\,\mathrm{kHz} \tag{3.20}$$

We measured the gain G of our lock-in amplifier experimentally using an reference signal at $f_0 = 20\,\mathrm{MHz}$. The input signal entering the lock-in was a sinusoidal voltage of amplitude $300\,\mathrm{uV}$ and frequency $f_0 + 3\,\mathrm{kHz}$. The output signal from the lock-in resulted in a sinusoidal voltage of amplitude $1.8\,\mathrm{V}$ and frequency $3\,\mathrm{kHz}$. The associated gain in power was therefore measure to be $G = 75.56\,\mathrm{dB}$. The reference, lock-in input and output signals were generated and recorded using a multipurpose system (Zurich Instrument HF2LI). Given G and Δf, the electronic noise $K(f_0)$ can be measured directly by blocking the laser beam before the photodiode ($I_{avg} = 0$). The measured lock-in output voltage root mean square in the absence of the laser was $V_{rms}(0) = 1.1\,\mathrm{mV}$. This corresponds to an electrical noise power in a $R = 50\,\mathrm{Ohm}$ resistance (Equation 3.18):

$$P_{f_0,\Delta f}(0) = G\Delta f\, K(f_0) = 2.4210^{-8}\,W = -76\,\mathrm{dBW} \tag{3.21}$$

This means the equivalent electrical noise prior to amplification is:

$$K(f_0) = -190\,\mathrm{dBW/Hz} = \left(2\,\mathrm{nV}/\sqrt{\mathrm{Hz}}\right)^2/50\Omega \tag{3.22}$$

The power spectral density $PSD_{laser,shotnoise}(I_{avg})$ associated to shot noise is given by Equation 3.15. As a result the only unknown in Equation 3.18 is the power spectral density associated with the laser classical fluctuation $PSD_{laser,classical}(f, I_{avg})$ given by Equation 3.14.

The average photo-current I_{avg} delivered by the photodiode can either be measured directly with an oscilloscope, or derived from Equation 3.3 where $\mathcal{I}_{opt}(t)$ is replaced by its time averaged intensity. Knowing the quantum efficiency $\eta = 0.8$ of our photodiode at $800\,\mathrm{nm}$, we used the latter option. As a result for a laser at this wavelength $I_{avg} = 0.5\mathcal{I}_{opt}$ where $\mathcal{I}_{opt}$ is expressed in Watts and I_{avg} in Amperes. Note that all the above described derivation assumes that the detector is below saturation, this can be easily achieved experimentally by controlling the laser power and its overlapping with the photodiode.

The electrical power $P_{f_0,\Delta f}(I_{avg})$ (Equations 3.18 and 3.19) ($f_0 = 20\,\mathrm{MHz}$, $\Delta f = 8\,\mathrm{kHz}$) at the output of the lock-in amplifier was recorded using our multipurpose system (Zurich Instrument HF2LI) for varying laser intensity (and therefore different I_{avg}) and the resulting data were compared to the expected value on a logarithmic plot (Figure 3.2).

3.3.3 Results

The SRS noise analysis was performed on two commercial laser systems using a $800\,\mathrm{nm}$ beam.

Device 1 is a Ti:Saph femtosecond laser (Chameleon, Coherent Inc) operating at a repetition rate of $80\,\mathrm{MHz}$ with a pulse width duration of $160\,\mathrm{fs}$ and a wavelength of $800\,\mathrm{nm}$. This beam acts as the (unmodulated) pump beam of a SRS laser system whereas the (amplitude modulated) Stokes beam is provided by a tunable femtosecond optical parametric oscillator OPO pumped by the Ti:Saph laser (Section 6.1, describes the system in more details). Here, we only consider the (unmodulated) $800\,\mathrm{nm}$ beam as it is the one monitored by the SRS photodiode.

Device 2 is a picosecond OPO (Emerald, APE) operating at a repetition rate of $80\,\mathrm{MHz}$ with a pulse duration of $2\,\mathrm{ps}$ and a wavelength of $800\,\mathrm{nm}$. This OPO is pumped by a frequency doubled ytterbium fiber laser (Emerald engine, APE) ($80\,\mathrm{MHz}$ repetition rate, $2\,\mathrm{ps}$ pulse duration) that also provides the Stokes beams at $1030\,\mathrm{nm}$. We consider here only the (unmodulated) $800\,\mathrm{nm}$ OPO beam as it is the one monitored by the SRS photodiode. Note that device 2 is similar to the commercially available one box PicoEmerald SRS system (APE).

Figure 3.2 shows the electrical power $P_{f_0,\Delta f}(I_{avg})$ ($f_0 = 20\,\mathrm{MHz}$, $\Delta f = 8\,\mathrm{kHz}$) at the output of the lock-in amplifier (LIA, APE) as recorded by the oscilloscope (HF2LI, Zurich Instrument) for different photodiode output current I_{avg}. $P_{f_0,\Delta f}(I_{avg})$ is expressed in dBW.

The power plotted for electronic noise (Equation 3.18 first term, Figure 3.2 grey dashed line) and shot noise (Equation 3.18 second term, Figure 3.2 grey solid line) are the expected contributions using our model.

We can see that the measured power from Device 1 matches the model (dotted orange line), with no measurable classical laser noise (Equation 3.18 third term) also known as excess laser noise ($S_\alpha(f_0)RI_{avg}^2 << 2qRI_{avg}$). For photo-currents I_{avg} higher than $5\,\mathrm{mA}$ (i.e. laser intensities on the photodiode above $10\,\mathrm{mW}$) the SRS measurement with this system is shot noise limited.

Device 2 exhibits a clear quadratic dependence characteristic of an excess laser noise (Figure 3.2 light grey dot-dashed line). In this case we used the points of highest photodiode current to fit $S_\alpha(f_0)$ and model the data taking into account excess laser noise (dotted blue line). For a photo-current of $10\,\mathrm{mA}$ (i.e. laser intensity of $20\,\mathrm{mW}$) the noise level on Device 2 is $12\,\mathrm{dB}$ above the shot noise limit. This means that the measured voltage has fluctuations $6\,\mathrm{dB}$ (i.e. 4 times) higher than that of an equivalent shot noise limited system under the same conditions.

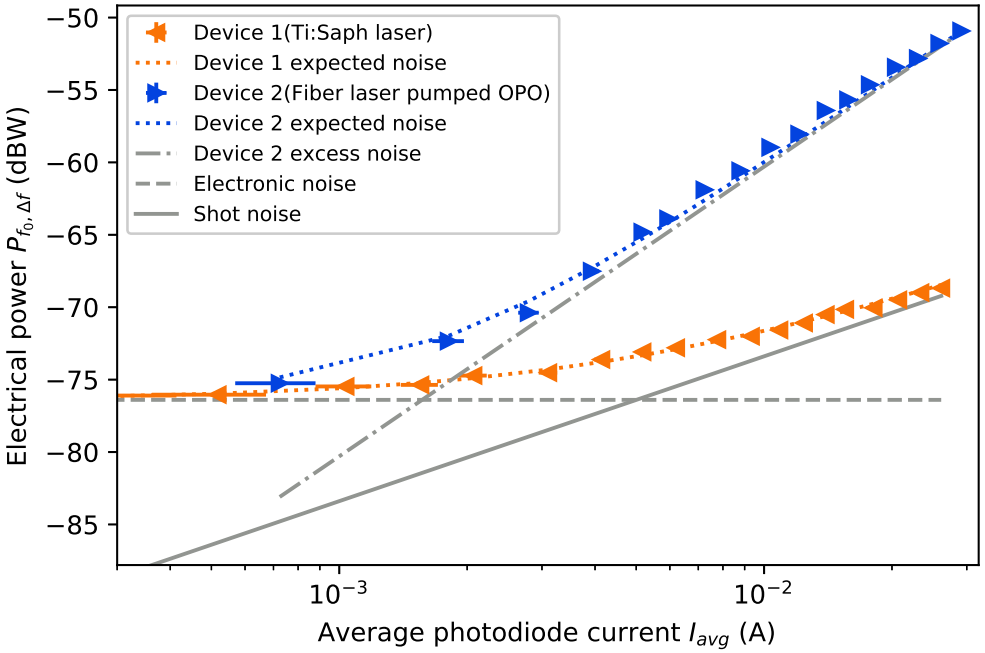

Figure 3.2 – Electrical power (expressed in dBW) at the output of the lock-in amplifier ($f_0 = 20\,\text{MHz}$, $\Delta f = 8\,\text{kHz}$) with increasing average laser photodiode current I_{avg} (and therefore average laser intensity). The figure shows raw measured electrical power for Device 1 (Ti:Saph - orange left triangles) and Device 2 (Fiber laser pumped OPO - blue right triangles). For small optical intensity, the electronic noises (grey dashed line) dominates over the laser noise. The noise increases linearly with laser intensity in the case of shot noise (solid grey line) and quadratically in the case of excess noise (dot-dash grey line). Note that no SRS signal is present here, however the expected SRS signal will contributes to the electrical power in a way similar to the excess noise and will show a quadratic dependence with I_{avg}.

3.4 A figure of merit: the Relative Intensity Noise.

3.4.1 Definition

Although the power spectral density is a powerful tool to characterize noise, it fails to provide a meaningful figure of merit when comparing different systems. In fact, the same PSD can be achieved by a shot noise limited laser working at high intensity, or a laser with higher noise levels that is working at low intensity. It is useful to refer to the relative intensity noise (RIN) in order to be more specific when discussing laser noise. The RIN is defined as the power spectral density divided by the power of the DC component :

$$RIN_{laser}(f, I_{avg}) = \frac{PSD_{laser}(f, I_{avg})}{RI_{avg}^2} \tag{3.23}$$

the RIN is the power contribution relative to DC power, per unit bandwidth, usually expressed in $\mathrm{dBc/Hz}$. The interesting features appear when using the expression of the PSD in Equation 3.10 and 3.12. The RIN then becomes :

$$RIN_{laser}(f, I_{avg}) = S_\alpha(f) + \frac{2q}{I_{avg}} \tag{3.24}$$

In this expression, we expect the first term to be constant with respect to optical intensity and the second term to decrease as optical intensity increases. Such a quantity behaves more like what one would expect from a figure of merit describing noise. If the limiting factor is the laser excess noise, the RIN at a given frequency will be constant and will not improve (decrease) with higher laser intensity:

$$RIN_{laser,excess}(f) = S_\alpha(f) \tag{3.25}$$

If the laser is shot noise limited (at a given frequency) the RIN will be given by:

$$RIN_{laser,shotnoise}(I_{avg}) = \frac{2q}{I_{avg}} \tag{3.26}$$

It will decrease with increasing laser intensity, until the first term in Equation 3.24 or another source of noise becomes limiting again. This highlights the very important fact that a shot noise limited system is only reaching this limit around a certain frequency and a certain photo-current.

Additionally, one could define the RIN associated with the electrical noises:

$$RIN_{electronics}(f, I_{avg}) = \frac{K(f)}{RI_{avg}^2} \tag{3.27}$$

As expected, this noise will dominate all other noise contributions when the

average photo-current approaches 0.

3.4.2 RIN in SRS

The RIN allows to quantify the performance of a laser system used to conduct SRS experiments. The minimal RIN imposed by physical laws ($RIN_{laser,shotnoise}$) is independent of the frequency and scales inversely with I_{avg} (Equation 3.26). On the contrary, the minimal RIN set by the design of the laser ($RIN_{laser,excess}$) is a well-defined function of frequency and does not depend on I_{avg}.

Given the laser excess RIN $S_\alpha(f)$, one can already anticipate the domain of frequency and photo-current for which the laser fluctuations will be shot noise limited. We will now illustrate this in the specific context of SRS.

In a standard SRS system, a pump laser beam with electric field intensity $\mathcal{I}_p$ and a Stokes beam with electric field intensity $\mathcal{I}_s$ are sent through a sample containing N oscillators having a stimulated Raman cross section σ. When collecting either $\mathcal{I}_p$ or $\mathcal{I}_s$ in the far field after their interactions with the sample, one can measure an intensity loss $\Delta\mathcal{I}_p$ on the pump beam, and an intensity gain $\Delta\mathcal{I}_s$ on the stokes beam. The exact expression of these quantities depends on many factors, and in-depth developments can be found in Chapter 2 and in the litterature [14, 4]. For our analysis, we are solely interested in the way $\Delta\mathcal{I}_{p,s}$ depends on $\mathcal{I}_p$, $\mathcal{I}_s$, N, and σ:

$$\Delta\mathcal{I}_p \propto -N\sigma\mathcal{I}_p\mathcal{I}_s \tag{3.28}$$
$$\Delta\mathcal{I}_s \propto +N\sigma\mathcal{I}_p\mathcal{I}_s \tag{3.29}$$

As a direct result of Equations 3.28 and 3.29, if a modulation at frequency f_0 is applied on either one of the lasers, the change in intensity $\Delta\mathcal{I}$ of the second laser will also be modulated at the same frequency. We will refer to the first laser as the modulated laser, and the second, unmodulated one, as the probe laser. Without loss of generality, we will assume that the pump beam is modulated while the Stokes beam is used as a probe (stimulated Raman gain modality). Additionally, we will assume a total modulation:

$$\mathcal{I}_{modulated} = \mathcal{I}_p\frac{1+cos(2\pi f_0 t)}{2} \tag{3.30}$$

As a result of this modulation, the intensity change in the probe laser becomes:

$$\Delta\mathcal{I}_s \propto N\sigma\mathcal{I}_s\mathcal{I}_p\frac{1+cos(2\pi f_0 t)}{2} \tag{3.31}$$

And the probe laser intensity reads:

$$\mathcal{I}_{probe} = \mathcal{I}_s + \Delta\mathcal{I}_s = \mathcal{I}_s\left(1+\frac{1}{2}\beta(1+cos(2\pi f_0 t))\right) \tag{3.32}$$

Where β is the relative amplitude of the SRS gain or loss, as described in Section 2.3, and does not depend on the probed beam intensity:

$$\beta \propto N\sigma I_{pump} \tag{3.33}$$

(alternatively $-N\sigma I_{stokes}$ if the Stokes beam is modulated)

The probe laser intensity is detected by the photodiode which generates a current (Equation 3.3) that reads:

$$I(t) = I_{avg}\alpha(t)m(t) \tag{3.34}$$

Where $\alpha(t)$ is the relative intensity fluctuation in the absence of the modulated beam (Section 3.2) and $m(t)$ the modulation transferred from the modulated beam:

$$m(t) = 1 + \frac{1}{2}\beta\,(1 + cos(2\pi f_0 t)) \tag{3.35}$$

With this definition $I_{avg}m(t)$ fluctuates between I_{avg} and $I_{avg} + \Delta I$. Where ΔI is linked to β through the following relation:

$$\beta = \frac{\Delta I}{I_{avg}} \tag{3.36}$$

β is typically small for most experimentally relevant applications, of the order of 10^{-4} to 10^{-6}.

In the lock-in amplifier, the photo-current $I(t)$ is mixed with the reference signal $r(t) = g\,\cos(2\pi f_0 t)$. The amplitude g of this reference signal comes as an overall gain, and does not affect the discussion on SNR. Therefore, we will assume $g = 1$ for simplicity. The mixed current can be expressed as:

$$I_m(t) = I_{avg}\alpha(t)m(t)r(t) = I_{avg}\alpha(t)\left[\frac{\beta}{4} + (1+\frac{\beta}{2})cos(2\pi f_0 t) + \frac{\beta}{4}cos(2\pi 2 f_0 t)\right] \tag{3.37}$$

In terms of Fourier components:

$$\begin{aligned}\hat{I}_{mT}(f) = I_{avg}\Big[&\frac{\beta}{4}\hat{\alpha}_T(f) + (\frac{1}{2} + \frac{\beta}{4})(\hat{\alpha}_T(f + f_0) + \hat{\alpha}_T(f - f_0)) \\ &+ \frac{\beta}{8}(\hat{\alpha}_T(f + 2f_0) + \hat{\alpha}_T(f - 2f_0))\Big]\end{aligned} \tag{3.38}$$

The average current at the output of the locking amplifier $I_{m,avg}$ can readily be computed using Equation 3.5:

$$I_{m,avg} = \lim_{T\to\infty}\frac{1}{T}\langle\hat{I}_{mT}(0)\rangle = I_{avg}\frac{\beta}{4} \tag{3.39}$$

This current provides the DC power at the output of the lock-in with a load

resistor R. This is the signal power associated with a modulation β of the input signal. It can be written:

$$P_{DC} = RI_{avg}^2 \frac{\beta^2}{16} \tag{3.40}$$

Revisiting Equation 3.38, we expect the relative intensity fluctuations $\hat{\alpha}_T(f)$ to be small for non zero frequencies, of the order of β. Keeping only the terms of the order of β Equation 3.38 writes:

$$\hat{I}_{mT}(f) = \frac{I_{avg}}{2}(\hat{\alpha}_T(f + f_0) + \hat{\alpha}_T(f - f_0)) \tag{3.41}$$

It is worth noting that this simplification does not hold true when the frequency $2f_0$ matches a harmonic of the laser repetition rate. In this case, the last term in Equation 3.38 becomes significant and has to be accounted for in both $I_{m,avg}$ and $\hat{I}_{mT}(f)$. The effect has been calculated by Ozeki and collaborators [37] and results in a gain of a factor of 2 in SNR as compared to the more conventional SRS scheme presented here.

From Equation 3.41 we can calculate the photo-current spectral density $S_{I_m}(f)$ (Equation 3.7), for the mixed current at the output of the lock-in amplifier:

$$S_{I_m}(f) = 2 \lim_{T\to\infty} \frac{1}{T} \langle |\hat{I}_{mT}(f)|^2 \rangle = \frac{1}{4}(S_I(f_0 + f) + S_I(f_0 - f)) \tag{3.42}$$

There are no cross terms because there are no correlations between noises at different frequencies. The lock-in also applies a low pass filter, meaning the only relevant frequencies will be for $f < \Delta f \ll f_0$, where Δf is the filter bandwidth defined in Equation 3.20. We expect S_I to be slowly varying around f_0, and we will approximate it by its value in f_0. The power spectral density for the mixed current then reads:

$$R\, S_{I_m}(f) = \frac{R}{2}\, S_I(f_0) = \frac{1}{2}\Big(2qRI_{avg} + RI_{avg}^2 S_\alpha(f_0)\Big) = \frac{RI_{avg}^2}{2} RIN_{laser}(f_0, I_{avg}) \tag{3.43}$$

Integrating the power spectral density over the lock-in bandwidth Δf, and following Equation 3.9 the electrical power of the noise at the output of the lock-in amplifier can be expressed as:

$$P_{Noise} = \frac{RI_{avg}^2}{2} RIN_{laser}(f_0, I_{avg})\, \Delta f \tag{3.44}$$

Using Equations 3.40 and 3.44, the signal to noise ratio as the output of the lock-in amplifier can ultimately be expressed as:

$$SNR = \frac{P_{DC}}{P_{Noise}} = \frac{\beta^2}{8\Delta f RIN_{laser}(f_0, I_{avg})} \tag{3.45}$$

The result of Equation 3.45 states that, assuming all other sources of noise are negligible, the SNR in a lock-in based SRS setup is given by the RIN of the laser around the modulation frequency. β is the modulation transfer amplitude on the probe beam; Its scales linearly with the molecular concentration and its value depends on the stimulated Raman cross section. Another way to interpret Equation 3.45 is to express the smallest modulation ΔI_{min} a system can detect with an SNR of 1.

$$\frac{\Delta I_{min}}{I_{avg}} = \beta_{min} = \sqrt{8\Delta f RIN_{laser}(f_0, I_{avg})} \tag{3.46}$$

Let us now consider a practical case: a laser with a wavelength of $800\,\mathrm{nm}$ and an average power of $10\,\mathrm{mW}$ is sent on a photodiode with of quantum efficiency $\eta = 0.8$. The photocurrent generated is given by Equation 3.3: $I_{avg} = 5\,\mathrm{mA}$. Using Equation 3.26, the theoretical RIN associated with shot noise is then $-162\,\mathrm{dBc/Hz}$.

The smallest modulation detectable with $\Delta f = 8\,\mathrm{kHz}$ is given by Equation 3.46:

$$\frac{\Delta I_{min}}{I_{avg}} = \beta_{min} = \sqrt{8 \cdot 8 \times 10^3 \cdot 10^{-162/10}} = 2.0 \times 10^{-6} \tag{3.47}$$

This sensitivity limit for a SRS setup is directly related to the smallest number of molecular bonds detectable inside the focal point of a microscope. However, the derivation of this ultimate number of molecular bonds is not straightforward. This number depends on the molecular stimulated Raman scattering cross section, but also some technical parameter such as the pump and Stokes beam overlap and their respective powers.

It is important to stress that the signal to noise ratio is meaningful only if a bandwidth is specified. For instance, for the same average current but with a bandwidth of $\Delta f = 1\,\mathrm{MHz}$, the sensitivity becomes

$$\frac{\Delta I_{min}}{I_{avg}} = \sqrt{8 \cdot 10^6 \cdot 10^{-162/10}} = 2.2 \times 10^{-5} \tag{3.48}$$

As a direct result of Equation 3.45, any deviation from the minimal RIN results in a sub-optimal measurement that impairs the SNR, which ultimately slows down signal acquisition.

Eventually, the proper way to evaluate and assess the performance of a SRS system with respect to laser noise is to specify:

(i) The photo-current from the detector, which sets the shot noise limited RIN and SNR through Equations 3.26 and 3.45.

(ii) The achieved experimental RIN by either its absolute value or its distance in dB from the shot noise limit.

Ideally, one needs to measure the RIN as a function of both photo-current and frequency. A way to obtain such measurement is detailed in the next section.

The complete RIN measurement allows to compare the system's performance with both the physical limit and other implementations of SRS.

3.4.3 Maximizing the SRS signal to noise ratio

We have derived the exact contribution of both noise and SRS signal to the electrical power output of a lock-in amplifier based SRS system. For a system with electrical noise $K(f)$, excess laser RIN $S_\alpha(f)$, average photodiode current I_{avg}, load resistor R, amplifier gain G, lock-in bandwidth Δf, modulation frequency f_0, and SRS signal $\beta = \frac{\Delta I}{I_{avg}}$, the output power of the lock-in amplifier reads:

$$P_{f_0,\Delta f} = G\left[\Delta f\left(K(f_0) + 2qRI_{avg} + S_\alpha(f_0)RI_{avg}^2\right) + \frac{\beta^2}{8}RI_{avg}^2\right] \tag{3.49}$$

This expression holds true assuming the following:

(i) All electronic noises affect the signal prior to the lock-in amplifier module. Under typical working conditions of a lock-in based SRS system, the limiting electrical source of noise is the photodiode current noise, which verifies this condition.

(ii) $K(f)$ and $S_\alpha(f)$ can be considered constant in a bandwidth Δf around f_0. The expression can be generalized with an integral to account for any frequency dependence in these two functions.

(iii) The modulation frequency f_0 is strictly smaller than half of the repetition rate of the measured laser. Tuning f_0 to half of the repetition rate gives a different expression for the electrical power output of the lock-in amplifier.

(iv) The laser relative intensity fluctuations $\hat{\alpha}(f)$ are small. This assumption will be verified for any stable laser system.

Each noise component of Equation 3.49 is illustrated in Figure 3.2. Electronic noise ($K(f_0)$), shot noise ($2qRI_{avg}$), and laser excess noise ($S_\alpha(f_0)RI_{avg}^2$) are constant, linearly increasing, and quadratically increasing with the photodiode current I_{avg}. They are represented in Figure 3.2 by grey dashed line, grey solid line, and light grey dot-dashed line, respectively. In this section, we have illustrated the fact that the electrical power of the SRS signal also increases quadratically with the photodiode current I_{avg}.

Using Equation 3.49, we can express the SNR of our system as a function of I_{avg}:

$$SNR_{f_0,\Delta f}(I_{avg}) = \frac{\frac{\beta^2}{8\Delta f}}{\frac{K(f_0)}{RI_{avg}^2} + \frac{2q}{I_{avg}} + S_\alpha(f_0)} \tag{3.50}$$

The different terms of the denominator in Equation 3.50 are precisely the RIN associated with electronic noise, shot noise, and laser excess noise respectively (Equations 3.25 to 3.27). If electronic noises are negligible, the denominator simplifies to the laser RIN (Equation 3.24 and 3.50) becomes Equation 3.45.

Using Equation 3.50, we can identify all the ways one can maximize the SNR in a lock-in based SRS system:

(i) Maximizing β, the relative modulation of the probe beam. β increases linearly with the number of molecular bonds probed, as well as with the laser intensity in the modulated beam (Equation 3.33). It is important to note that β is constant with respect to the laser intensity of the probed beam (Equation 3.33), and therefore does not depend on I_{avg}.

(ii) Minimizing Δf, the lock-in bandwidth. In principle an arbitrarily high SNR can be achieved by reducing Δf. In practice, the bandwidth has to be large enough to allow changes in the SRS signal. In a SRS point scanning microscope, we expect the signal to vary from one pixel to the next. In this case Δf should match the pixel acquisition rate to allow fluctuations from one pixel to the next, while filtering out fluctuations within a pixel.

(iii) Maximizing I_{avg} to minimize electrical noise and shot noise. Depending on the photodiode noise features, one can increase the probed laser beam intensity (end therefore I_{avg}) to reach the regime where the electronic noise $\frac{K(f_0)}{RI_{avg}^2}$ becomes negligible with respect to the laser RIN (Equation 3.24). In our applications, this regime was reached for a few milliwatts of optical intensity. When the SNR is limited by the laser RIN, one of two scenarios has to be considered. a) The RIN is limited by the shot noise (Equation 3.26), in which case the SNR will increase linearly with I_{avg}. The SNR is then limited by how much I_{avg} can be increased. This limit is set by the laser maximum output power, the saturation current of the photodiode and the sample photodamage threshold; ultimately the laser excess noise may become limiting. b) The RIN is limited by the laser excess noise (Equation 3.25), in which case increasing I_{avg} will not change the SNR. Once the SNR limit allowed by the laser is reached it cannot be improved by increasing the probed laser beam intensity.

In this last scenario, the laser excess RIN (Equation 3.25) ultimately sets the limit on the SNR in a lock-in based SRS system, and it is important to chose a modulation frequency that minimizes this excess RIN. A proper measurement of the laser RIN is therefore necessary to quantify and optimize the performance of a specific SRS system. The experimental procedure used for laser RIN measurements is detailed in the following section.

3.5 SRS noise experimental characterization.

3.5.1 Method

To properly quantify the noise level in Devices 1 and 2, we used a fast biased photodiode (Thorlabs DET10A/M, $1\,\mathrm{ns}$ rise time) placed at the position of the forward SRS detector. The average photo-current generated by the photodiode was measured with a fast oscilloscope (HP 54111D $500\,\mathrm{MHz}$ bandwidth, $50\,\Omega$ input).

The typical photo-current was several milliamperes. The associated shot noise power can be calculated using Equation 3.15 and is of the order of $-190\,\mathrm{dBW/Hz}$ which is far below the input noise ($-180\,\mathrm{dBW/Hz}$) of our spectrum analyzer (Zurich instrument HF2LI). For this reason, we added a filtering and amplification stage. The photodiode was loaded with a $50\,\Omega$ resistor and the resulting voltage was filtered with a $30\,\mathrm{MHz}$ low pass filter (Mini-Circuits BLP$-$30$+$) to damp the 80 MHz repetition rate and harmonics of the lasers. The signal was then amplified with a $25\,\mathrm{dB}$ low noise preamplifier (Ref 153579, APE) working in the range of $100\,\mathrm{kHz}$ to $100\,\mathrm{MHz}$. The overall effect of this filtering and amplification stage was to amplify by more than $20\,\mathrm{dB}$ the electrical current components between $500\,\mathrm{kHz}$ and $30\,\mathrm{MHz}$ (Figure 3.3). Following this, the electrical power spectral density was acquired with a spectrum analyzer (Zurich instrument HF2LI). The center frequency was swept across 1000 points from $500\,\mathrm{kHz}$ to $30\,\mathrm{MHz}$ with a bandwidth of $1.1\,\mathrm{kHz}$ to $70\,\mathrm{kHz}$. The effect of the filter and amplifier was numerically subtracted from the measured RIN data (Figure 3.5 and 3.6).

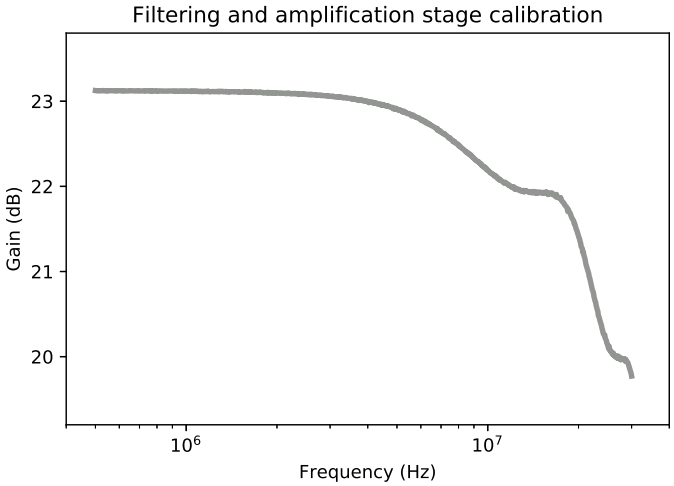

Figure 3.3 – Gain of the filter and preamplification stage.

The power spectral density associated with electronic noise was measured by blocking the laser beam. The noise level was $-173\,\mathrm{dBW/Hz}$ measured with the spectrum analyzer. This noise is a combination amplified dark current, input and output noise of the amplifier, and input noise of the spectrum analyzer. We merge all electronic noises in an equivalent power spectral density at the detector $K(f)$ (Equation 3.16). We obtain $K(f) \approx -173 - 23 = -196\mathrm{dBW/Hz}$ with very little dependence in frequency (Figure 3.4) (23 dB being the amplification, Figure 3.3). Using Equations 3.13 and 3.16, we can numerically remove the contribution of the electronic noises to the power spectral density.

After accounting for filtering, amplification, and electronic noise contributions numerically, the acquired power spectral density was transformed into RIN using

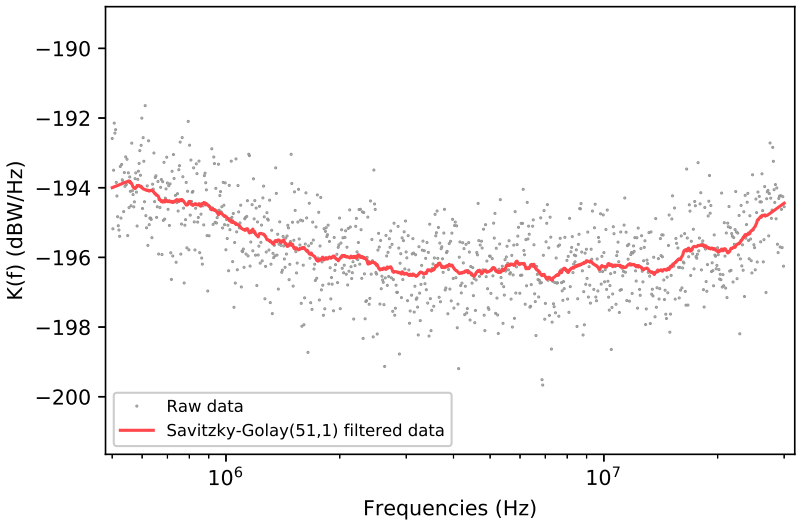

Figure 3.4 – Equivalent electronic noise power spectral density. The raw data (grey dots) has been smoothed (red line) using a Savitzky–Golay filter (51 points, 1st order).

Equation 3.23.

3.5.2 Results

For an average photo-current of $I_{avg} = 5\,\mathrm{mA}$ the recovered laser RINs are plotted in Figure 3.5 for Devices 1 and 2. For Device 1 (Ti:Saph laser), the measured data matches the expected shot noise limit for frequencies above $2\,\mathrm{MHz}$. This means that any SRS related modulation of the laser above this frequency can be detected down to the shot noise limit. For Device 2, the measured data is within $5\,\mathrm{dB}$ of the shot noise limit for frequencies above $20\,\mathrm{MHz}$. This means that the SNR of the device for this set of frequencies and photo-current is only a factor of 3 above the shot noise limit.

Complementary to the frequency analysis, one needs to measure the RIN for different photodiode currents to characterize the optimal setup working parameters. We performed this analysis by recording the RIN as a function of frequency for photo-currents ranging from $0.5\,\mathrm{mA}$ to $7\,\mathrm{mA}$. Note that above $7\,\mathrm{mA}$ we started to observe saturation of the detector, which comes in the form of a distorted signal from the photodiode output current visualized on the oscilloscope. As before, we removed numerically the effect of the electronic noise (Figure 3.4), which is dominant for small photo-currents. The full RIN measurements in the two dimensions, frequency and photodiode current, are illustrated at the end of the Chapter (Figure 3.8). Figure 3.6 illustrates better the RIN dependence with

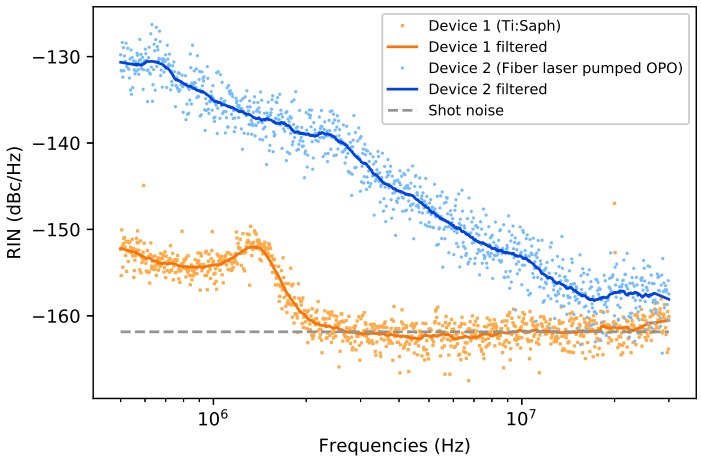

Figure 3.5 – Relative intensity noise (RIN) measured as a function of frequency for Device 1 (Ti:Saph) and 2 (Fiber laser pumped OPO) with average photodiode current $I_{avg} = 5\,\mathrm{mA}$. The solid lines are the filtered data (Savitzky–Golay filter, 51 points, 1st order).

I_{avg}, where the RIN value has been averaged between 10 and $30\,\mathrm{MHz}$.

In agreement with Figure 3.5, Device 1 is shot noise limited around $20\,\mathrm{MHz}$ for all photodiode currents, and, consequently, all laser intensities allowed by the photodiode. This observation is also consistent with Figure 3.2 which probed even higher photo-currents. Device 2 shows a small excess noise of $5\,\mathrm{dB}$ above the shot noise for $5\,\mathrm{mA}$ photo-current, which can be be clearly visualized in Figure 3.6. As expected from our model, Device 2 is shot noise limited for small enough photo-currents ($<500\,\mu\mathrm{A}$) and reaches a plateau at $S_\alpha(f_0 = 20\,\mathrm{MHz}) = -159\,\mathrm{dBc/Hz}$.

3.5.3 Discussion

The full measurement of the RIN for different electrical frequencies and laser intensities provides a much better understanding of the limits in a SRS system. This understanding is mandatory to design state-of-the art SRS systems. The choice of the laser modulation frequency is an important parameter, as it can minimize the laser RIN and maximize the SNR. In our example, the same measurement performed with 5MHz or 20MHz modulation frequency can increase the SNR by a factor of 10. In addition, it is important to understand that the SNR is limited by the laser that is used as a probe and detected by the photodiode. This is particularly important in the case of SRS, since only one of the lasers used (pump or Stokes) will serve as the probe beam, and therefore has to exhibit a low noise. The other laser is usually amplitude modulated and its contribution

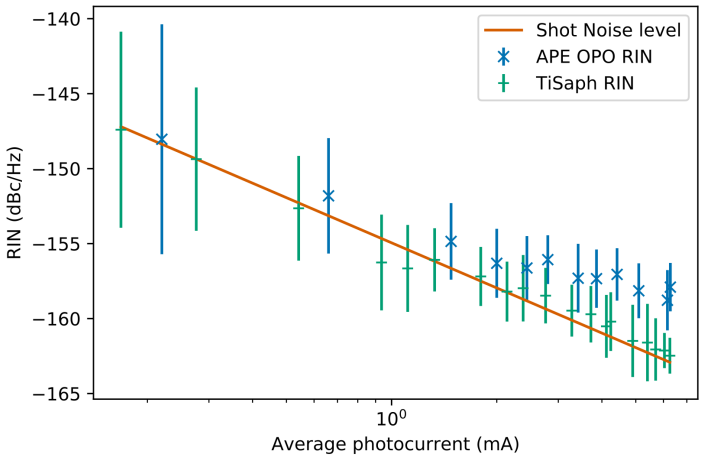

Figure 3.6 – Relative intensity noise (RIN) as a function of the average photodiode current I_{avg} for Device 1 (Ti:Saph) and 2 (Fiber laser pumped OPO). The RIN was averaged between 10 and 30 MHz.

to noise is negligible.

Complementary to this, once the SNR is limited by excess laser RIN, there is no advantage of increasing the probe laser power at the sample plane (and therefore the current of the photodiode I_{avg}). Since the SRS signal scales as the laser noise in this case, the SNR will not be improved by using higher laser power, as detailed in Section 3.4.3. In the case of shot noise limited RIN, higher laser probe power (and therefore larger I_{avg}) will increase the SNR. In our particular example of using Device 2 as our SRS probe, there is no need to push the intensity above several milliwatts (on the photodiode). However, in both cases (excess laser noise or shot noise limitation), it is always interesting to increase the optical intensity of the second (modulated) SRS laser to increase β and therefore the SNR, up to the point where sample damage threshold is reached.

With a lock-in integration time of $\tau = 20\,\mu$s, 20 MHz modulation, and average photo-current of $I_{avg} = 5\,$mA (i.e. 10 mW of laser power on the photodiode), the RIN of Device 1 and 2 are -162 and -157 dBc/Hz, respectively (Figure 3.6). Device 1 is therefore predicted to be at the shot noise limit (Equation 3.46):

$$\begin{aligned}\frac{\Delta I_{min}}{I_{avg}} &= \beta_{min} = \sqrt{8\Delta f RIN_{laser}(f_0, I_{avg})} \\ &= \sqrt{\frac{8}{2\pi\tau}\cdot\frac{2q}{I_{avg}}} = \sqrt{\frac{8}{2\pi\tau}10^{-16.2}} = 2.0\times10^{-6}\end{aligned} \tag{3.51}$$

And Device 2 is expected to be slightly less sensitive:

$$\frac{\Delta I_{min}}{I_{avg}} = \beta_{min} = \sqrt{8\Delta f RIN_{laser}(f_0, I_{avg})} = \sqrt{\frac{8}{2\pi\tau}10^{-15.7}} = 3.6 \times 10^{-6} \quad (3.52)$$

To reach such sensitivity with a fiber laser usually requires noise cancellation using balanced detection schemes [38, 41, 27].

When imaging biological samples and other diluted species, the number of Raman active molecules in the focal spot is such that to detect a signal, one needs to record each pixel for several microseconds or tens of microseconds. With such acquisition times, the maximum speed at which one can expect to do imaging is tens of thousands of pixels per second. The consequent rate will be a few frames per second with 100 by 100 pixel images.

We can anticipate that this limit will be overcome in two ways: first by reducing laser repetition frequency and increasing peak power, and second by developing spatial multiplexing in SRS. The first method would further increase β, the efficiency of the SRS process while making modulation more practical at half of the repetition frequency. In this case, low frequency noise would be extremely important to characterize in order to preserve the SNR. The limitation set by non linear photo-damage will also limit the amount of peak power that can be delivered to the sample. The second method, which involves developing spatial multiplexing in SRS, will be required if the time spent per pixel cannot be diminished further. One can increase the amount of information collected from the sample, and further increase the imaging speed, either by having multiple foci at once in the sample [42] or with other spatial multiplexing. In this case, several watts of power may be necessary to enable the SRS process to take place at multiple locations. This high power can currently be achieved with fiber lasers or optical parametric amplifiers. Again, the question of noise in such systems will be of prime importance to ensure optimal - shot noise limited - SNR.

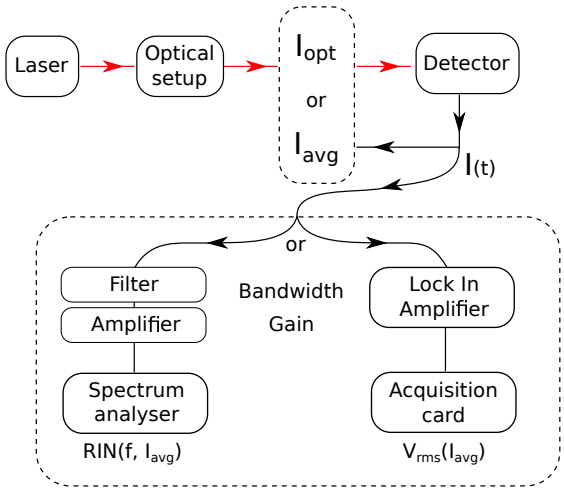

Figure 3.7 – Simplified RIN measurement protocol.

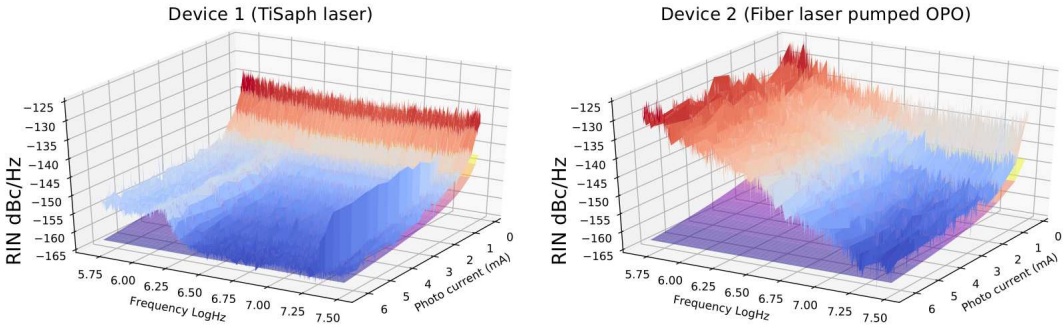

Figure 3.8 – RIN measured as a function of frequency (log(Hz)) and photodiode current (I_{avg} in mA) for Device 1 (right) and Device 2 (left). The peaks at 20 MHz in Device 1 is an example of a SRS signal. The purple surfaces correspond to the shot noise limited RIN.

4 Spectral focusing SRS

As we have discussed in Chapter 2, the shorter the pulse of light we send on a sample, the higher the electric field for a given average power. The higher the electric field, the greater the SRS signal and the better for any application.

With this reasoning, one would like to have the shortest possible light pulse. However, with shorter pulses comes an increasing number of spectral components. With a pulse of $1\,\mathrm{ps}$ for instance, the pulse contains a range of wavenumber of $14.7\,\mathrm{cm}^{-1}$ (assuming Gaussian Fourier limited pulses as in Section 4.2.1). For $100\,\mathrm{fs}$, the pulse has a span of $147\,\mathrm{cm}^{-1}$. With such spectrally broad pulses, it is difficult to target vibration levels of widths close to $10\,\mathrm{cm}^{-1}$. Spectral focusing will now be discussed, as it constitute a way to recover spectral resolution while using spectrally broad pulses.

The resolution in a femtosecond SRS system can be greatly enhanced by the use of spectral focusing, a technique that relies on applying dispersion to the optical pulses. With these chirped pulses, the different optical frequencies are no longer synchronized and will arrive at different times. Therefore, it is possible to tune which pair of frequencies from the pump and Stokes pulses will arrive on the sample simultaneously. This is illustrated in Figure 4.1 and explained in greater depth in this chapter.

Here we discuss the theoretical, numerical, and experimental approach to pulse engineering in our SRS system in details. We start by reviewing the literature concerning this technique, how it was applied to SRS, in addition to why grating pairs are a suitable technique for pulse chirping. The derivation of the equations behind a grating and a pair of gratings will follow. We will elaborate on the effects of dispersion on the pulses under the assumption that the pulses are Gaussian for simplification. This effect will be described numerically and compared to experimental results. The effect of dispersion on the SRS signal in terms of signal power and resolution is derived from the work of Jue Su and collaborators [43] and adapted to our use. Finally, the fine optimization of the SRS resolution and signal will be described.

4.1 Literature review

The term spectral focusing has had different uses in the past, but the first use related to our application was by Broers and collaborators in 1992 [44]. This team used chirped femtosecond pulses in the context of second harmonic generation to reduce the spectral range of the generated light. The first application to coherent Raman scattering was reported by Gershgoren and colleagues in 2003 [45], with an achieved resolution of $15\,\mathrm{cm}^{-1}$, 80 times higher than the laser bandwidth.

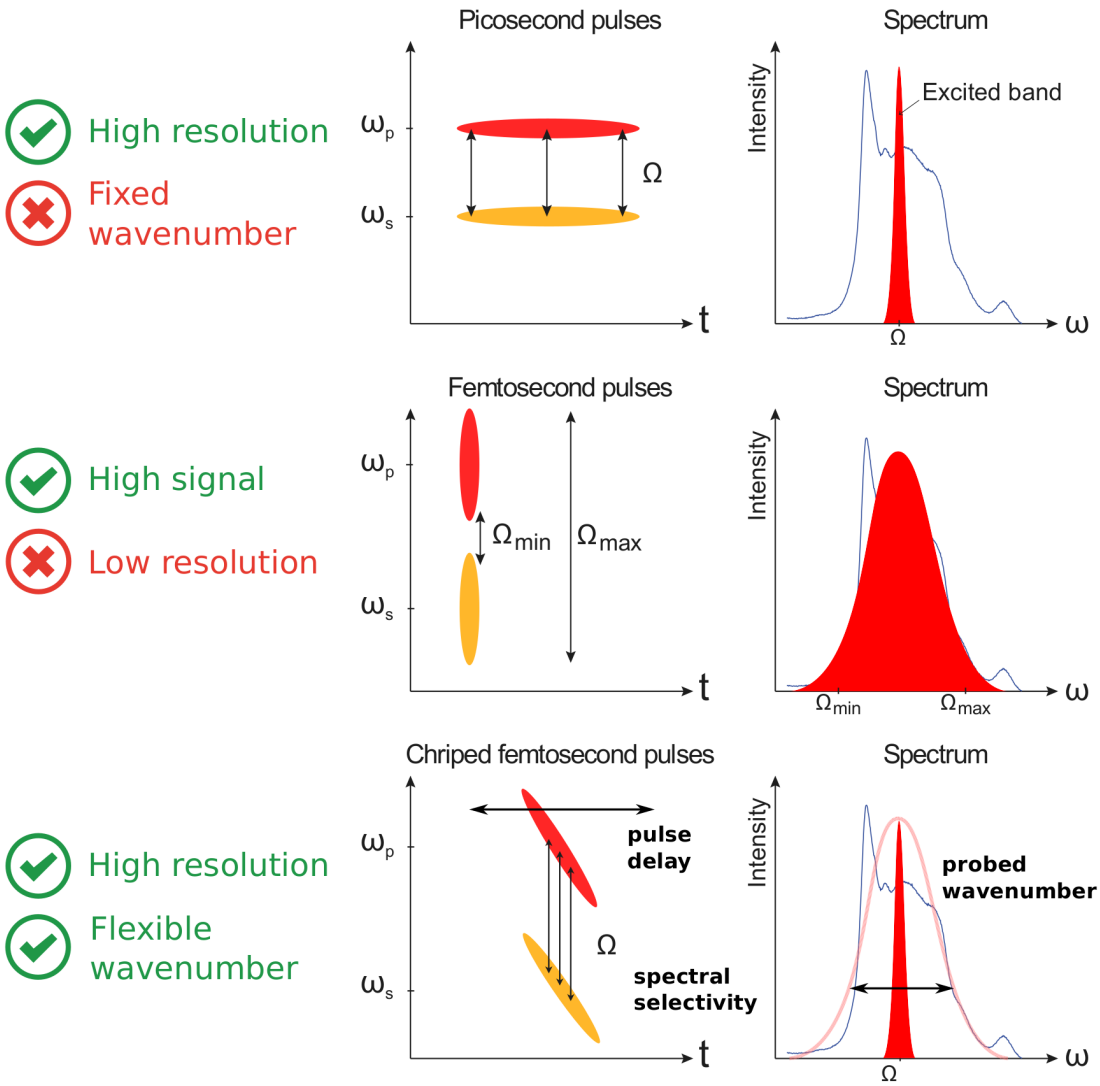

Figure 4.1 – Comparison between picosecond and femtosecond stimulated Raman scattering. With picosecond pulses (top) the pulses have a narrow spectral range. This leads to a well defined frequency difference between the pulse, which leads to high spectral resolution. In order to acquire a SRS spectrum the wavelength of one of the lasers has to change. With Fourier-limited femtosecond pulses (middle), the pulses have a broad spectral range and the entire spectrum is probed at the same time. This provides high signal, but low spectral resolution. Finally, with chirped femtosecond pulses (bottom), one particular wavenumber can be targeted within the range of wavenumbers accessible with femtosecond pulses. Moreover, this selected wavenumber can be tuned easily by changing the delay between the pump and the Stokes pulses.

This technique has then been used in CARS [46, 47, 48, 49, 50, 51], and later in SRS [52, 53, 54, 30, 55]. In today's literature, femtosecond SRS is almost exclusively performed with spectral focusing [29, 23, 21, 56].

There are several ways to imprint chirp on the pulses, but the most common is either the use of glass rods [47, 48, 49, 50, 51, 55] or gratings [46, 52, 30].

We will detail the many advantages of such schemes, but we will first describe the meaning of dispersion and provide a model of its phase effects on optical pulses.

4.2 Gaussian pulses theory

Typically, the pulses generated from a laser system that is using passive mode-locking with fast saturable absorber are hyperbolic secant pulses [57, 58]. However, as seen in Section 4.4.3, the pulses used within this research are more adequately described by Gaussian pulses as opposed to hyperbolic secants. Additionally, the mathematical aspects of phase and dispersion are simpler when considering Gaussian pulses.

4.2.1 Fourier-transform-limited pulses

We consider a classical electrical field with center angular frequency ω_0, and Gaussian envelope of parameter σ:

$$E(t) = E_0 \exp\left(-\frac{t^2}{2\sigma^2}\right)\exp(-j\omega_0 t) \tag{4.1}$$

We define a additional parameters that will have a physical interpretation:

$\Delta t_0 = 2\sigma\sqrt{\ln 2}$	Is the temporal full width at half maximum of our pulse.
$\Delta\omega = \frac{4\ln 2}{\Delta t_0}$	Is the spectral full width at half maximum of our pulse.
$A_0 = E_0\left[\frac{\Delta\omega}{\pi\Delta t_0}\right]^{\frac{-1}{4}}$	

With these definitions, the electric field becomes:

$$E(t) = A_0\left[\frac{\Delta\omega}{\pi\Delta t_0}\right]^{\frac{1}{4}}\exp\left(-\frac{\Delta\omega}{2\Delta t_0}t^2\right)\exp(-j\omega_0 t) \tag{4.2}$$

And the intensity:

$$|E(t)|^2 = |A_0|^2\left[\frac{\Delta\omega}{\pi\Delta t_0}\right]^{\frac{1}{2}}\exp\left(-\frac{\Delta\omega}{\Delta t_0}t^2\right) \tag{4.3}$$

We justify the physical interpretation of Δt_0 (temporal full width at half maximum) and A_0 (total intensity) by evaluating Equation 4.3 at $\pm\frac{1}{2}\Delta t_0$ and integra-

ting it over the time domain:

$$|E(\pm\tfrac{1}{2}\Delta t_0)|^2 = \frac{1}{2}|E(0)|^2 \qquad\qquad \int_{-\infty}^{+\infty}|E(t)|^2 \mathrm{d}t = |A_0|^2$$

When passing into the Fourier domain, the pulse becomes :

$$E(\omega) = \frac{1}{\sqrt{2\pi}}\int_{-\infty}^{+\infty} A_0\left[\frac{\Delta\omega}{\pi\Delta t_0}\right]^{\frac{1}{4}} \exp\Big(-\frac{\Delta\omega}{2\Delta t_0}t^2\Big)\exp(j(\omega-\omega_0)t)\mathrm{d}t$$

It's an integral of the form $\int_{-\infty}^{+\infty}\exp\Big(\alpha t - \frac{\beta}{2}t^2\Big)\mathrm{d}t = \left[\frac{2\pi}{\beta}\right]^{\frac{1}{2}}\exp\left(\frac{\alpha^2}{2\beta}\right)$ with $\alpha = j(\omega-\omega_0)$ and $\beta = \frac{\Delta\omega}{\Delta t_0}$ Hence:

$$E(\omega) = A_0\left[\frac{\Delta t_0}{\pi\Delta\omega}\right]^{\frac{1}{4}}\exp\Big(-\frac{\Delta t_0}{2\Delta\omega}(\omega-\omega_0)^2\Big) \tag{4.4}$$

From Equation 4.4 we justify the physical interpretation of $\Delta\omega$ as being the spectral full width at half maximum:

$$|E(\omega_0 \pm \tfrac{1}{2}\Delta\omega|^2 = \frac{1}{2}|E(\omega_0)|^2$$

4.2.2 Effect of first and second order phase

The previous section described the case of a perfect Fourier-limited Gaussian pulse, which is of course an approximation. In particular, in Equation 4.4 the various spectral components of the optical pulse have the same phase, which would be the ideal case. While the pulse is propagating, these different components will acquire different phases ϕ that depend on ω:

$$E(\omega) = A_0\left[\frac{\Delta t_0}{\pi\Delta\omega}\right]^{\frac{1}{4}}\exp\Big(-\frac{\Delta t_0}{2\Delta\omega}(\omega-\omega_0)^2\Big)\exp(j\phi(\omega))$$

We will now derive how this phase is related to the propagation and dispersion of the pulse, meaning the relationship between this phase in the spectral domain and its interpretation in time domain. If we consider that our pulses contain only a limited span of frequencies $\Delta\omega$ around the center frequency ω_0 ($\Delta\omega << \omega_0$), we can perform a second order Taylor expansion of the phase ϕ with respect to ω around ω_0:

$$E(\omega) = A_0\left[\frac{\Delta t_0}{\pi\Delta\omega}\right]^{\frac{1}{4}}\exp\Big(\frac{\Delta t_0}{2\Delta\omega}(\omega-\omega_0)^2\Big)\exp\Big(j\Big(\phi(\omega_0)+\phi'(\omega_0)(\omega-\omega_0) + \frac{1}{2}\phi''(\omega_0)(\omega-\omega_0)^2\Big)\Big)$$

We merge the zero order phase development inside the complex amplitude : $B_0 \equiv A_0 \exp\big(j\phi(\omega_0)\big)$

$$E(\omega) = B_0\Big[\frac{\Delta t_0}{\pi\Delta\omega}\Big]^{\frac{1}{4}} \exp\Big(j\phi'(\omega_0)(\omega-\omega_0) - \frac{1}{2}\Big(\frac{\Delta t_0}{\Delta\omega} - j\phi''(\omega_0)\Big)(\omega-\omega_0)^2\Big)$$

Now, in time domain :

$$E(t) = \frac{1}{\sqrt{2\pi}}\int_{-\infty}^{+\infty} B_0\Big[\frac{\Delta t_0}{\pi\Delta\omega}\Big]^{\frac{1}{4}} \exp\Big(j\phi'(\omega_0)(\omega-\omega_0) - \frac{1}{2}\Big(\frac{\Delta t_0}{\Delta\omega} - j\phi''(\omega_0)\Big)(\omega-\omega_0)^2\Big)\exp(-j\omega t)\mathrm{d}\omega$$

changing ω to $\omega_0 + \omega$

$$E(t) = \frac{1}{\sqrt{2\pi}}\int_{-\infty}^{+\infty} B_0\Big[\frac{\Delta t_0}{\pi\Delta\omega}\Big]^{\frac{1}{4}} \exp\Big(j\Big(\phi'(\omega_0) - t\Big)\omega - \frac{1}{2}\Big(\frac{\Delta t_0}{\Delta\omega} - j\phi''(\omega_0)\Big)\omega^2\Big) \times \exp(-j\omega_0 t)\mathrm{d}\omega$$

It is an integral of the form $\int_{-\infty}^{+\infty}\exp\Big(\alpha\omega - \frac{\beta}{2}\omega^2\Big)\mathrm{d}\omega = \Big[\frac{2\pi}{\beta}\Big]^{\frac{1}{2}}\exp\Big(\frac{\alpha^2}{2\beta}\Big)$ with $\alpha = j\Big(\phi'(\omega_0) - t\Big)$ and $\beta = \Big(\frac{\Delta t_0}{\Delta\omega} - j\phi''(\omega_0)\Big)$

$$E(t) = B_0\Big[\frac{\Delta t_0\Delta\omega}{\pi\Big(\Delta t_0 - j\phi''(\omega_0)\Delta\omega\Big)^2}\Big]^{\frac{1}{4}} \exp\Big(-\frac{1}{2}\frac{\Delta\omega\Big(\phi'(\omega_0)-t\Big)^2}{\Big(\Delta t_0 - j\phi''(\omega_0)\Delta\omega\Big)}\Big)\exp(-j\omega_0 t)$$

Let us define a chirp parameter $C \equiv \frac{\phi''(\omega_0)\Delta\omega}{\Delta t_0}$. We find:

$$E(t) = B_0[\frac{\Delta\omega}{\pi\Delta t_0(1-jC)^2}\Big]^{\frac{1}{4}} \exp\Big(-\frac{(1+jC)}{2}\frac{\Delta\omega\Big(t-\phi'(\omega_0)\Big)^2}{\Delta t_0(1+C^2)}\Big)\exp(-j\omega_0 t)$$

With these notations, we can deduce that we now have a Gaussian pulse delayed by a time $t_0 \equiv \phi'(\omega_0)$, and with the modified duration (full width at half maximum) $\Delta t = \Delta t_0\sqrt{1+C^2}$:

$$|E(t)|^2 = |A_0|^2\Big[\frac{\Delta\omega}{\pi\Delta t_0(1+C^2)}\Big]^{\frac{1}{2}} \exp\Big(-\frac{\Delta\omega}{\Delta t_0(1+C^2)}(t-t_0)^2\Big)$$

$$|E(t_0 \pm \tfrac{1}{2}\Delta t)|^2 = \frac{1}{2}|E(0)|^2 \qquad \int_{-\infty}^{+\infty}|E(t)|^2\mathrm{d}t = |A_0|^2$$

When compared to the original pulse, the peak amplitude of the envelope is slightly lower by a factor of $\sqrt{1+C^2}$. Within this envelope, the instantaneous

carrier angular frequency $\tilde{\omega}$ of is a function of time given by:

$$\tilde{\omega}(t) = \omega_0 + \frac{C}{1+C^2}\frac{\Delta\omega}{2\Delta t_0}(t - t_0) \tag{4.5}$$

To summarize

When adding a frequency dependent phase $\phi(\omega)$ on a Gaussian, Fourier-limited pulse, one adds:

— A global phase $\phi(\omega_0)$ which doesn't affect the intensity.
— A time delay $\phi'(\omega_0)$ that accounts for propagation of the pulse.
— A quadratic phase $\phi''(\omega_0)$ responsible for dispersion of the frequencies and temporal stretching of the pulses.

Under such conditions we have defined the following quantities :

— ω_0 the center angular frequency of the pulse
— $\Delta\omega$ the spectral full width at half maximum of our pulse.
— $\Delta t_0 \equiv \frac{4\ln 2}{\Delta\omega}$ the temporal full width at half maximum of our pulse under no dispersion.
— A_0 the total pulse complex amplitude.
— $C \equiv \frac{\phi''(\omega_0)\Delta\omega}{\Delta t_0}$ a parameter characterizing the amount of dispersion.
— $\Delta t \equiv \Delta t_0\sqrt{1+C^2}$ the temporal full width at half maximum with dispersion.

In Section 4.5, we will see what effect the dispersion has on the SRS process described in Chapter 2.

4.3 Grating theory

4.3.1 Dispersion methods, glass, prisms, gratings

In order to imprint dispersion on optical pulses, one needs to introduce a second order phase. There are several ways of doing this:

The most direct way would be to use dispersive materials in which the refractive index is a function of the wavelengths: $n(\lambda)$. This translates into a second order phase, as the different wavelengths experience different optical paths. Most materials show non zero group velocity dispersion (GVD), which is the group delay dispersion (GDD) per unit length, usually expressed in $\mathrm{fs}^2\,\mathrm{mm}^{-1}$. For example, the group velocity dispersion of silica is $36\,\mathrm{fs}^2\,\mathrm{mm}^{-1}$ at $800\,\mathrm{nm}$ and $-28\,\mathrm{fs}^2\,\mathrm{mm}^{-1}$ at $1550\,\mathrm{nm}$. If the GVD is negative, the material is said to have negative (or normal) dispersion. If it is positive, we refer to positive (or anomalous) dispersion.

Having a pulse go through a medium such as silica can lead to a dispersed pulse at the output. However, the amount of dispersion we will need to imprint on our pulses is of the order of $6 \times 10^4\,\mathrm{fs}^2$. Using silica to imprint such chirp

would require several meters of glass. Other materials with much higher GVD could be used to reduce this length to less than a meter of glass. Dense flint glass, SF57 for instance, has a GVD of $223.58\,\mathrm{fs}^2\,\mathrm{mm}^{-1}$ at $800\,\mathrm{nm}$, and only $27\,\mathrm{cm}$ of this material is required to apply the same amount of dispersion [56, 23]. Optical fibers with are also suited for this application but can introduce significant losses.

While dispersive materials are sufficient, they suffer from several drawbacks that make their use cumbersome in research, such as high losses and lack of tunability. To change the GDD, one must change the length of the material or optical fiber.

Another approach is to use prism pairs. With this technique, the dispersion is not exactly due to difference in velocity, but to the fact that different wavelengths going through a prism will be refracted with different angles. By having each angle see a different optical path, we achieve dispersion with a tunable system as opposed to propagation in dispersive materials. With a prism pair implementation, the dispersion is tuned by adjusting the distance between the two prisms, as opposed to cutting several lengths of dispersive material. However, the amount of dispersion required in spectral focusing is such that the prism distance required for appropriate dispersion can reach several meters.

The third most common approach is to use grating pairs, as we will implement in this analysis. With gratings pairs, one also uses angular dispersion to delay the different wavelengths. However, with the proper gratings the distance required to apply the same amount of dispersion is only few centimeters as we will detail in Section 4.4.3. Both grating and prism pairs add negative second order phase on the pulses; gratings add a positive third order phase, while prisms add negative third order. These two systems can be combined to compensate for third order effects in ultra-short pulse applications. We describe below the principle behind the grating pairs, and make the calculations to determine the phase applied to our pulse. We will only focus on only second order phase.

4.3.2 Grating theory

A simple model for a grating is a set of lines which diffract light, each separated by a distance d called the grating parameter. We consider a monochromatic plane wave arriving on the surface with an incidence angle γ. Each line diffracts light in all directions, and the light from all lines interfere in the far field (Frauhoffer diffraction). The calculations for multi-wave coherent interference has been derived many times and can be summarized as each line adding coherently with its neighbor. The optical path difference between two "light rays" intersecting two neighboring lines must be a multiple of the wavelength. As illustrated in Figure 4.2, the optical path difference is $d\sin(\gamma) - d\sin(\theta_m)$. Therefore, the angle θ_m has to satisfy the grating condition:

$$\sin(\theta_m) = \sin(\gamma) - m\lambda/d \tag{4.6}$$

m is the diffraction order. We consider $m = 1$ always, and simplify by omitting it and writing the diffraction angle θ.

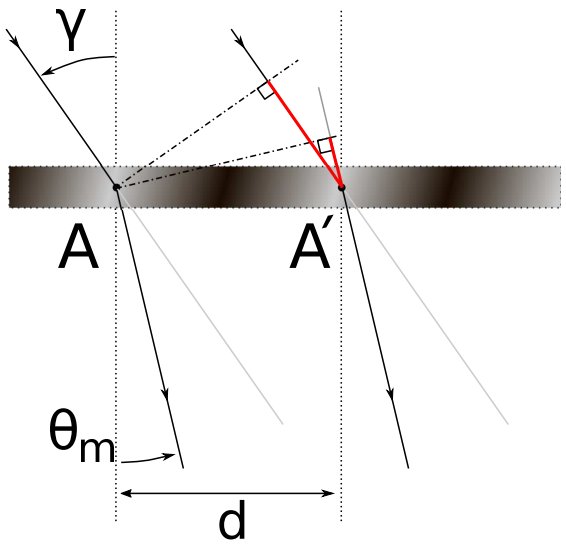

Figure 4.2 – Schematics of the grating

In the case of multiple wavelengths arriving on the grating, each must verify the grating condition and each will be diffracted at a different angle $\theta(\omega)$. This angular spread is then used to make each wavelength experience a different optical path.

4.3.3 Grating pairs

The individual wavelengths are sent in different directions from the first grating. This makes it easier to address each wavelength independently from the others. However, this provides an additional challenge as the laser beam will be divergent, so a second grating is placed parallel to the first one, at a distance equal to L (Figure 4.3). The grating condition (Equation 4.6) is automatically met on this second grating due to these alternating angles, and all wavelengths are therefore diffracted in a collimated beam, with wavelength varying across the beam spatially.

Consequently, the total distance traveled by each wavelength is different. In particular, the "blue" light will go through a much shorter path than the "red" ones, which will meet the necessary goal for our dispersion analyses. In a single pass however, the individual wavelengths will be spread across the width of the optical pulse, which is why a retro-reflector is used to send the light back in the direction it came from. The double pass compensates the lateral spread, and also spatially separate the reflected beam from the incoming one by shifting the latter above the former one.

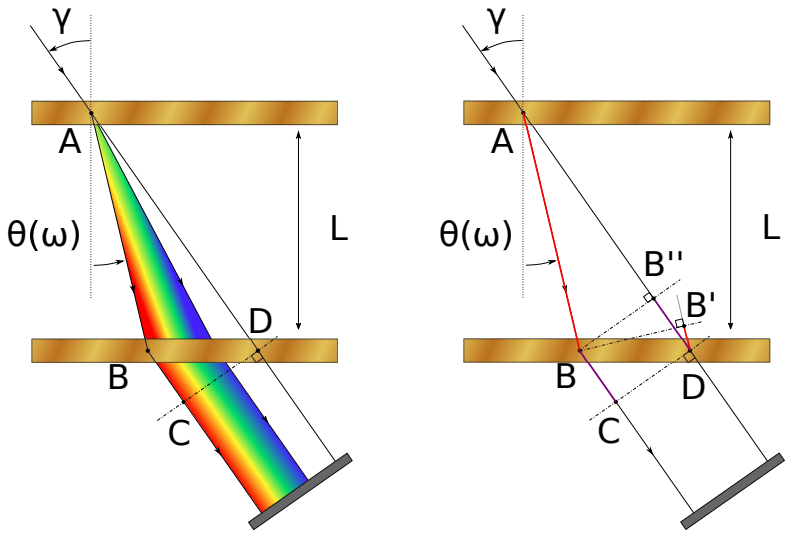

Figure 4.3 – Schematics of the grating pair. The pulse arrives from the top, each wavelength is diffracted once at an angle θ, diffracted by the second grating back at the angle γ, and then hits the mirror and follows the exact same path back. The left figure illustrates the wavelengths spreading across different angles. The right figure illustrates the origin of the phase step acquired by the wave at point B.

In order to quantify the second order phase introduced by a grating pair, one needs to derive the phase applied by this system as a function of angular frequency. Let us look at a wave propagating from point A, as illustrated in Figure 4.3. From A to B, the wave is propagating with a phase velocity $\frac{\omega}{c}$, so $\phi(A \rightarrow B) = \frac{\omega}{c}\overline{AB}$. There is also propagation from B to C, introducing a phase $\phi(B \rightarrow C) = \frac{\omega}{c}\overline{BC}$. It is tempting to simply add those two phases acquired by a wave propagating from A to C. However, the grating phase matching condition is such that the grating introduces an additional phase when the light is diffracted. This phase term was introduced by Treacy [59] in 1969.

When arriving at the point B, the light is on the same wavefront as the light arriving in B' with the same direction. When leaving point B, the light is on the same phase front as the light leaving from B'' towards point D. The light in point B therefore acquires a phase retardance equal to the phase difference between phase fronts at point B' and B'':

$$\begin{aligned}\phi(grating) &= \frac{\omega}{c}(\overline{B'D} - \overline{B''D}) \\ &= \frac{\omega}{c}\overline{BD}(\sin(\theta) - \sin(\gamma)) \\ &= -\frac{2\pi\overline{BD}}{d}\end{aligned}$$

The final phase of the light going from point A to point C is finally:

$$\begin{aligned}\phi(A \to C) &= \phi(A \to B) + \phi(B \to C) + \phi(grating) \\ &= \frac{\omega}{c}\overline{AB} + \frac{\omega}{c}\overline{BD}\sin(\gamma) - \frac{2\pi\overline{BD}}{d} \\ &= \frac{\omega}{c}\Big(\overline{AB} + \overline{BD}\sin(\theta)\Big) \\ &= \frac{\omega}{c}\Big(\frac{L}{\cos(\theta)} + L(\tan(\gamma) - \tan(\theta))\sin(\theta)\Big)\end{aligned}$$

In order to derive the phase with respect to angular frequency, it is important to remember that the angle of diffraction θ is a function of frequency. With Equation 4.6 we can derive:

$$\begin{aligned}\frac{d\theta}{d\omega} &= \frac{2\pi c}{\omega^2 d\cos(\theta)} \\ \frac{d}{d\omega} &= \frac{2\pi c}{\omega^2 d\cos(\theta)}\frac{\partial}{\partial\theta} + \frac{\partial}{\partial\omega}\end{aligned}$$

The first order phase is therefore:

$$\begin{aligned}\phi'(\omega) &= \frac{d\phi}{d\omega} \\ &= \frac{d\theta}{d\omega}\frac{\partial\phi}{\partial\theta} + \frac{\phi}{\omega} \\ &= \frac{2\pi L}{\omega d}\Big(\tan(\gamma) - \tan(\theta)\Big) + \frac{\phi}{\omega}\end{aligned}$$

The second order phase is:

$$\begin{aligned}\phi''(\omega) &= \frac{d^2\phi}{d\omega^2} \\ &= -\frac{2\pi L}{\omega^2 d}\Big(\tan(\gamma) - \tan(\theta)\Big) - \frac{4\pi^2 Lc}{\omega^3 d^2\cos^3(\theta)} - \frac{\phi}{\omega^2} + \frac{\phi'}{\omega} \\ &= -\frac{4\pi^2 Lc}{\omega^3 d^2\cos^3(\theta)}\end{aligned}$$

Since we focus on the second order derivative at ω_0 the second order phase

applied on the pulse for a double pass is:

$$\phi''(\omega_0) = -2\frac{4\pi^2 cL}{d^2\omega_0^3 cos^3(\theta(\omega_0))} \tag{4.7}$$

Using what we previously derived in Section 4.2.1, we can express $\phi''(\omega_0)$ in terms of the other parameters :

$$\phi''(\omega_0) = C\frac{\Delta t_0}{\Delta\omega} \qquad \text{and} \qquad \Delta t = \Delta t_0\sqrt{1+C^2}$$

We can therefore link the grating distance and the pulse duration :

$$\Delta t = \Delta t_0\sqrt{1+(\frac{2L\lambda_0\Delta\lambda}{c\Delta t_0 d^2 cos^3(\theta_0)})^2}$$

We can now measure the pulse FWHM at the sample plane and compare it with the model for different grating distances.

4.4 Pulse chirping

4.4.1 Laser sources

The laser system used in this work is detailed in Chapter 6. Here, we summarize the specifications of the pump and Stokes laser which will be used in the following measurements.

The pump beam is provided by a Titanium Sapphire (TiSaph) laser (Chameleon OPO-VIS, Coherent). The device delivers femtosecond pulses, typically $140\,\mathrm{fs}$ according to the specifications, which are tuned to $800\,\mathrm{nm}$.

The Stokes beam consists of an optical parametric oscillator (OPO) pumped by the TiSaph laser. The OPO pulses are tuned around $1045\,\mathrm{nm}$, and their typical duration is $200\,\mathrm{fs}$ according to the specifications.

4.4.2 Pulse characterization

Following the discussion of the theory of grating pairs, we want to numerically simulate and experimentally measure the way the pulses are stretched by this system. In order to do so, we need to characterize the different pulse characteristics : Δt_0, $\Delta\lambda$, λ_0, and θ_0. $\Delta\lambda$ and λ_0 are measured using a spectrometer (QE65 Pro, Ocean Optics, Largo USA) and reported in Table 4.1.

For the grating pairs, we use custom transmission gratings (Wasatch Photonics, USA), with 600 lines per millimeter and optimized for $900\,\mathrm{nm}$ wavelengths. The efficiency of the gratings around our wavelengths of interest is still above 90%. The incident angle γ was chosen to optimize the diffraction in the first order,

which gives θ_0 with Equation 4.6 and can be added to Table 4.1 once confirmed experimentally. The second grating is coarsely set parallel to the first one, then finely tuned to ensure the best diffraction efficiency. Next, we add a retro-reflector to send the light back through the grating pair. The retro-reflector is set such that the optical axis of the output pulse is shifted upwards by roughly $2\,\mathrm{cm}$ with respect to the incoming one. The second grating and retro-reflector are mounted on a translation line parallel to the beam inside the grating pair, allowing one to change the grating distance without affecting the alignment significantly.

4.4.3 Temporal width measurement

We then measure the output pulse temporal width Δt, at the sample plane, as a function of L the grating distance.

This measurement is performed with an auto-correlator (pulseCheck, APE, Berlin Germany) which gives the auto-correlation function of the pulses in the temporal domain. In order to retrieve the temporal full width at half maximum (i.e. duration) of our pulses from the auto-correlation function, it is necessary to make an assumption of the temporal shape of the pulse. Lazaridis and collaborators [60] compared the effect of dispersion on hyperbolic secant and Gaussian pulses. The time-bandwidth product (TBWP) for these types of pulses behave differently when the chirp factor increases.

The auto-correlator provides the temporal FWHM under both Gaussian and secant assumptions. We multiply this value with the frequency FWHM to obtain the experimental TBWP. This value is plotted in Figure 4.4 for different values of the distance between the gratings, which we transform into the chirp factor using Equation 4.7. The pulses behave like Gaussian pulses, which justifies the Gaussian assumption.

The experimental curve $\Delta t(L)$ is shown in Figure 4.5. Δt_0 is given by the minimum of the curves, and reported in Table 4.1. This value is equal (within the error range) to the theoretical value for unchirped Gaussian pulses with spectral width $\Delta\lambda$.

System	λ_0 (nm)	$\Delta\lambda$ (nm)	θ (degrees)	Δt_0 (fs)	$\delta\phi''$ (kfs^2)
Ti:Sapphire	800±1	6.1±0.2	10±1	155±4	2±0.5
OPO	1045±1	10.2±0.2	19±1	157±4	12±1

Table 4.1 – Summary of the optical pulses characteristics.

4.4.4 Ad-hoc adjustments

We measure that the pulse temporal lengths are actually minimal for a specific distance between the gratings. This is an indication that the pulses acquire a significant positive chirp in the absence of the grating pairs. This can be explained

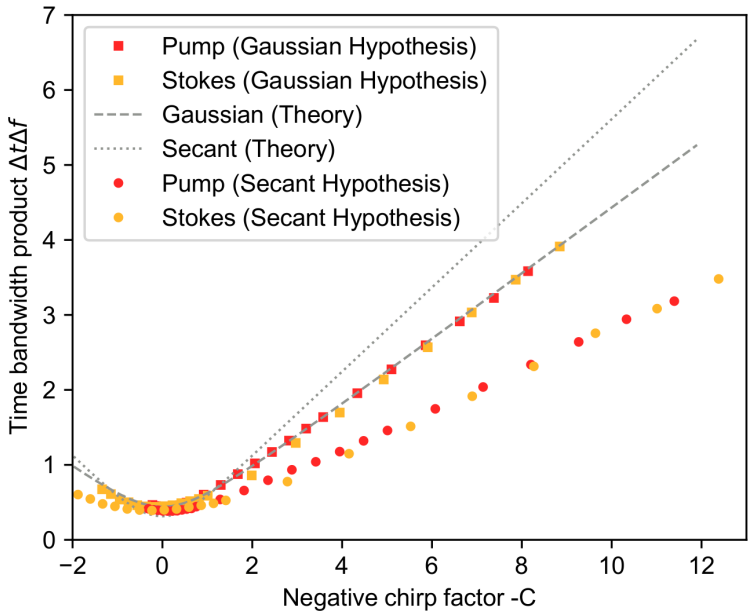

Figure 4.4 – Time-Bandwidth Product (TBWP) of the pump and Stokes pulse as a function of the chirp factor. In gray lines the theoretical values assuming Gaussian (dashed) and Secant (dotted) pulses. The experimental results for the pump (red) and Stokes (orange) are plotted assuming Gaussian (squares) or Secant (circles) pulses. The experimental data only matches the theory when we assume our pulses are Gaussian.

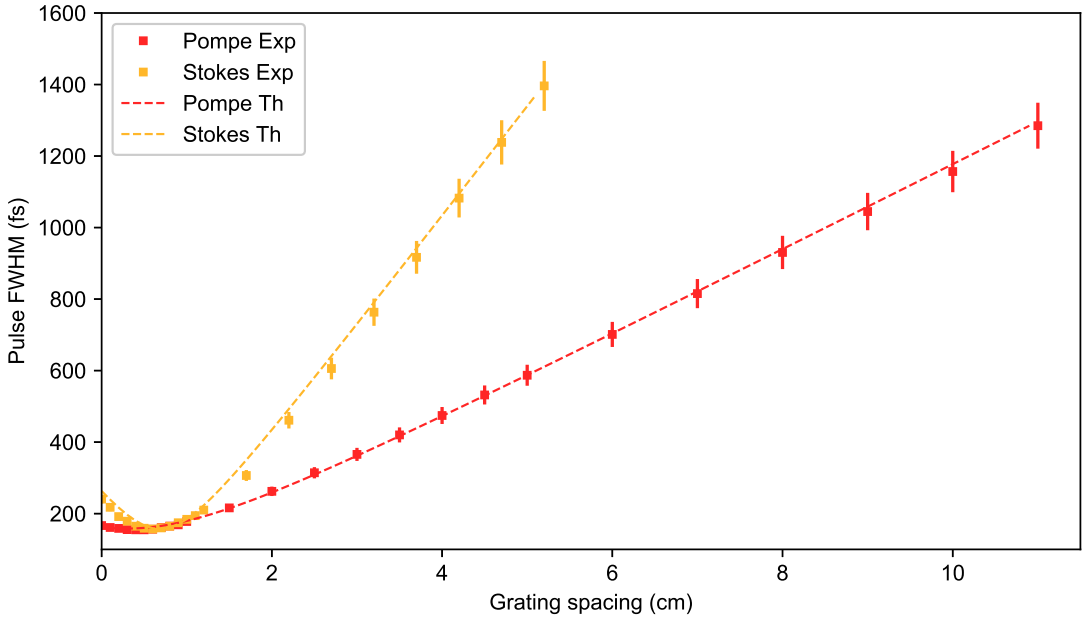

Figure 4.5 – Temporal width of the pump (red) and Stokes (orange) pulses with increasing grating spacing L. The experimental data (squares) matches well with the model (dashed lines) representing chirped Gaussian pulses. The offset of the model in the X-axis is manually fitted.

by the optical components in the optical setup, which introduce positive dispersion that needs to be compensated for with the appropriate grating distance before negative dispersion can be added.

4.5 SRS Resolution and Gain with chirped pulses

We have mentioned previously that chirped pulses can be used to increase spectral resolution in SRS with femtosecond pulses. In order to go from this qualitative statement to a quantitative measure of resolution gain, one needs to derive the equations relative to SRS generation.

4.5.1 Resolution

Jue Su and collaborators have previously discussed the way SRS happens in the presence of chirped pulses [43]. We will base our analysis on their model and adapt it to our pulses, which have different characteristics (Table 4.1).

The best resolution, and smallest losses, are achieved when the two pulses have the same second order phase derivative. This will correspond to two optimum chirp factors, C_p and C_s, for the pump and Stokes, respectively. Under

these conditions, the effective resolution is:

$$\Delta\omega = \sqrt{\frac{\Delta\omega_p^2}{1+C_p^2} + \frac{\Delta\omega_s^2}{1+C_s^2}}$$

The theoretical resolution obtained by applying chirp on our pulses is plotted in Figure 4.6. We can see that, by going towards picosecond pulses, we are able to retrieve the resolution power available with such "long" pulses.

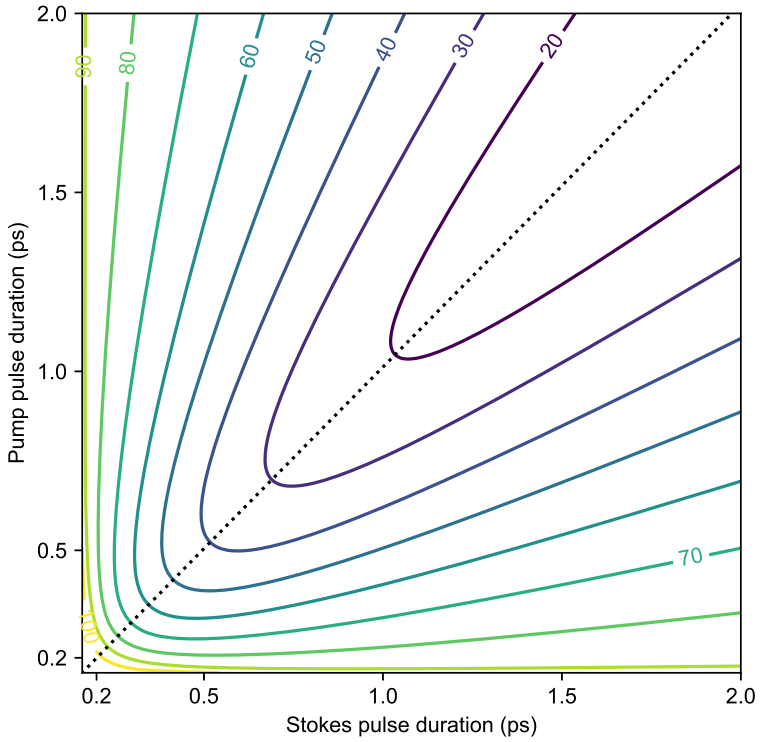

Figure 4.6 – Spectral resolution (in cm^{-1}) as a function of the pump and Stokes pulse duration. The numbered lines indicate the obtained resolution. The dotted line represents the optimal scheme in which pump and Stokes have the same second order phase.

However, short and ultra-short pulses have been used in SRS in the first place in order to increase the signal by having intense electric fields. When lengthening the optical pulses, the electric field amplitude is diminished, and we can expect a drop in SRS power. As shown in Figure 4.7, the amplitude of the signal is significantly dampened by several decibels as the resolution improves. The damping has two components: the drop in electric field amplitude and the reduced range of probed frequency. For instance, if a species has a constant spectrum (or infinite linewidth), the SRS signal will drop significantly as most of the spectrum is

no longer probed due to increased resolution. If the species has a sharp spectrum (or small linewidth), chirping the pulses does not change the fact that the whole spectrum is still probed until the resolution of the chirped pulses drops below the linewidth.

This is illustrated in Figure 4.7, where the SRS signal drop is plotted as a function of pulse length for different spectral line widths. In a more realistic scenario, the linewidth of the molecular vibrations in the lipid band is to the order of $25\,\mathrm{cm}^{-1}$. We can select a spectral resolution of $20\,\mathrm{cm}^{-1}$ by stretching pump and stokes pulses to $1\,\mathrm{ps}$. In this situation, the drop in SRS signal we expect from the lipid band lines is only $3\,\mathrm{dB}$, much smaller than the $8\,\mathrm{dB}$ expected for infinite linewidths.

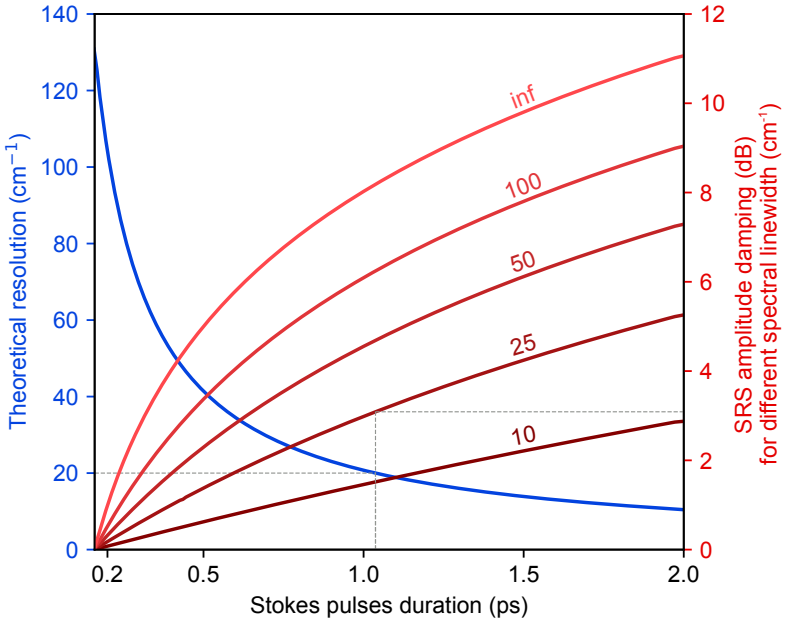

Figure 4.7 – Theoretical resolution (blue, left axis) and signal losses (red, right axis) for different Stokes pulse duration (the pump duration is chosen to optimize resolution). The theoretical resolution improves as the pulses are stretched, and does not depend on the sample. The signal loss gets worse as the pulse length increases and is worse for samples with larger linewidths (expressed in cm^{-1}).

4.5.2 Measurement of addition GVD due to optics

As mentioned in Section 4.4.4, there is extra (positive) dispersion added by the optics. The lenses and objectives inside our microscope add additional dispersion that require compensation to ensure optimal chirp of the sample. For instance, the group velocity dispersion of silica is $36\,\mathrm{fs}^2\,\mathrm{mm}^{-1}$ and $18\,\mathrm{fs}^2\,\mathrm{mm}^{-1}$ for $800\,\mathrm{nm}$ and $1045\,\mathrm{nm}$ respectively. Assuming all of our optics are silica, this

means roughly $5\,\mathrm{cm}$ of material. Combined, this gives the order of magnitude of $2000\,\mathrm{fs}^2$ group delay dispersion for our pulses. This can be compared to the amount of GDD introduced by our grating pairs, which is $60 \times 10^3\,\mathrm{fs}^2$ for $20\,\mathrm{cm}^{-1}$ resolution. Therefore, the GDD of the optics is quite small compared to the GDD necessary for spectral focusing, but is accounted for in order to maximize the resolution.

Since the GDD added by optics is a function of the wavelength, it is important to adjust the dispersion on the pump and Stokes pulses to ensure that the two arrive at the sample with the same second order phase. Otherwise, the resolution of the system will not be optimal as indicated in Figure 4.1.

4.5.3 Optimization of the second order phase to maximize resolution

In order to ensure optimal resolution, we measure the pulse length with the auto correlator directly on the sample plane, without the objective. This accounts for the lenses in the setup, but not the microscope objective. By setting the pulse lengths to $1\,\mathrm{ps}$ each (corresponding to a grating distance L of 4.3 and $9.3\,\mathrm{cm}$ for the Stokes and pump, respectively) we expect the resolution of our system be $20\,\mathrm{cm}^{-1}$.

In order to verify this value experimentally, and fine tune the pulse dispersion, we use a sample of Dimethyl sulfoxide (DMSO). The DMSO has two relatively sharp peaks on the lipid band at 2913 and $2994\,\mathrm{cm}^{-1}$. From previous studies, the linewidth of these resonances is estimated to be 5.4 and $9.4\,\mathrm{cm}^{-1}$ at room temperature, respectively [61].

We are able to recover the spectrum using either a mechanical delay line or a fast acousto optic delay line, and will elaborate further on this latter method in Chapter 6.

We target the $2913\,\mathrm{cm}^{-1}$ line of DMSO using the mechanical delay line to acquire the spectral data. We observe (Figure 4.8) that the width of the spectral line acquired with this technique is optimal for a grating distance close to $9.3\,\mathrm{cm}$, as predicted from our model. The resolution obtained is $25\,\mathrm{cm}^{-1}$, which is slightly worse than the expected resolution of $20\,\mathrm{cm}^{-1}$. It is possible that the linewidth of the DMSO is slightly larger in our experimental SRS setup using high laser power than in the one reported using spontaneous Raman spectroscopy at room temperature, and would artificially increase the measured resolution. A finer tuning of the second order phase will be demonstrated in Chapter 6.

With this approach we can ensure that we have a great understanding and control over our optical pulses, and that our system is working at the best of it's theoretical capabilities.

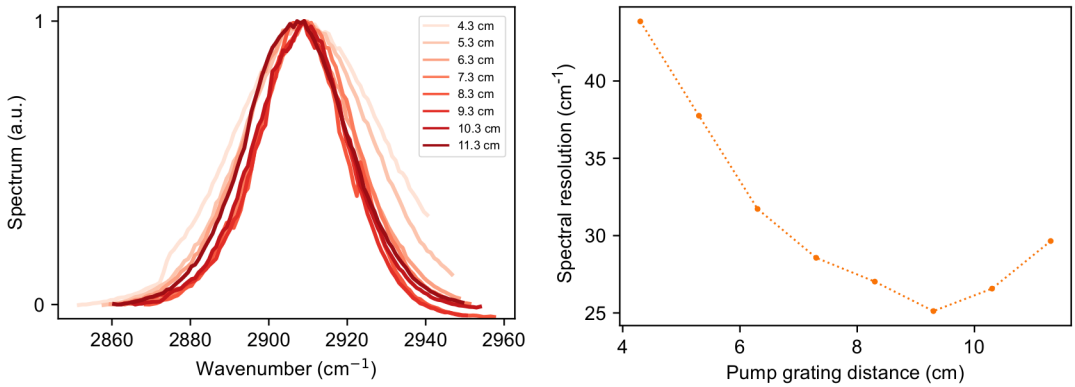

Figure 4.8 – Left: SRS spectrum of DMSO acquired with the mechanical delay line for different grating distance on the pump beam. Right: Optimization of the grating distance to ensure optimal resolution.

4.6 Discussion

In this chapter, we described how our pulses can be modeled with Gaussian envelopes and derived the relationship between the phase of the different optical frequencies and the temporal shape of the pulses. In particular, the first order phase is equivalent to delaying the time of arrival of the pulse, while the second order phase corresponds to a time-dependent frequency within the pulse. This chirping of the pulse can be used to improve the spectral resolution in SRS, similar to what has been done since 2003 in several systems. We analyzed the resolution obtained with our system, both numerically and experimentally, and optimized it to achieve an optimal spectral resolution of at least $25\,\mathrm{cm}^{-1}$. With such resolution comes a loss in SRS signal, which depends on the width of the resonance we are probing. This loss is estimated to be around 3 to $5\,\mathrm{dB}$ for most samples.

4.6.1 Presence of third order phase

Only second order phases have been discussed above, as a third order phase would slightly impair the resolution of the system. Although the effects of a third order system were identified as negligible in our configuration, we can expect that this would become a problem when attempting SRS with shorter pulses, in which case improved control would be required to maintain optimal resolution.

5 The AOPDF delay line

Chapter 4 detailed how one can retrieve spectral resolution in a SRS system consisting of two pulses. The resolution is obtained by applying dispersion to the pump and stokes pulses such that their instantaneous frequencies (ω_p and ω_s respectively) are a linear function of time:

$$\omega_p(t) = \omega_{p,0} + \alpha t \tag{5.1}$$
$$\omega_s(t) = \omega_{s,0} + \alpha t \tag{5.2}$$

With such dispersion, the probed SRS center frequency $\Omega = \omega_p - \omega_s$ can be adjusted by adding a time delay τ between the two optical pulses:

$$\Omega(\tau) = \omega_p(t+\tau) - \omega_s(t) = (\omega_{p,0} - \omega_{s,0}) + \alpha\tau = \Omega_0 + \alpha\tau \tag{5.3}$$

This chapter introduces the acousto-optic programmable dispersive filter (AOPDF) that was used as a fast delay line to sweep τ, and therefore Ω at unprecedented speed.

5.1 Working principle

The AOPDF device used in this study is a Dazzler (FASTLITE, France), which has demonstrated tunable dispersion control and is commonly used for pulse stretching and compression of optical pulses [62, 63]. Two different models have been studied, the Dazzler-HR ("High resolution") and the Dazzler-WB ("Wide Band"), corresponding to two different crystal cuts [64]. The different properties of the two AOPDFs are summarized in Table 5.1.

5.1.1 Propagating wave in a dielectric medium

We first model the acousto-optic interaction in a simplified case, following the work of Verluise and collaborators [65]. We consider an electromagnetic wave propagating inside a birefringent crystal along the optical axis z. The electromagnetic wave experiences two different dielectric coefficients, depending on its polarization state along the x and y axis. These axes are directed by the unit vectors $\mathbf{e_1}$ and $\mathbf{e_2}$, and the light polarized along each direction experiences a dielectric coefficient of ϵ_1 and ϵ_2, respectively. The two coefficients correspond to two optical indices n_1 and n_2. In addition to polarization decomposition, the optical wave propagating along the optical axis can be decomposed in its spectral components:

$$\mathbf{E}(t,z) = \int \mathbf{E}(\omega,z)\exp(i\omega t)\mathrm{d}\omega \tag{5.4}$$

The electric field satisfies the wave equation :

$$\frac{\partial^2 \mathbf{E}}{\partial z^2}(\omega, z) + \omega^2 \mu_0 \epsilon \mathbf{E}(\omega, z) = 0 \tag{5.5}$$

In the absence of perturbation, the dielectric tensor expressed in the $(\mathbf{e_1}, \mathbf{e_2})$ basis writes:

$$\epsilon = \begin{pmatrix} \epsilon_1 & 0 \\ 0 & \epsilon_2 \end{pmatrix} \tag{5.6}$$

In this case, there are two decoupled equations corresponding to the two polarization modes. The general (forward propagating) solution of Equation 5.5 is:

$$\mathbf{E}(\omega, z) = S_1(\omega)\mathbf{e_1} \exp(-ik_1(\omega)z) + S_2(\omega)\mathbf{e_2} \exp(-ik_2(\omega)z) \tag{5.7}$$

Where $k_1(\omega)$ and $k_2(\omega)$ are given by the dispersion relation:

$$k_i(\omega) = \sqrt{\mu_0 \epsilon_i}\omega^2 = n_i(\omega)\frac{\omega}{c} \tag{5.8}$$

If we assume that the wave is linearly polarized along $\mathbf{e_1}$ ($S_2(\omega) = 0$), then it will propagate and keep its polarization along this axis. The phase acquired by each spectral component ω on a propagation length l_1 will be $k_1(\omega)l_1$.

Additionally, if the component suddenly becomes polarized along the $\mathbf{e_2}$ (as detailed in the next section), and keeps propagating for a distance l_2, the total phase acquired by the component becomes:

$$\varphi(\omega) = k_1(\omega)l_1(\omega) + \psi(\omega) + k_2(\omega)l_2(\omega) \tag{5.9}$$

where $\psi(\omega)$ is the phase induced by the polarization rotation from $\mathbf{e_1}$ to $\mathbf{e_2}$. We will now show how such polarization rotation is induced through acousto-optic coupling.

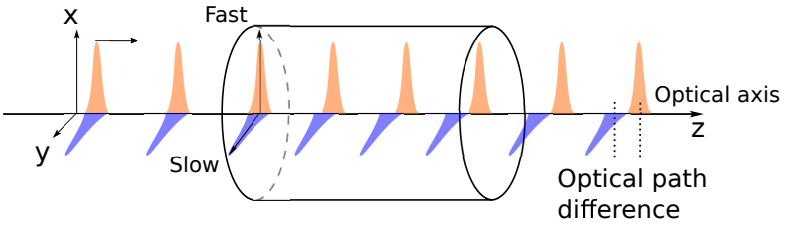

Figure 5.1 – Schematics of the birefringent crystal properties. Two optical fields polarized along the x and y axis represent the orange and blue pulses, respectively, as they propagate at different speeds inside the crystal. The x and y axes are the fast and slow axis of the crystal. At the output of the crystal, the group delay will appear as an optical path difference on the two pulses.

5.1.2 Acousto-optic coupling

A static dielectric perturbation of amplitude $a(z)$ is applied on the crystal, so that the dielectric tensor writes:

$$\epsilon(z) = \begin{pmatrix} \epsilon_1 & p_{12}a(z) \\ p_{21}a(z) & \epsilon_2 \end{pmatrix} \tag{5.10}$$

Following the same approach as Verluise and collaborators [65], the perturbation $a(z)$ is assumed to be a frequency-modulated signal and can be written through its envelope $\xi(z)$ and instantaneous spatial phase $\psi(z)$:

$$a(z) = \xi(z)(\exp(i\psi(z)) + \exp(-i\psi(z))) \tag{5.11}$$

The instantaneous spatial phase can additionally be linked to the instantaneous spatial frequency $K(z)$:

$$\psi(z) = \int_0^z K(z)\mathrm{d}z \tag{5.12}$$

The wave Equation 5.5 in such crystal then becomes:

$$\frac{\partial^2 \mathbf{E}}{\partial z^2}(\omega, z) + \omega^2 \mu_0 \epsilon(z)\mathbf{E}(\omega, z) = 0 \tag{5.13}$$

The general solution of Equation 5.13 is:

$$\mathbf{E}(\omega, z) = S(\omega)[A_1(z)\mathbf{e_1}\exp(-ik_1(\omega)z) + A_2(z)\mathbf{e_2}\exp(-ik_2(\omega)z)] \tag{5.14}$$

Inserting the general solution in Equation 5.13 and using the expression of the tensor ϵ in Equation 5.10 gives a system of two coupled equations:

$$\frac{\mathrm{d}^2 A_1}{\mathrm{d}z^2} - 2ik_1(\omega)\frac{\mathrm{d}A_1}{\mathrm{d}z} + \omega^2\mu_0 p_{12} A_2(z)a(z)\exp(i(k_1(\omega) - k_2(\omega))z) = 0 \tag{5.15}$$

$$\frac{\mathrm{d}^2 A_2}{\mathrm{d}z^2} - 2ik_2(\omega)\frac{\mathrm{d}A_2}{\mathrm{d}z} + \omega^2\mu_0 p_{21} A_1(z)a(z)\exp(i(k_2(\omega) - k_1(\omega))z) = 0 \tag{5.16}$$

The function $A_1(z)$ and $A_2(z)$ are expected to vary slowly, on lengths longer than the optical wavelengths $2\pi/k_1$ and $2\pi/k_2$. Assuming this, the second order derivative is neglected in equations (5.15) and (5.16), which can be written:

$$\frac{\mathrm{d}A_1}{\mathrm{d}z} = -\frac{i\omega^2\mu_0 p_{12}}{2k_1(\omega)} A_2(z)\xi(z)[\exp(-i\phi_+(z)) + \exp(-i\phi_-(z))] \tag{5.17}$$

$$\frac{\mathrm{d}A_2}{\mathrm{d}z} = -\frac{i\omega^2\mu_0 p_{21}}{2k_2(\omega)} A_1(z)\xi(z)[\exp(i\phi_+(z)) + \exp(i\phi_-(z))] \tag{5.18}$$

where:

$$\phi_\pm(z) = (k_2(\omega) - k_1(\omega))z \pm \psi(z) \tag{5.19}$$

If no particular condition is met, the phases ϕ_+ and ϕ_- are changing on a short length-scale, which leads to the exponential terms in Equations 5.17 and 5.18 oscillating rapidly as z increases. On the contrary, A_1, A_2, and ξ have slow variations with z. As a result, the derivatives of A_1 and A_2 described in Equation 5.17 and 5.18 will average out. However, the coupling will be efficient, if either ϕ_+ or ϕ_- remains constant over a certain distance. This condition is the *phase matching condition* between optical and acoustic waves:

$$\frac{\mathrm{d}\phi_\pm}{\mathrm{d}z}(z) = k_2(\omega) - k_1(\omega) \pm K(z) = 0 \tag{5.20}$$

In the following we consider that $k_2(\omega) > k_1(\omega)$. As a result, only ϕ_- will realize phase matching and participate in coupling A_1 and A_2. This coupling will take place when:

$$K(z) = k_2(\omega) - k_1(\omega) = \frac{\omega}{c}(n_2(\omega) - n_1(\omega)) \tag{5.21}$$

If $K(z)$ is further assumed to be monotone, there will be a single position $z(\omega)$ to Equation 5.21. This will correspond to the position in which the instantaneous frequency of the optical index perturbation is phase-matched to diffract the wavelength ω from polarization $\mathbf{e_1}$ to $\mathbf{e_2}$.

For simplification, we consider that the phase-matching conditions are met only for a small region of size δz of the crystal around $z(\omega)$. As a result, A_2 will experience a step at position $z(\omega)$ of value:

$$\begin{aligned}\delta A_2 &= \int_{z(\omega)}^{z(\omega)+\delta z} \frac{\mathrm{d}A_2}{\mathrm{d}z}\mathrm{d}z \\ &= -\frac{i\omega^2\mu_0 p_{21}}{2k_2(\omega)} A_1(z(\omega))\xi(z(\omega))\exp(i\phi_-(z(\omega)))]\delta z\end{aligned}$$

In particular, A_2 acquires a phase $-\phi_-(z(\omega))$ during the interaction. Assuming an optical wave is initially polarized along $\mathbf{e_1}$, the initial distribution of amplitude is $A_1(0) = 1$, $A_2(0) = 0$. From $z = 0$ to $z = z(\omega)$ the wave propagating along the $\mathbf{e_2}$ polarization state has a zero amplitude but has acquired the phase $k_2(\omega)z(\omega)$. During this interaction, the amplitude becomes non-zero, and the phase increases by $-\phi_-(z(\omega))$. From $z = z(\omega)$ to $z = L$, the propagation continues with no amplitude change and a phase increasing by $k_2(\omega)(L - z(\omega))$. The total phase acquired by the optical wave at frequency ω during propagation in the perturbed medium is:

$$\begin{aligned}\varphi(\omega) &= k_2(\omega)z(\omega) - \phi_-(z(\omega)) + k_2(\omega)(L - z(\omega)) \\ &= k_1(\omega)z(\omega) + \psi[z(\omega)] + k_2(\omega)(L - z(\omega))\end{aligned} \tag{5.22}$$

From the expression of the phase in Equation 5.22, we can identify the three

terms expressed in Equation 5.22. They correspond respectively to the propagation of the optical wave along the polarization state $\mathbf{e_1}$ (with optical index $n_1(\omega)$), the phase introduced by the interaction with optical index perturbation, and the propagation along the polarization state $\mathbf{e_2}$ with optical index $n_2(\omega)$.

To makes this interpretation even clearer, we can calculate the group delay encountered by each optical frequency, $\tau(\omega)$:

$$\tau(\omega) = \frac{\mathrm{d}\varphi}{\mathrm{d}\omega} \tag{5.23}$$

$$= \frac{\mathrm{d}z}{\mathrm{d}\omega}(k_1(\omega) - k_2(\omega) - K(\omega)) + \frac{\mathrm{d}k_1(\omega)}{\mathrm{d}\omega}z(\omega) + \frac{\mathrm{d}k_2(\omega)}{\mathrm{d}\omega}(L - z(\omega)) \tag{5.24}$$

$$= \frac{z(\omega)}{V_{g1}(\omega)} + \frac{L - z(\omega)}{V_{g2}(\omega)} \tag{5.25}$$

Where V_{g1} and V_{g2} are the group velocity of the optical frequencies along polarization $\mathbf{e_1}$ and $\mathbf{e_2}$, respectively. We can clearly see the interpretation of this group delay as propagation along in polarization state $\mathbf{e_1}$, followed by propagation along the polarization state $\mathbf{e_2}$. Consequently, the group delay of each frequency can be addressed independently by adjusting the instantaneous spatial frequency $K(z)$ of the dielectric tensor perturbation $a(z)$. Additionally, the amplitude of each diffracted optical component can be separately addressed by choosing the appropriate amplitude of this perturbation $\xi(z)$.

5.1.3 Adding dispersion with the AOPDF

From Equation 5.25, it appears that the arrival time of each frequency can be independently tuned by engineered a perturbation $a(z)$, such that the different frequencies are diffracted at different positions $z(\omega)$ in the crystal.

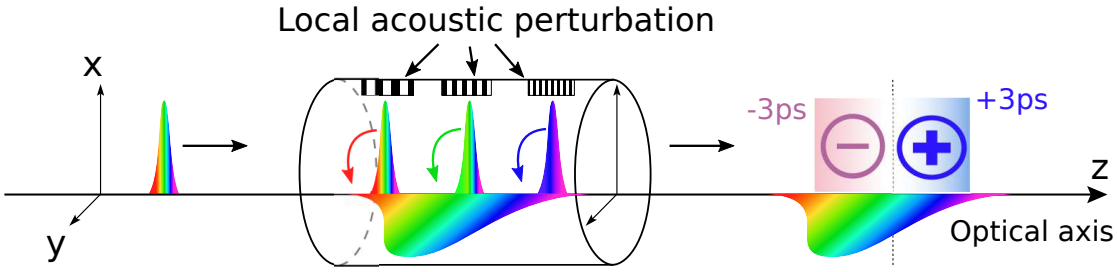

Figure 5.2 – An acoustic perturbation inside the crystal can diffract the optical pulse from the x to the y polarization state. Different acoustic frequencies diffract specific optical frequencies, allowing to independently tune the effective optical path experienced by each optical frequency, within the range allowed by the crystal.

We will make the assumption that the group velocities V_{g1} and V_{g2} are indepen-

dent of frequency. Considering our optical pulses will have limited spectral content, this assumption remains valid for our experiments. Under this assumption, the group delay encountered by each optical frequency can be independently tuned from $\frac{L}{V_{g1}}$ to $\frac{L}{V_{g2}}$. The difference between the minimum and maximum group delay gives the AOPDF a working window, which is $3\,\mathrm{ps}$ to $7\,\mathrm{ps}$ for the devices we experimented with during this thesis (Table 5.1).

Adding dispersion with an AOPDF is straightforward and corresponds to a linear group delay:

$$\tau(\omega) = D\omega + \tau_0 \tag{5.26}$$

where D is group-delay dispersion (GDD) in fs and τ_0 a delay time

Such relations can be achieved by choosing a linear function for $z(\omega)$:

$$z(\omega) = D[\frac{L}{V_{g1}} - \frac{L}{V_{g2}}]^{-1}\omega + z_0 \tag{5.27}$$

The only constraint for the quantity of dispersion the AOPDF can imprint on the optical pulse is that the delay between the highest frequencies and lowest frequencies have to remain within the AOPDF working window.

5.1.4 Adding delay with the AOPDF

Previous to this discussion, we have assumed that the perturbation $a(z)$ was static. Considering that the propagation of light in the crystal is 10^5 times faster than that of elastic deformations, this assumption holds true for each optical pulse that passes through the crystal. However, the perturbation induced in the crystal is a propagating acoustic wave, with a velocity of $V_{ac} = 680\,\mathrm{m\,s^{-1}}$. Therefore, the acoustic perturbation is actually moving along the z axis. Assuming the crystal is not dispersive for acoustic waves, the perturbation along the z axis becomes $a(z + V_{ac}t)$.

The result of this acoustic propagation is relatively straightforward: the position $z(\omega)$ in the crystal that efficiently diffracts optical frequency ω becomes a linearly increasing function of time:

$$z(\omega, t) = z(\omega, t = 0) + V_{ac}t \tag{5.28}$$

The group delay is also impacted, and increases linearly with time:

$$\tau(\omega, t) = \tau(\omega, t = 0) + \alpha t \tag{5.29}$$

where α is the dimensionless ratio defined by:

$$\alpha = V_{ac}[\frac{L}{V_{g1}} - \frac{L}{V_{g2}}]^{-1} \tag{5.30}$$

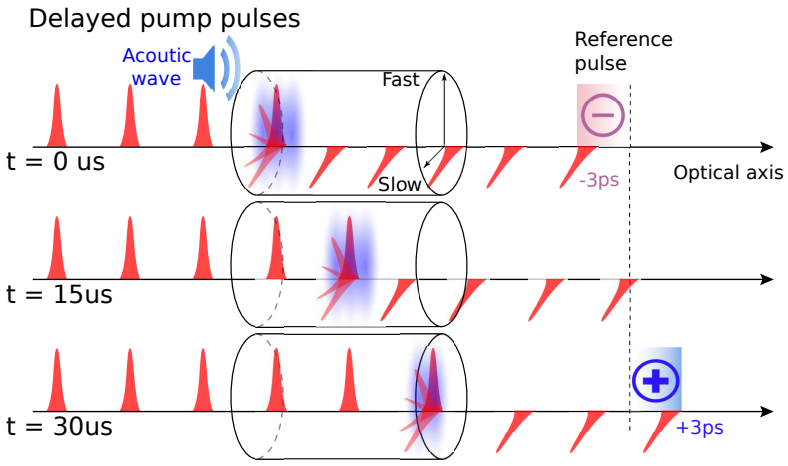

Figure 5.3 – A acoustic wave propagating inside the crystal induces a group delay that changes linearly over time.

The conversion factor α defines the way the propagation of the acoustic wave affects the optical propagation. The value of alpha was measured (Section 5.2.2) to be $\alpha = 260\text{fs}/\mu\text{s} = 2.6 \times 10^{-7}$ for the HR-Dazzler and $\alpha = 161\text{fs}/\mu\text{s} = 1.6 \times 10^{-7}$ for the WB-Dazzler. When propagating during one microsecond, the acoustic wave introduces an additional group delay all optical frequencies of 260 fs for the HR crystal and 161 fs for the WB crystal. This ratio will be particularly important since it controls the speed at which the optical delays are swept.

5.1.5 Quasi-collinear interactions

Previous sections describe collinear interactions between the acoustic and electromagnetic field. In practice, for the devices considered in this work, these interactions are quasi-collinear and the equations differ slightly from the one described previously. One can still use the simplified picture of an optical frequency interacting at a specific point in the crystal, and then diffracted in the other polarization state. The phase matching condition also has to be met in this case, and Equation 5.20 becomes:

$$\vec{K}(z) = \vec{k}_2(\omega) - \vec{k}_1(\omega) \tag{5.31}$$

The AOPDF consists of a 25-mm-long TeO_2 crystal. Both the acoustic wave and the optical wave propagate in the plane containing the [110] and [001] axis. The incident optical wave is polarized along the $[1\bar{1}0]$(x) axis, which corresponds to the vertical axis in the experimental setup. The optical wave has a wave vector k_o, making an angle θ_o with the [110] axis. The acoustic wave is a transverse wave, polarized along the x axis. Its wave vector K makes an angle θ_a with the [110] axis. Because the crystal has a strong elastic anisotropy, the Poyting vector

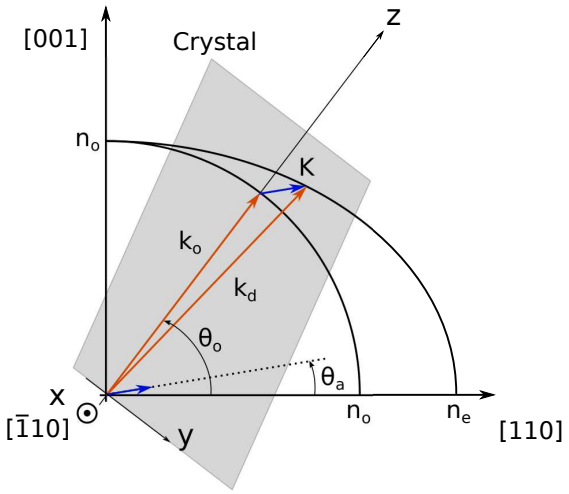

Figure 5.4 – Schematics of the crystal cut and refractive index ellipse diagram. The incident optical wave and the acoustic wave propagate along the z axis. The acoustic wave vector $\vec{K}$ is not aligned along z due to the elastic properties of the crystal. The diffracted beam propagates at a slower speed ($n_e > n_o$) and at a slight angle with the z axis.

of the acoustic wave (and therefore its propagation direction) is not aligned with K. Instead, the device is designed such that the acoustic wave propagates collinearly with the optical wave, along k_o.

If the phase-matching conditions are met (Equation 5.31), the optical wave can be diffracted into the propagation mode with the subsequent wavevector $\vec{k_d} = \vec{k_o} + \vec{K}$ and horizontal polarization (along the y axis). The diffracted beam is not perfectly collinear with the incoming one, which allows for spatial separation of the two. Additional optical components are diffracted parallel to each other but not exactly overlapping. The spatial effect resulting from this quasi-collinearity has not been detected experimentally during this work.

5.1.6 Delay line literature review

The AOPDF is widely used in ultra short pulse engineering due to its tunable dispersive properties. One case in which it is typically used is dispersion and compression of high power, low repetition rate lasers. Acoustic waves can be updated to a maximal rate of 33 kHz for the HR crystal (40 kHz for the WB crystal) , which allows pulse-to-pulse phase control of lasers with this repetition rate (or a lower one).

Schubert and collaborators illustrated the AOPDF as a precise delay line in 2013 [66]. This technology was used experimentally for the first time in 2014 by Znakovskaya and collaborators, who performed Fourier-transformation spectroscopy on pressured acetylene gas [67].

Our group published the first use of the AOPDF in the context of pump-probe transient absorption spectroscopy, and demonstrated the delay line's compatibility with an imaging modality [68]. Two additional studies have used the AOPDF for rapid delay sweeping during the span of the work presented here. Urbanek and coworkers have illustrated its application to terahertz spectroscopy and surface profiling. Alshaykh, Liao, and colleagues used the AOPDF as a fast delay line in stimulated Raman scattering featuring spectral focusing. Their work is similar to the results shown in Chapter 6 of this manuscript, however the work present in this manuscript extends much further the development of ultra-fast SRS imaging using AOPDF.

5.2 Experimental assessment

5.2.1 Transmission efficiency

The acoustic wave propagates inside the crystal and diffracts the optical pulse at different points along its propagation. The diffraction efficiency needs to remain constant while the acoustic wave propagates for the AOPDF to act strictly as a delay line. The following section focuses on the HR-AOPDF, but the same analysis has been performed on the WB crystal.

The pump laser (specifications in Section 6.1) was sent to the input of the AOPDF, and the light intensity in the diffracted beam was measured with a photodiode (Thorlabs PDA100A2, 11MHz Bandwidth). The bandwidth of the photodiode was large enough to enable the visualization of the laser intensity fluctuations in the time required for an acoustic pulse to propagate through the whole crystal (Table 5.1).

The acoustic pulse in the AOPDF was set to compensate the dispersive optical properties of the crystal, resulting in a $4\,\mu s$-long acoustic pulse. The duration of the acoustic pulse introduces two dwell times. The first one occurs when the acoustic wave is generated at one end of the crystal, and the second one occurs when it vanishes at the other end.

Therefore, the duration of the acoustic pulse is critical, as it will limit the amount of time the acoustic wave is fully formed and propagates inside the crystal. The generation, and vanishing of, the acoustic wave leads to the rise and fall of the intensity of the diffracted beam (Figure 5.5). While the acoustic wave is propagating inside the crystal, the diffracted beam maintains a constant intensity, within 10% of the maximum value. This result highlights the limited distortion added by the AOPDF. Additionally, this distortion could be compensated for numerically using the measured diffraction efficiency.

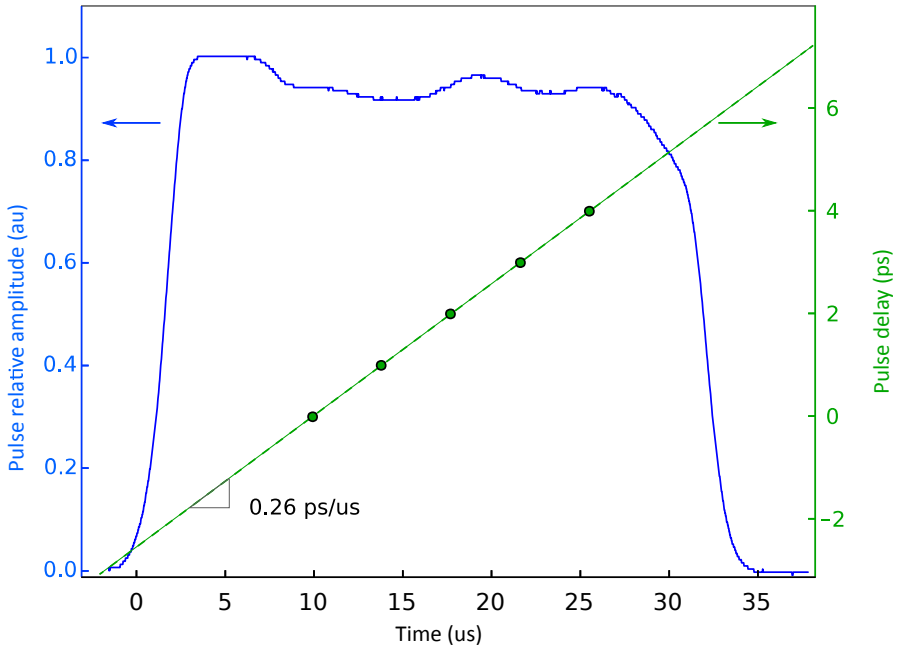

Figure 5.5 – Characterization of the transmission properties of the AOPDF (Dazzler HR) as the acoustic wave propagates within. The solid blue line (left scale) is obtained by measuring the pump pulse directly. The green dots (right scale) are calibrated using a mechanical delay line. The dotted green line shows the linear fit of the data.

Model	Pulse propagation time μs	Max delay range ps	Scaling ratio $\alpha(fs/\mu s)$
HR	33	7	260
WB	25	3	161

Table 5.1 – Characteristics of the two AOPDF types.

5.2.2 Delay linearity

The AOPDF adds a linearly increasing delay to the input pulses (Section 5.1.4). Using this property, we demonstrated fast pump-probe transient absorption spectroscopy on pigments [68]. The linearity of the delay was measured using transient absorption signals. This signal comes in the form of a sudden rise in voltage at the output of the lock-in amplifier, followed by exponentially decaying voltage levels. The voltage rise corresponds to the simultaneous arrival of a pump and a probe pulse to a sample. The exponential tail indicates that the pump laser has arrived prior to the probe pulse.

In the transient absorption scheme presented in our work, the pump beam was passed through the AOPDF and focused on an ink sample, along with the probe pulse. Using a mechanical delay line, a known delay is added to the pump laser, resulting in a shift in the signal trace (Figure 5.6). The temporal shift is measured in terms of acoustic propagation time for several optical delays ranging from 0 to $7\,\mathrm{ps}$. This measurement confirms that, for each microsecond that the acoustic wave propagates, the optical pulses are delayed by an additional $260\,\mathrm{fs}$. The ratio between the real time and the equivalent group delay gives the value of α in Equation 5.29. The measured value of $\alpha = 2.6 \times 10^{-7}$ is consistent with previous work [66], as well as the AOPDF specifications.

The linearity of the delay in the AOPDF is interesting in that it removes the need for post treatment required in other delay lines. Competing technology for fast delay scanning revolves around resonant mirrors that introduce a sinusoidal delay, which introduce additional signal distortion that needs to be compensated for [24].

5.2.3 Intensity noise

As mentioned in Chapter 3, active devices can add intensity fluctuations on the laser beam, contributing to suboptimal signal to noise ratios in measurements. We quantified the amount of noise introduced by the AOPDF.

The pump laser was sent trough the AOPDF and the diffracted beam was measured using a fast photodiode (DET10A, Thorlabs, 1ns rise time). The AOPDF introduces an intense laser intensity modulation at its repetition rate and harmonics, making laser fluctuation measurements at higher frequencies difficult. To dampen these low frequency modulations, the output current of the photodiode was measured through a $50\,\Omega$ resistor, and filtered with a high-pass filter ($-3\,\mathrm{dB}$

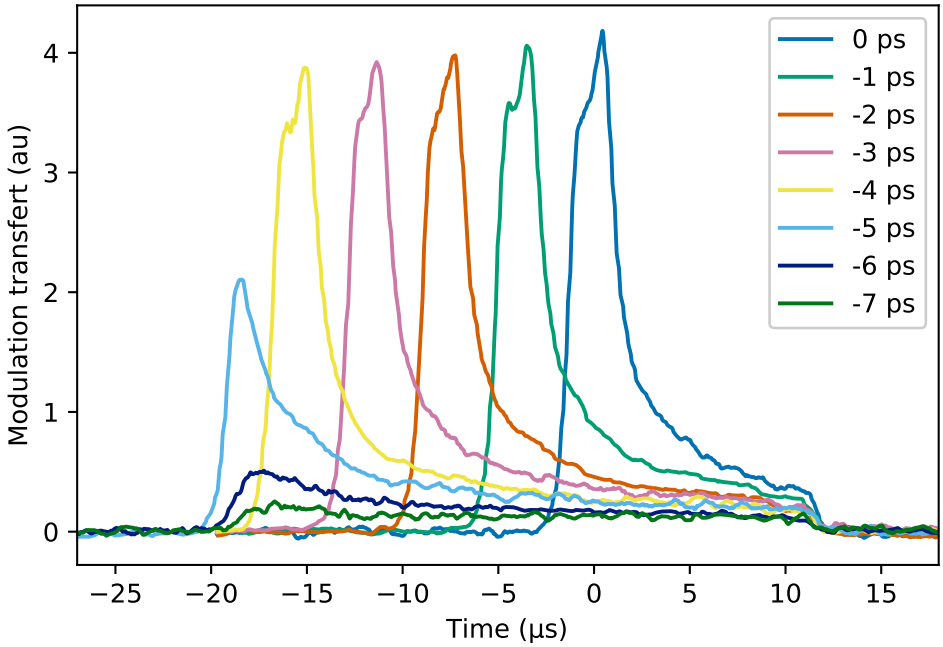

Figure 5.6 – Pump probe traces obtained on an ink sample for different values of delay added by the mechanical delay line. The acoustic wave propagates inside the AOPDF between −21 and −12 µs. The linearity of the delay line is observed within this time, with 15 µs of acoustic propagation corresponding to a 4 ps delay of the optical pulses.

at $5.6\,\mathrm{MHz}$, EF515 Thorlabs, 6^{th}order). The filtered voltage power spectral density was acquired between 10 and $40\,\mathrm{MHz}$ by means of a spectrum analyzer (HF2LI, Zurich Instrument). The laser power was set so that the average current from the photodiode reached $5\,\mathrm{mA}$. This value was previously used in laser noise characterization, and is below the photodiode saturation level (Chapter 3).

The expected power spectral density for this laser power can be calculated with Equation 3.15 to be:

$$PSD_{shotnoise} = 2qRI_{avg} = 8 \times 10^{-20}\mathrm{W/Hz} = -191\mathrm{dBW/Hz} \tag{5.32}$$

This value is below the spectrum analyzer input noise (-182 dBW/Hz, Figure 5.7 grey curve) and cannot be measured without an amplification stage such as the one described in Chapter 3. The AOPDF introduce a significant laser intensity modulation that can be measured even without prior amplification (Figure 5.7). The HR AOPDF introduces a significant noise around $12\,\mathrm{MHz}$ of amplitude -155 dBW/Hz (Figure 5.7 blue curve). Relative to the power of the DC component (-29dBW for $5\,\mathrm{mA}$ in a $50\,\Omega$ resistor), this leads to a relative modulation of $-155 + 29 = -126$ dBc/Hz. The first WB AOPDF that was measured showed an even higher noise feature, with -145 dBW/Hz (-116 dBc/Hz) around $25\,\mathrm{MHz}$.

The strong noise described on these two devices has been attributed to unwanted interference from reflections of the acoustic wave inside the crystal. For the WB crystal working with a $800\,\mathrm{nm}$, the carrier frequency of the acoustic wave is centered around $52.4\,\mathrm{MHz}$. A newly generated acoustic wave can interfere with the reflection of a previously generated one, creating a standing wave inside the crystal with double the frequency of the carrier, in this case $104.8\,\mathrm{MHz}$. This high frequency standing wave induces a fluctuating diffraction efficiency of the AOPDF, which then is probed at the $80\,\mathrm{MHz}$ by the pump laser. The frequency difference between the standing wave and the laser repetition rate creates an aliasing effect, resulting in the pump laser being modulated at the frequency difference $104.8 - 80 = 24.8\mathrm{MHz}$. Similar calculations can be made for the HR AOPDF, for which the carrier frequency at $800\,\mathrm{nm}$ is centered around $85.9\,\mathrm{MHz}$. In this case, the expected laser modulation is centered around $12\,\mathrm{MHz}$. In both the HR and WB crystals, the expected modulation frequency matches the experimental data (Figure 5.7).

The SRS scheme presented in Chapter 6 performs lock-in detection at $20\,\mathrm{MHz}$ on the pump laser. Consequently, it is critical to minimize any laser fluctuations around this frequency, and any additional modulation from the AOPDF will result in measurements with higher noise levels. To minimize the effect of acoustic reflections on laser intensity modulation, a low noise WB AOPDF was engineered by the Fastlite company. An additional slanted crystal of TeO_2 was attached to one side of the crystal, reflecting the acoustic wave out of the horizontal plan. This second WB AOPDF was measured by the manufacturer to improve the noise figure by $10\,\mathrm{dB}$. This noise dampening was confirmed experimentally (Figure 5.7,

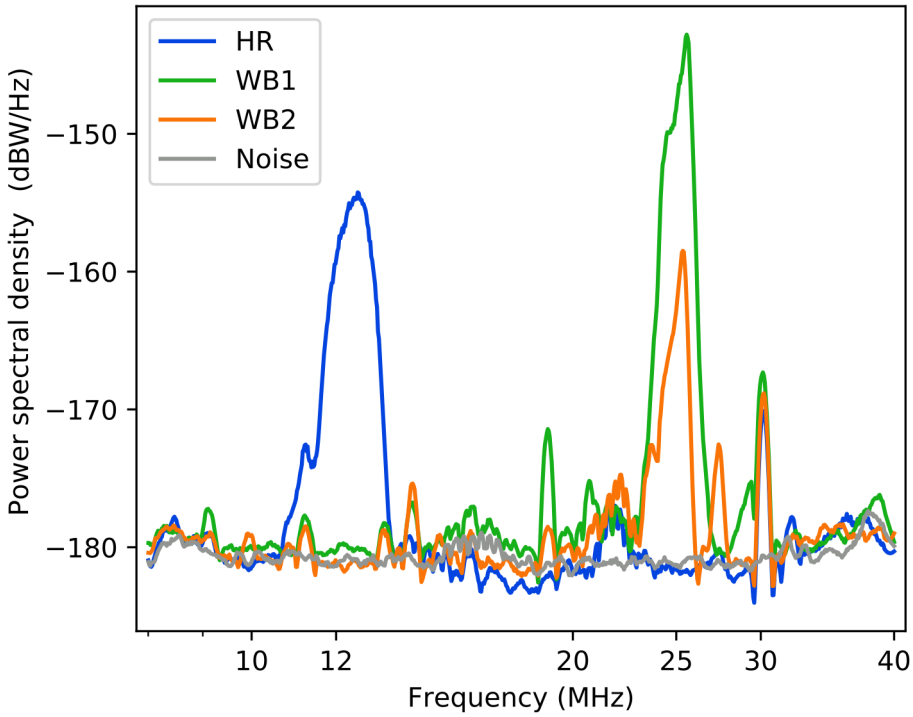

Figure 5.7 – Power spectral density of the photodiode output for the HR crystal (blue), the WB crystal without noise attenuation (WB1, green), and the WB crystal with noise attenuation (WB2, orange). The electronic noise level is -180dBW/Hz (grey).

orange curve). However, the modulation introduced by the AOPDF remains significant, with a relative amplitude of -131 dBc/Hz.

5.2.4 Impact on SRS measurements

We are interested in the amount of noise introduced by the AOPDF in the final measurement. This noise presents in the form of a modulated voltage output of the lock-in amplifier system. We sent the laser beam diffracted by the AOPDF onto our photo-diode that was used for acquisition, and the output was connected to the associated lock-in amplifier (APE SRS Lock-in module).

The trigger signal from the laser ($80\,\mathrm{MHz}$ TTL) was transformed via a f/4 frequency divider into a $20\,\mathrm{MHz}$ signal which was fed as a reference for the lock-in amplifier. The bandwidth of the lock-in amplifier was set to $1.6\,\mathrm{MHz}$, the largest setting on the lock-in module, which corresponds to an integration time of $100\,\mathrm{ns}$. The gain was set to $43\,\mathrm{dB(V)}$ ($86\,\mathrm{dB(W)}$), the largest gain setting available without post-amplification.

The effect of the lock-in amplifier is to send the $20\,\mathrm{MHz}$ frequencies of the photodiode power spectral density to the DC component of the lock-in output power spectral density. The frequencies above and below $20\,\mathrm{MHz}$ are folded back onto positive frequencies, and noisy components at frequency f_{noise} in the photodiode current will appear in the lock-in output voltage at frequency $|f_{noise} - 20\mathrm{MHz}|$.

The noise observed previously at the output of the photodiode (at $12\,\mathrm{MHz}$ and $24.8\,\mathrm{MHz}$ for the HF and WB crystals, respectively), can be observed at the output of the lock-in amplifier centered around $7.5\,\mathrm{MHz}$ and $5\,\mathrm{MHz}$ (Figure 5.8). For the HR and the first WB crystals, the average laser power on the photodiode was set to $30\,\mathrm{mW}$. This optical power corresponds to an average photocurrent of $15\,\mathrm{mA}$. The shot noise associated with this optical power is given by Equation 3.15, and after a $86\,\mathrm{dB}$ amplification the power spectral density associated with shot noise is $-117\,\mathrm{dBW/Hz}$. At low frequencies, and up to the cutoff frequency of the lock-in, the experimental PSD confirms that the system is working at the shot noise limit, suggesting that the AOPDF does not add extra noise in the measurement at these frequencies (Figure 5.8).

Although the short-pass filter of the lock-in module has a bandwidth of $1.6\,\mathrm{MHz}$, the cutoff is not sharp enough to remove the noise at $7.5\,\mathrm{MHz}$ and $5\,\mathrm{MHz}$ introduced by the AOPDFs. By adding a second short-pass filter ($-3\,\mathrm{dB}$ at $1.35\,\mathrm{MHz}$, EF508 Thorlabs, 5^{th}order), the noise features were dampened to negligible values (Figure 5.8, pink curve). No noticeable distortions of the signal were observed due to the presence of the filter, but a deeper analysis should be performed to validate this empirical statement.

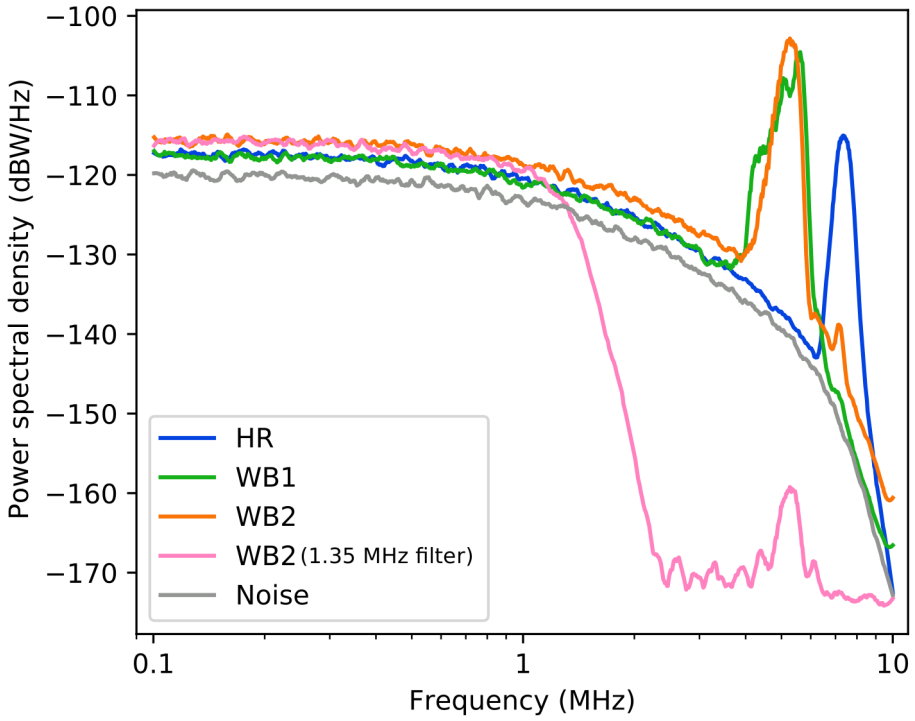

Figure 5.8 – Power spectral density of the lock-in amplifier output for the HR crystal (blue), the WB crystal without noise attenuation (WB1, green), the WB crystal with noise attenuation (WB2, orange) and with additional electronic filtering (pink). The electronic noise level is shown in grey.

5.3 Comparison with a mechanical delay line

As demonstrated early in this section, the AOPF ideally acts as a very linear delay line, and has near constant transmission. However, the signal acquired when using the AOPDF can differ from the mechanical delay line reference through several processes.

The range of delays accessible with the AOPDF is limited by the device (Table 5.1). The duration of the acoustic wave further limits this range, by modifying the transmission properties of the delay line at both of its ends. The lock-in amplifier demodulates the signal within the duration of an acoustic pulse, with a certain integration time τ. Any changes in the signal amplitude on timescales faster than τ will be distorted. This has been observed as a slight resolution drop and discussed previously in Chapter 4. Additionally, the low-pass filtering process that is required for noise rejection after the lock-in amplifier can further distort the signal.

A comparison between the AOPDF and a mechanical delay line was published in the context of pump-probe microspectroscopy and showed no difference between the two [68]. A similar comparison in the context of SRS will be provided in the following chapter.

6 Hyper-spectral SRS

In this Chapter, all the technical aspects described previously (spectral focusing SRS, noise optimization, fast AOPDF delay line) are combined to perform SRS spectroscopy and imaging in different application fields. Spectral focusing SRS images acquired with the fast AOPDF delay line are compared with images acquired with the mechanical delay line.

6.1 Setup description

The optical setup utilized in our present work combines the different techniques and tools introduced in the previous Chapters.

6.1.1 Laser sources

The main laser source is a Chameleon OPO-VIS (Coherent), which consists of a Titanium Sapphire (TiSaph) laser providing $160\,\mathrm{fs}$ pulses at $80\,\mathrm{MHz}$. A fraction of the beam is sent directly to the optical setup, while the rest is used to pump an optical parametric oscillator (OPO). The signal from this OPO serves as the second beam in SRS. Unless otherwise specified, the TiSaph laser is tuned to $800\,\mathrm{nm}$ and serves as the pump beam in SRS. The OPO is tuned around $1045\,\mathrm{nm}$ to provide the Stokes beam in our SRS scheme. The frequency difference between the pump and Stokes beam allows us to target the CH-stretch region in the vibrational spectrum, around $2930\,\mathrm{cm}^{-1}$, with a $110\,\mathrm{cm}^{-1}$ spectral window. In order to properly center the range of wavenumbers accessible with this scheme, the OPO wavelength was tuned between 1043 and $1053\,\mathrm{nm}$, depending on the application. This range of wavelength corresponds to centering the SRS spectral window around 2913 to $3000\,\mathrm{cm}^{-1}$ (Table 6.1).

OPO center wavelength (nm)	1043	1045	1047	1053
Spectral window center (cm^{-1})	2913	2930	2950	3000

Table 6.1 – SRS spectral window centering for different Stokes (OPO) wavelengths. The pump beam is fixed at $800\,\mathrm{nm}$ and the width of the spectral window is $110\,\mathrm{cm}^{-1}$

6.1.2 OPO preprocessing

The OPO beam is modulated using an acousto-optic modulator (AOM) (MT200-A0.2-1064, AA Opto-Electronic, France). The beam is focused inside the AOM using a $10\,\mathrm{cm}$ lens and collected with a $15\,\mathrm{cm}$ one, allowing for a 1.5x beam expansion. The modulation frequency is obtained by using a frequency divider (SRS Lockin Module, APE, Germany) to divide the laser repetition frequency by four. The result is a modulation frequency of $20\,\mathrm{MHz}$, which is synchronized with the pulses.

The modulated beam is then sent through two parallel diffraction gratings in a double pass scheme (see Chapter 4 for more details). This allows one to adjust the second order phase imprinted on the beam. Tunable attenuation of the beam is then performed with a half wave plate and polarization beam splitter, keeping the beam horizontally polarized.

6.1.3 TiSaph preprocessing

The TiSaph beam can be sent in two paths, depending on the application. The first path is a double pass through parallel diffraction gratings to control the second order phase, similar to the one on the OPO path. It is used in combination with the mechanical delay line to obtain SRS spectra in the spectral focusing scheme. The second path goes through the acousto-optic programmable dispersive filter (AOPDF) (see Chapter 5 for more details). For both cases, the beam is then expanded with a 3x telescope, attenuated in the same way the OPO is with polarization optics, and goes through a mechanical delay line (M 415.2S, Physik Instrumente, Germany) for fine tuning of the pulse timing.

6.1.4 Scanning Microscope

The OPO and TiSaph beams are then combined with a dichroic mirror, and fine adjustments are performed to ensure their collinearity. The combined beams are sent through scanning galvanometric mirrors (Cambridge Technology, USA). The mirrors are conjugated with the back focal plane of the microscope objective with a 3x telescope. The microscope body is a commercially available system (Eclipse Ti-U, Nikon, Japan) working in an inverted scheme. The beams are focused on the sample with a 40x/1.15NA water immersion objective (N40XLWD-NIR, Nikon), and collected using a 20x/0.75NA air objective (CFI Plan Apo Lambda 20X, Nikon).

6.1.5 Detection

The SRS signal is collected in the forward direction, and the back aperture of the collection objective is conjugated with the detector (SRS Lockin Module, APE,

Integration time (µs)	0.1	0.3	2	10	20
Bandwidth (kHz)	1600	5300	800	16	8

Table 6.2 – Lockin integration times and associated bandwidth.

Germany) with a 1/3x telescope. The modulated OPO beam is filtered using a low pass filter (FES0900, Thorlabs, USA). The modulation that is transfered to the TiSaph laser is measured with a lockin detection scheme (SRS Lockin Module, APE, Germany).

In the epi direction, a dichroic mirror (770dcxr, Chroma, USA) and two short-pass filters (FESH0750, Thorlabs, USA) allow for the detection of fluorescence, second harmonic generation, or CARS signalling. Only second harmonic generation was measured in this work. The SHG signal was isolated using a 400/40nm band-pass filter (HQ400/40, Chroma, USA), and detected with a photomultiplier tube (R9110 tube and C7950 data socket, Hamamatsu, Japan).

6.1.6 Lockin detection

The TiSaph beam intensity is measured with a biased photodetector (SRS Lockin Module, APE, Germany). The detector area is $1\,\mathrm{cm}^2$, with a bandwidth of $25\,\mathrm{MHz}$, and quantum efficiency of 80% at $800\,\mathrm{nm}$.

The output of the photodiode is sent as the input of the lockin amplifier. The same frequency divider that drives the AOM provides the reference signal from the lockin. The phase of the lockin is pi-shifted from the modulation on the OPO beam in order to detect stimulated Raman loss on the pump as a positive signal. The lockin integration time (i.e. bandwidth) can be selected from the values in Table 6.2. The gain of the amplifier was set between 35 and $48\,\mathrm{dBV}$.

6.1.7 Acquisition and triggering

The output of the lockin amplifier is acquired with a fast analog digital converter (ATS460-128M PCI Digitizer, 125 MS/s, AlazarTech, Canada). The sampling rate of this digitizer is set to over-sample the lock-in output.

The entirety of the experimental setup is controlled via a custom made Labview interface (Labview2011, National Instruments, USA). An Input/Output Card (NI 6361, National Instruments, USA) was used to control the galvanometric mirrors, to trigger the AOPDF, and to trigger the data acquisition on the AlazarTech digitizer. When using the AOPDF, careful synchronization had to be done to account for the delay of a few microseconds between the AOPDF trigger event and the formation of the acoustic wave inside the AOPDF crystal. The National Instrument card acquired the second harmonic generation signal provided by the photomultiplier tube.

6.1.8 Calibration samples

In spectrally focused SRS, the spectral window where acquisition is made possible is limited by the spectral width and central wavelengths of the pump and Stokes beams. In this window, the efficiency of the SRS process is not uniform, but a Gaussian. As a result, it is important to center the spectral window on the part of the CH stretch region that is most relevant. This is done by tuning the central wavelength of the OPO and by increasing sensitivity at low and high wavenumbers (Table 6.1).

Using spectral focusing, the accessible spectral window is equivalent to a delay window in which the pulses overlap. It is critical to know the correspondence between the pulse delay that is set and its resulting probed wavenumber. The first step is to characterize the delays for which the pulses overlap.

To probe the pulse overlap, we change the delay between the two pulses and use fluorescein crystals to record the modulation transfer from the OPO to the TiSaph laser. The strong two photon absorption from fluorescein gives a strong photon loss on the pump beam when the Stokes beam is present, independently of the wavelength. Therefore, the signature of two photon absorption is similar to that of a perfectly flat SRS spectrum. This signature corresponds to the cross-correlation function of the two optical pulses. This function gives the relative SRS efficiency across the different delays, and the different wavenumbers probed as a result (Figure 6.1). The delay to achieve maximal cross-correlation function corresponds to the point where the two pulses simultaneously arrive to the sample. This corresponds to the center of the spectral window.

One can already compute the delay to wavenumber conversion function by knowing both the delay that needs to be added to the TiSaph laser to synchronize it with the OPO beam and the chirping parameter of both optical pulses. In order to further calibrate the system, we used dimethyl sulfoxide (DMSO), which has two distinct Raman lines in the CH stretch region (at room temperature), at 2913 and $2994\,\mathrm{cm}^{-1}$ (Figure 6.4). This allows for mitigation of the small changes in pulse delays across various experiments.

6.1.9 AOPDF working window

The AOPDF can imprint a specific phase on a wide range of frequencies. This range needs to cover the full range of frequencies present in the incoming pulse. The spectral width of the TiSaph laser pulses are measured to be of $6.1\,\mathrm{nm}$ FWHM (Table 4.1). The effective spectral window of the AOPDF should be at least this wide in order to avoid clipping, and therefore distorting, the optical pulse. Conversely, if the AOPDF spectral window is too large, the acoustic wave will be designed to diffract optical wavelengths that are not present in the incoming pulse. There is, however, a limit to the amount of acoustic power that can be sent through the crystal without damaging it. As a result, the unnecessary acou-

stic frequencies will ultimately limit the maximum diffraction efficiency of the AOPDF by limiting the amount of useful power that can be sent through the crystal.

We used different sizes for the AOPDF spectral window, from 2 to 25 nm. The effect on the SRS spectral window was observed by measuring the cross correlation of the pump and Stokes pulses on fluorescein. For AOPDF spectral windows that were below the optical spectral width, distorted signals were observed. The SRS spectral window was broadened with increasing AOPDF spectral window, until the full range of optical frequencies present in the laser were included in this window.

The value of 15 nm was chosen as the smallest spectral window to diffract all optical frequencies. This value is consistent with the spectral width of the TiSaph laser as it corresponds to 2.5 times the spectral FWHM of this laser.

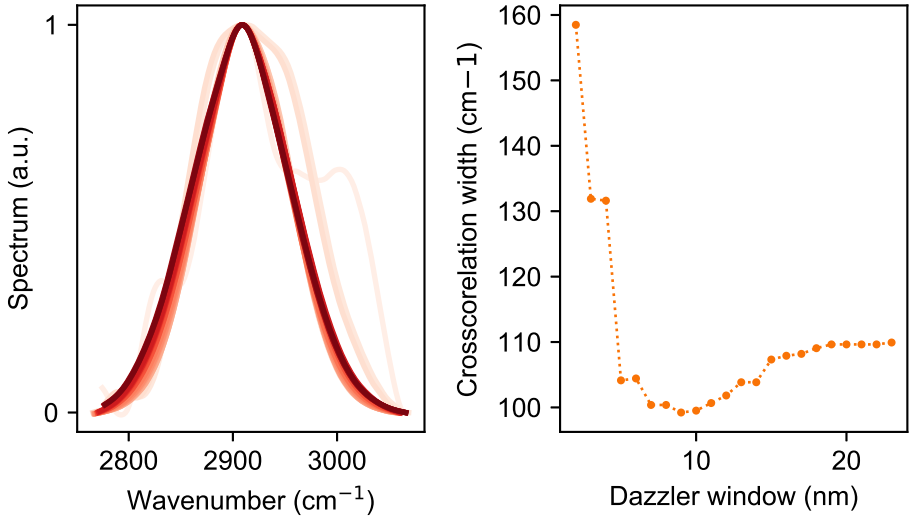

Figure 6.1 – AOPDF working window optimization. Left: SRS efficiency in the spectral domain, from fluorescein calibration. The lines are plotted from light to dark with increasing AOPDF window parameter. Right: Width of the spectral window with increasing AOPDF window parameter.

For the remainder of this work, no normalization procedure was applied to correct for the non-uniformity of the spectral window. This normalization would be required to quantitatively compare the spectra acquired through this method with other Raman spectra.

6.2 Spectral measurements

As detailed in Chapter 4, we can retrieve spectral resolution using spectral focusing with chirped optical pulses. In Chapter 4, we measured the spectral resolution as a function of dispersion added on the TiSaph beam with the grating pair, and concluded that we could reach $25\,\mathrm{cm}^{-1}$ resolution, not far from the $20\,\mathrm{cm}^{-1}$ limit anticipated from the theoretical analysis.

In the present Chapter, we are interested in combining the spectral focusing scheme with the AOPDF acting as a fast delay line. Several measurements need to be performed to ensure that the use of this device does not impair the signal acquisition: a) The AOPDF replaces the grating pair on the TiSaph beam; it is necessary to optimize the dispersion added by the device. b) The spectrum is acquired during the propagation of the acoustic wave, within tens of microseconds. The lockin bandwidth needs to be large enough to allow such fast signals to be acquired without distortion. c) The AOPDF delay line needs to be compared to the mechanical delay line in order to ensure that the two schemes are equivalent.

The resolution measurements are realized using DMSO, which has a sharp Raman line at $2913\,\mathrm{cm}^{-1}$ with a $5.4\,\mathrm{cm}^{-1}$ width. The OPO center frequency is set to $1043\,\mathrm{nm}$, which centers the spectral range on this Raman line and minimizes artifacts from the non uniform spectral efficiency. The linewidth of the Raman line is smaller than the resolution we obtain, and consequently does not significantly broaden the signal. The linewidth is still accounted for in the resolution presented in Figures 6.2.

6.2.1 AOPDF Dispersion

The second order phase added by the AOPDF is tuned from -110 to $-25\,\mathrm{kfs}^2$, while the spectrum of DMSO is recorded (Figure 6.2). The grating distance on the OPO beam is set to $4.3\,\mathrm{cm}$, corresponding to $-59\,\mathrm{kfs}^2$ of second order phase at the sample plane (i.e. in addition to correcting the optics in the setup). The resolution is expected to be optimal for $-74\,\mathrm{kfs}^2$ on the TiSaph beam: $-59\,\mathrm{kfs}^2$ for spectral focusing, $-13\,\mathrm{kfs}^2$ to compensate for the AOPDF internal dispersion (from device specifications), and $-2\,\mathrm{kfs}^2$ for the optics in the setup (Table 4.1). The resolution is experimentally optimal for $-78\,\mathrm{kfs}^2$, which is still consistent with the expected value. This discrepancy could be due to the microscope objective, which has not been taken into account when measuring the pulse length at the sample plane.

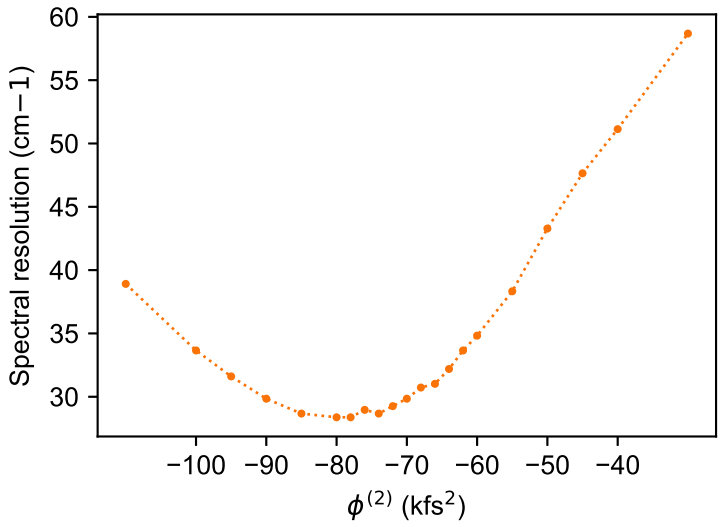

Figure 6.2 – Spectral resolution optimization using the WB AOPDF.

6.2.2 LockIn BW

With the AOPDF acting as the delay line, the SRS signal comes in the form of a voltage fluctuation at the output of the lockin module. To acquire a spectrum, the voltage needs to change within the time the acoustic wave propagates in the AOPDF. This means the bandwidth of the lockin module should allow fast voltage fluctuations, with time constants much smaller than the acoustic propagation time (25 to $33\,\mu s$, Table 5.1).

By varying the lockin integration time (i.e. its bandwidth, Table 6.2), we measured the resulting SRS spectral resolution using the WB AOPDF (Figure 6.3). In order to cancel the extra noise added by the AOPDF, we added a $1\,\mathrm{MHz}$ low-pass filter to the output of the lock-in amplifier, as described in Chapter 5.

We observe that the resolution improves with higher bandwidths, and less distortion is observed on the signal. The resolution is optimal for bandwidths of $0.5\,\mathrm{MHz}$ and above, reaching $28\,\mathrm{cm}^{-1}$. This resolution is lower than the one obtained under the same conditions with the mechanical delay line, by $3\,\mathrm{cm}^{-1}$.

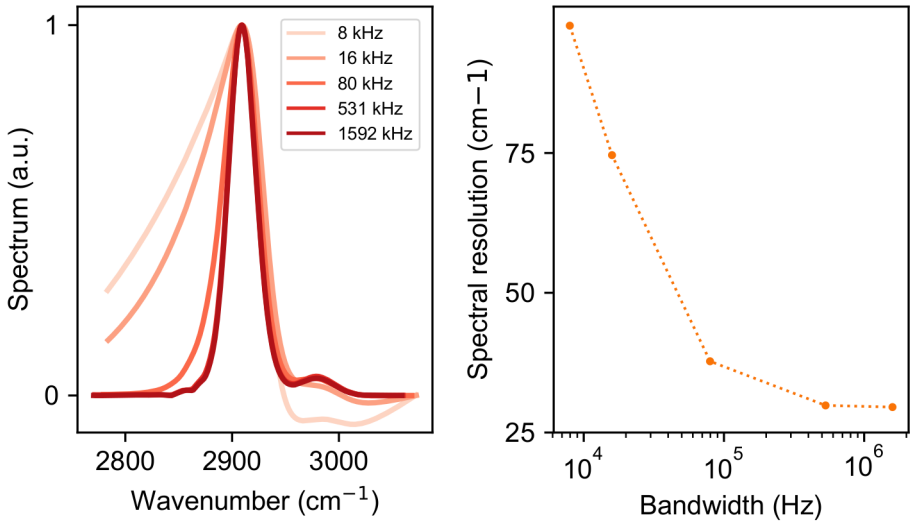

Figure 6.3 – Left: Effect of different lock-in bandwidths on the SRS spectrum. Right: Spectral resolution obtained for different lock-in bandwidths.

6.2.3 Signal distortion

In addition to the resolution, it is important to address how the AOPDF delay line can affect the shape of the signal. We compare the signal obtained on DMSO with the mechanical delay line and AOPDF delay line (Figure 6.4). In order to probe the two DMSO Raman peaks, the OPO center wavelength was set to center the SRS spectral window around $2950\,\mathrm{cm}^{-1}$ (Table 6.1).

Both the mechanical delay line and AOPDF methods are able to probe the two Raman peaks. However, slight differences can be observed between the two measurements. As expected from the achieved resolution, the mechanical delay line provides a slightly higher resolution. The relative amplitude of the two Raman peaks is additionally different for the two methods. This can be explained by a small change in the OPO center frequency between the two measurements. If the center frequency of the OPO changes by as little as $1\,\mathrm{nm}$, the spectral window of the SRS scheme is shifted by $10\,\mathrm{cm}^{-1}$. Because the SRS efficiency is not uniform across the spectral window, the acquired spectrum is very sensitive to shifts in this window (Figure (6.1)).

This notable difference between two similar measurements highlights one limitation of the current scheme. The center wavelength of the TiSaph and OPO are currently controlled through a feedback loop that allows 1 to $2\,\mathrm{nm}$ drifts. Such drifts can lead to significant shifts in the SRS spectral window on timescales of several hours. While most experiments presented in this work were done on much smaller timescales, we anticipate that more accurate control over the central wavelengths will be required in the future.

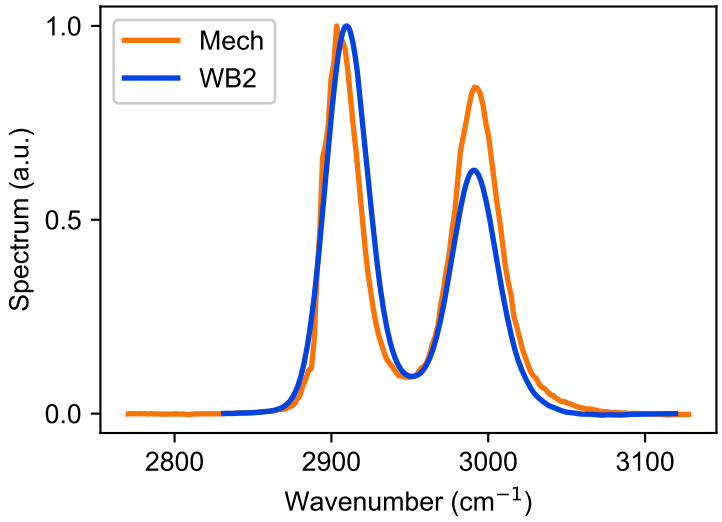

Figure 6.4 – Comparison of acquired spectra with the mechanical line or AOPDF on DMSO. The small differences can be explained by the slight change in central wavelength between the two measurements.

6.3 Measurement schemes

6.3.1 Mechanical imaging

The first measurement scheme relies on a grating pair to imprint dispersion on the pulses (Chapter 4). Using spectral focusing, different wavenumbers are probed by changing the delay between the pump and Stokes pulse. This delay is set by moving a mechanical delay line.

The parameters used in the different experiments are summarized in Table 6.3. *OPO Wavelength* and associated *Central wavenumber* correspond to the center of the SRS spectral window. The FWHM of this window is $110\,\mathrm{cm}^{-1}$ (Figure 6.1). The spectra were acquired over a range of wavenumbers covering 2 to 3 times the FWHM of the spectral window. The number of wavenumbers used to sample the spectra is set by *Nb wavenumbers*.

For each wavenumber, i.e. each delay value of the mechanical delay line, images were acquired and averaged. Each image measured a square field of view of size 50 to $200\,\mu\mathrm{m}$ (*Single image size (um)*). The number of pixels for each image was set to 100×100 to $200 \times 200\,\mathrm{pixel}$, limited memory of the software and acquisition cards. This parameter is *Single image size (pxl)*, and the resulting pixel to pixel distance is computed in *Pixel spacing*. In order to increase SNR while limiting photo-damage, averaging was done on a number of successive images (*Image Accum*), rather than by recording each pixel for longer.

On each pixel of an image, the output of the lockin amplifier was recorded

with a fast analog to digital converter (ATS460-128M PCI Digitizer, 125 MS/s, AlazarTech, Canada). The sampling frequency is given by *Sampling freq* and a number of samples by *Samples/pixel*. The bandwidth of the lockin amplifier was typically 8kHz when using the mechanical delay line (*Lockin Bandwidth*). The total time during which the laser beams were focused on each pixel is given by *Time/pixel*, and is slightly larger than the recording time. Due to the limited lockin bandwidth in this measurement scheme, a short time period was allowed between each pixel to allow the output to change value, thus reducing motion blur that can appear during image scanning. All samples acquired on the same pixel were then averaged in order to provide an image.

After acquiring each image (potentially several times for averaging) the wavenumber was changed to probe the next spectral value. The images at each wavenumber were stacked into a hyperspectral image. Each hyperpectral image consist therefore of a three dimensional data cube with dimension X, Y, and Wavenumber.

The effective recording time for such imaging is the product $(\textit{Nb wavenumbers}) \times (\textit{Total time/pixel}) \times (\textit{Single image size}) \times (\textit{Image Accum})$. However, additional idle time significantly increases this recording time, by almost 100%. The idle time is mainly due to the mechanical nature of the delay line, which takes about half a second to change position, as well as data transfer from the acquisition card to the computer which also takes about half a second. The final acquisition time for the figures presented are presented as *Total recording time*.

6.3.2 AOPDF imaging

Hyperspectral images were acquired using the AOPDF crystal to imprint delay and dispersion on the TiSaph laser pulses. Similarly to the mechanical scheme, the parameters used in the different experiments are summarized in Table 6.3. A few notable changes occur when using the AOPDF.

This fundamental difference emanates from the way in which the hyperspectral image is acquired. Instead of recording the data in the X and Y before change the wavenumber, the AOPDF allows one to record all wavenumbers for a given pixel before changing the X and Y position.

For each pixel, an acoustic wave is triggered in the AOPDF. During the propagation time of the acoustic wave, all delays are swept and a full SRS spectrum can be acquired. The lockin bandwidth time was set to $1.6\,\mathrm{MHz}$ to allow fast fluctuations of the signal. When using the WB crystal, an additional $1.35\,\mathrm{MHz}$ low-pass filter was used to restrict the bandwidth and improve the noise performance (Section 5.2.4). This filtering was not required with the HR crystal.

The time spent per pixel is set by the propagation time of the acoustic wave (Table 5.1). During this propagation, the pump and Stokes pulses are not always overlapping, further limiting the effective acquisition time. For the HR crystal, the pulses overlap during $10\,\mu\mathrm{s}$, corresponding to a $2.5\,\mathrm{ps}$ delay window. This

represents only a third of the duration of the acoustic wave. For the WB crystal, a $2.5\,\mathrm{ps}$ delay window corresponds to $16\,\mu\mathrm{s}$ of acoustic propagation. This duration is a much higher proportion of the acoustic propagation. As a result, about 70% of the measurement time is lost in the HR crystal due to non overlapping pulses. In the WB crystal only 35% of the time is lost due to non overlapping pulses, but this time is strictly necessary for the formation of the acoustic wave inside the crystal.

The number of samples per pixel (*Samples/pixel*), and acquisition rate (*Sampling freq (Ms/s)*) are specified in Table 6.3. In this case, the number of samples per pixel corresponds to the number of wavenumbers probed (*Nb wavenumbers*) as each time sample correspond to a different delay/wavenumber.

In this scheme, averaging over multiple images (*Image Accum*) is done by averaging successive hyperspectral images.

6.3.3 Image stitching

The size of the field of view allowed by our measurement system is limited by two factors. First the data acquisition cards and acquisition software impose a limit on the number of pixels that can be recorded. For a given pixel to pixel resolution, this memory limitation translates into a limit of the field of view. Second, the objective is slightly chromatic when imaging a large field of view. The result of this chromaticity is that the two laser beams focus will not overlap entirely on the edges of the image, and the SRS efficiency will drop. The non uniform SRS efficiency can be seen as vignetting on homogeneous samples. This vignetting could be calibrated and compensated for in future work. For images shown in the following, the field of view of single images was limited to 200 by $200\,\mu\mathrm{m}$, which minimizes vignetting.

In order to address larger fields of view, several images were patched together. From one image to the next, the X and Y center position of the image was changed using a translation stage (Scan-IM 130x85, Märzhäuser, Germany). Neighboring images were overlapping by at least 10%, and the pixels in the overlapping region were averaged across neighboring images. The number of images used to create the final image is given by *Stiching*. The total field of view is *Field of view*.

6.3.4 Orthogonal projection

Let N be the number of wavenumbers probed in a spectral measurements. Any spectrum can be seen as a vector of $\mathbb{R}^N$. Let $u_1, ..., u_k$ be k spectra of different chemical species. Let x be a spectrum.

Assuming $u_1, ..., u_k$ are linearly independent, the spectrum x can be projected

	Fig 6.6	Fig 6.7	Fig 6.8	Fig 6.9	Fig 6.11	Fig 6.12	Fig 6.13	Fig 6.14	Fig 6.15	Fig 6.16	Fig 6.17
Sample	Beads	Beads	Beads	Beads	Excip.	API	Excip.	API	Histo	Histo	MAN
Scheme	Mech	Mech	WB	WB	Mech	Mech	WB	WB	HR	HR	HR
TiSaph Power (mW)	15	15	15	15	10	15	15	15	15	15	15
OPO Power (mW)	7	15	7	7	7	7	7	7	20	20	20
OPO Wavelength (nm)	1045	1045	1045	1045	1053	1053	1053	1053	1045	1045	1045
Central wavenumber (cm^{-1})	2930	2930	2930	2930	3000	3000	3000	3000	2930	2930	2930
Nb wavenumbers	200	100	72	72	200	200	400	400	256	104	120
Single image size (um)	50x50	100x100	100x100	100x100	200x200	200x200	50x50	100x100	50x50	100x100	100x100
Single image size (pxl)	100x100	200x200	200x200	200x200	100x100	100x100	100x100	100x100	200x200	200x200	200x200
Pixel spacing (um)	0.5	0.5	0.5	0.5	2	2	0.5	1	0.25	0.5	0.5
Image Accum	1	1	4	4	2	2	20	20	10	2	2
Lockin Bandwidth	8kHz	8kHz	1.35MHz	1.35MHz	8kHz	8kHz	1.35MHz	1.35MHz	1.6MHz	1.6MHz	1.6MHz
Samples/pixel	504	256	72	72	504	504	400	400	256	104	120
Sampling freq (Ms/s)	20	10	5	5	20	20	20	20	20	10	20
Time/pixel (us)	30	30	25	25	30	30	25	25	40	40	40
Stiching	4x4	6x6	None	8x13	2x2	None	5x5	3x3	10x10	3x3	None
Field of view (um^2)	180^2	500^2	100^2	600x1100	360^2	200^2	225^2	270^2	450^2	450x800	100x100
Total recording time (min)	43	131	0.1	42	20	5	7	3	52	7	0.1

Table 6.3 – Experimental parameters used in measurements. Beads sample is the artificial sample with 3 polymer beads, oil, and bovine serum albumin crystals. Excip. is a sample containing three pharmaceutical excipients. API contains two polymorph forms F1 and F2 relevant in pharmacology.. Histo are frozen sections from human colon. MAN is a sample of delta-mannitol powder.

orthogonally on this family. The projection matrix is :

$$P = A(A^T A)^{-1} A^T \tag{6.1}$$

where A is the matrix containing $u_1, ..., u_k$ in columns. This projection corresponds to linearly unmixing the contribution of each chemical species to the final spectrum.

For each spectrum represented as a vector column x, the estimated content in the different species is given by $(A^T A)^{-1} A^T x$. In the results presented in this work, the images associated with different chemical components have been extracted with this method. Each pixel from the hyperspectral images was projected using orthogonal projection on known spectra.

6.4 Artificial sample

Prior to measuring biological samples, we investigated the use of spectrally focused SRS on artificial sample. This sample is a mixture of polymer beads, bovine serum albumin (BSA) crystals, and lipids (cooking oil). The polymer beads were of three different chemical composition and sizes: polystyrene ($30\,\mu m$ diameter), polymethyl methacrylate (PMMA, $20\,\mu m$), and melamine resin ($12\,\mu m$).

6.4.1 Mechanical line

Spectral imaging of the sample was first performed using the mechanical delay line and grating pair. The experimental parameters have been summarized in Table 6.3. Images were recorded for 200 values of the delay between the pump and Stokes, from -2 to $2\,\mathrm{ps}$.

The spectra of the five chemical species were acquired independently in pure samples (Figure (6.5)), using the same experimental parameters. The spectra shown distinct and characteristic features. The polystyrene component features two peaks around 2905 and $3055\,\mathrm{cm}^{-1}$ as expected from Raman shift standards (ASTM E1840). PMMA and Melamine resin present a single peak at 2952 and $2970\,\mathrm{cm}^{-1}$ respectively, both with different widths. Oil has a characteristically large spread at low wavenumber, which is consistent with oil having a strong SRS response between 2850 and $2950\,\mathrm{cm}^{-1}$. BSA lacks the $2850\,\mathrm{cm}^{-1}$ component that is characteristic of CH_2, in agreement with previous work using SRS on biological samples [28].

Hyperspectral images of the mixture are projected on all five spectra using orthogonal decomposition (Figure (6.5)). To provide a wider field of view, 16 hyperspectral images were acquired. Their projection on each species were patched together, resulting in a $260 \times 260\,\mu\mathrm{m}$ field of view with $0.5\,\mu\mathrm{m}$ pixel spacing.

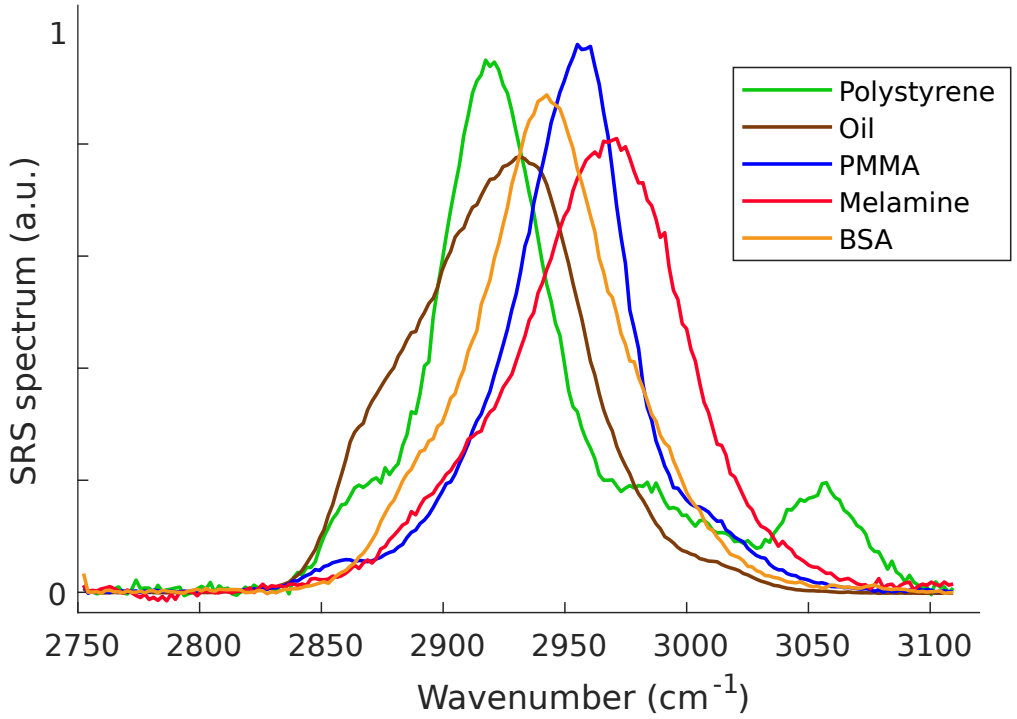

Figure 6.5 – SRS spectra of the five chemicals species in the artificial sample, acquired with the mechanical delay line.

The image shows the three types of beads sitting on a BSA crystal, with a space in the middle that is filled with oil. There is close to no cross talk between the different species, with only slight leakage from the PMMA signal onto the Melamine one. The image corresponding to the BSA also shows a signal at the center of the image where the oil is present. This is not due to cross talk, but rather the presence of the BSA crystal out of focus.

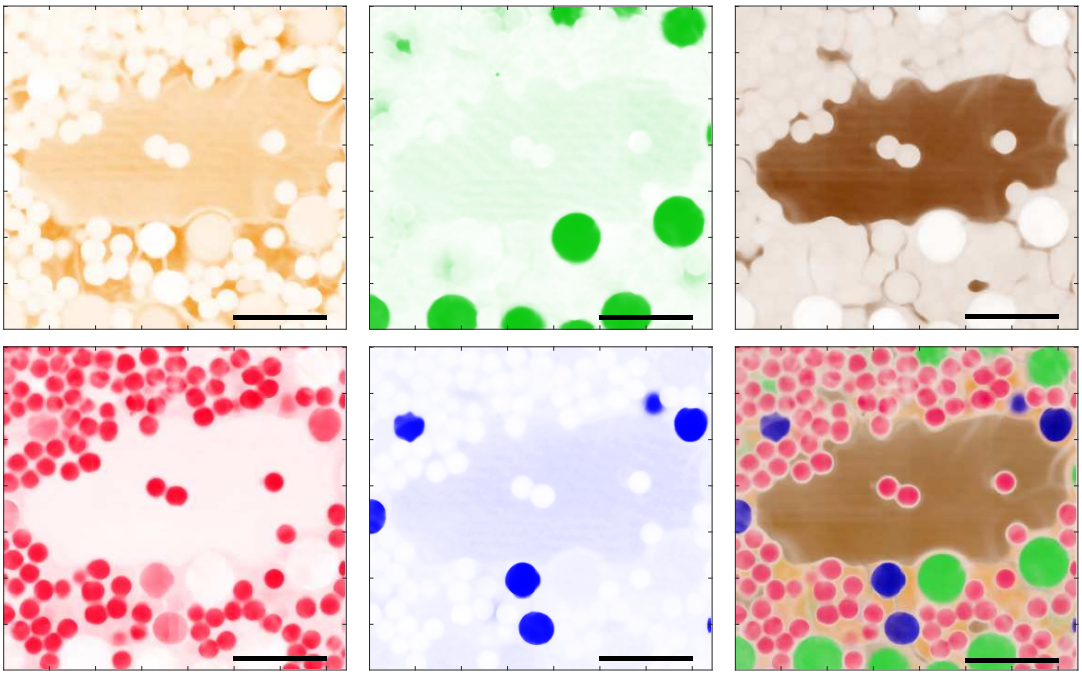

Figure 6.6 – Imaging of five different chemical species using the mechanical delay line. Top row, from left to right: BSA, Polystyrene, and Oil components. Bottom row: Melamine and PMMA components, superimposed image of all five images. The scale bar is 50 µm

The acquisition time can be reduced by reducing the number of delay / wavenumbers used to reconstruct the spectrum. By lowering this number to only 100 wavenumbers, one can still resolve the different species and acquire an image (Figure 6.7). This image shows a 0.5 by 0.5 mm field of view, and was acquired in two hours. In theory, the orthogonal decomposition (Section 6.3.4) only requires that the number of wavenumber be equal or greater than the number of chemical species. Experimentally, oversampling the spectrum with far more wavenumbers than there are chemical species, provides a much better image quality, is less prone to artifacts, and the redundancy can be used to reduce noise.

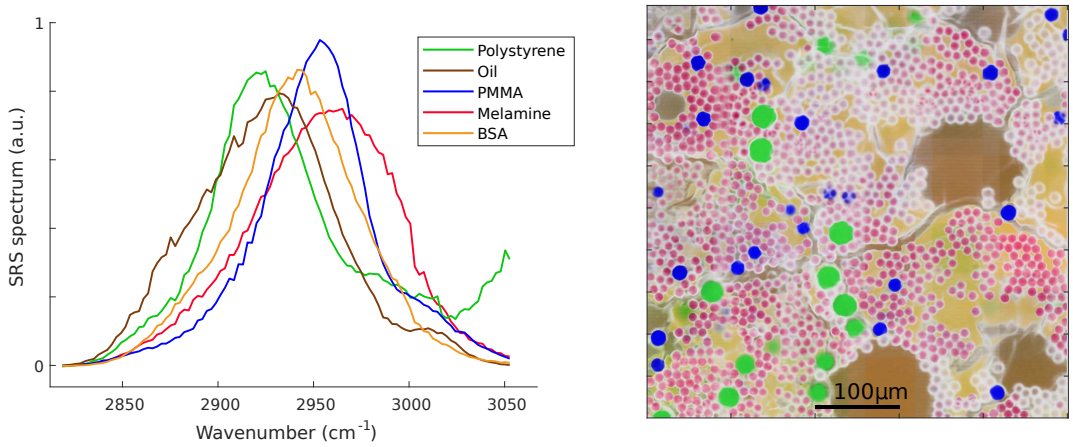

Figure 6.7 – Left: Spectra of the five chemical species present in the sample, acquired on pure samples. Right: Artificial sample imaged over a wide field of view. The scale bar is 100 µm

6.4.2 WB2 AOPDF

The artificial sample was imaged using the AOPDF to imprint delay and dispersion on the TiSaph laser pulses (Figure 6.8). The experimental parameters have been summarized in Table 6.3.

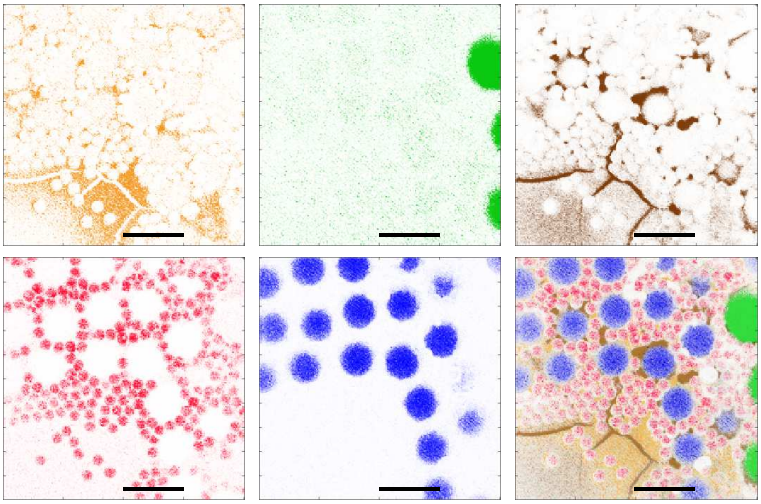

Figure 6.8 – Spectral imaging of the artificial sample, using the WB-AOPDF. Top row, from left to right: BSA, Polystyrene, and Oil components. Bottom row: Melamine and PMMA components, superimposed image of all five images. The scale bar is 25 µm

The hyperspectral image consist of 200 pixel by 200 pixel by 72 wavenumber, and was acquired in one second. Four such image were acquired per field of

view for averaging. The spectrum of each species was acquired on pure samples (Figure 6.8). These spectra are qualitatively equivalent to those obtained using the mechanical delay line (Figure 6.8), with only slight differences at the limits of the spectral window (2850 to $3050\,\mathrm{cm}^{-1}$). In particular we can note that the second peak of polystyrene, at $3055\,\mathrm{cm}^{-1}$ cannot be resolved in this case. This is consistent with the apodization of the spectral window that has been observed previously (Figure 6.1).

A large field of view is acquired by stitching together smaller ones (Figure 6.8). This field of view is 0.7 by $1.1\,\mathrm{mm}$, with $0.5\,\mu\mathrm{m}$ pixel spacing. Such field of view was acquired in under 45 minutes. The measurement is significantly faster than the equivalent image using the mechanical delay line.

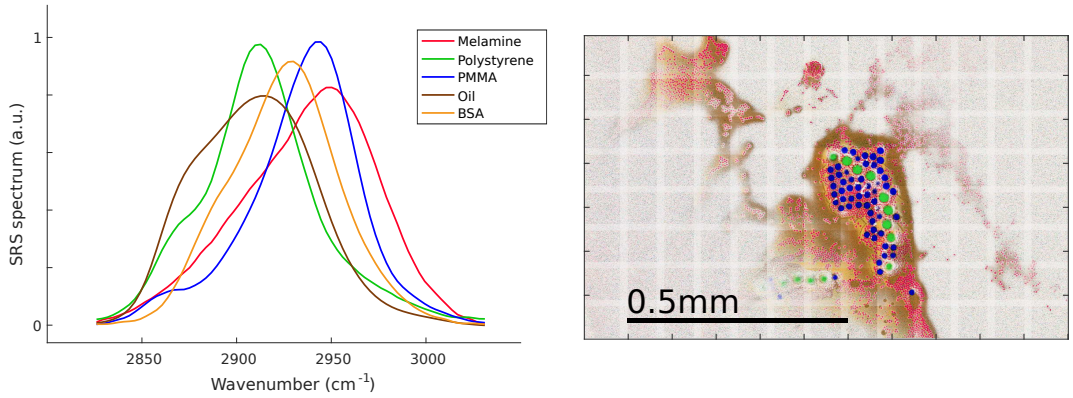

Figure 6.9 – Left: Spectra of the five chemical species present in the sample, acquired on pure samples using the AOPDF. Right: AOPDF imaging of the artificial sample over a wide field of view. The scale bar is $500\,\mu\mathrm{m}$

The sample shows polymer beads sitting under a BSA crystal. In this case the oil is only detected around the BSA crystal, adhering to it by capillarity. A large fraction of the field of view is devoid of significant signal. This illustrate the strong optical sectioning property of SRS microscopy. The image presented was acquired a few micron from the glass surface of the microscope slide. Only beads, oil, and crystal near the surface are detected. The BSA crystal extends to the full field of view but is out of focus.

This loss of focus highlight a difficulty encountered when imaging large fields of view of thin samples. In such experiments, it is important that the sample lies perfectly flat in the focal plane.

6.5 Pharmaceutical compounds

Quality control is a critical part of drug production. In solid pharmaceutical tablets, one key aspect of quality control is to monitor the size, arrangement,

and chemical composition of the crystals that make the tablet. Most chemical species posses different polymorphs, meaning that they can crystallize in more than one form. Polymorphs are endowed with the same chemical composition but their packing (i.e. arrangement) and/or conformation differ [69]. This induces differences in their physicochemical properties, and many parameters have been reported to be altered from one polymorph to another. Such parameters include solubility, dissolution kinetic, thermodynamic stability, bioavailability and toxicity [70].

The control of polymorphs is critical for the pharmaceutical industry, in order to provide the more efficient form in medicines. Polymorph screening is now a mandatory step when developing a new drug. The control of polymorphs is performed during the full extent of the tablet manufacturing process. This control is made difficult with the existence of concomitant polymorphs: when several enantiomer polymorphs can co-exist within a mixture at specific temperature and pressure

The most commonly used techniques to investigate polymorphism are: thermal analysis, differential scanning calorimetry (DSC), thermogravimetric analysis (TGA), Infrared spectroscopy, Raman spectroscopy, X-ray powder diffraction (XRD), solid state NMR and electron microscopy.

Raman spectroscopy is widely used in particular, due to its many advantages. This technique is non-destructive, and does not require any preparation. However, as discussed in Chapter 1, spontaneous Raman suffers from a small cross section, making it unpractical for imaging. Here we study the use of stimulated Raman scattering to perform chemical imaging of pharmaceutical powders.

Pharmaceutical tablets usually contain several excipients (i.e. inactive substances) in addition to the active pharmaceutical ingredients (API). These excipients help in the stabilization and delivery of the active compounds. We investigated three excipients: Mannitol (MAN), Polyethylene glycol (PEG), and Corn Starch (AMY). The API was clopidogrel, which is known to prevents platelet aggregations. This chemical species can present two enantiomers, F1 and F2, which are metabolized differently by the liver enzyme CYP2C19. The different samples were provided by Valérie Lavastre, Géraldine Pénarier, and Jean Alie (Sanofi Recherche & Développement, Montpellier, France). The spontaneous Raman spectra of all five species were provided as well, their CH-Stretch region is illustrated in Figure 6.10.

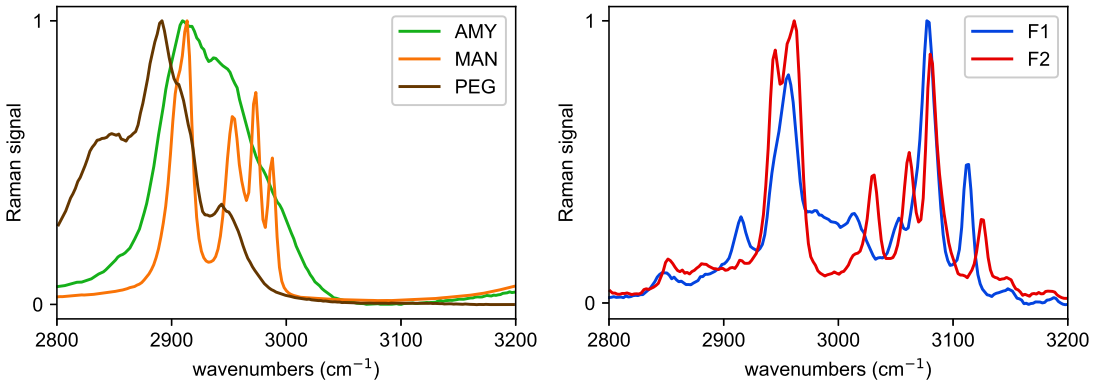

Figure 6.10 – Spontaneous Raman spectra of the excipients and active pharmaceutical ingredients.

6.5.1 Mechanical line

Measurements were performed first using the mechanical delay line and grating pair. The OPO center wavelength was set to $1053\,\mathrm{nm}$ such that the center of the spectral window in SF-SRS was around $3000\,\mathrm{cm}^{-1}$.

Two samples were imaged, one containing the three excipients, one containing the two forms of the API (Figure 6.11 and 6.12). The SRS signal of F1 and F2 was significantly lower than that of the excipients, making the simultaneous imaging of all five compounds experimentally difficult. This was exacerbated by the strong diffusive properties of the powders, making imaging of dense areas impossible in the forward direction. The amount of power on the sample was limited to 20 and $5\,\mathrm{mW}$ for the pump and Stokes beam respectively, higher powers led to damaging the samples.

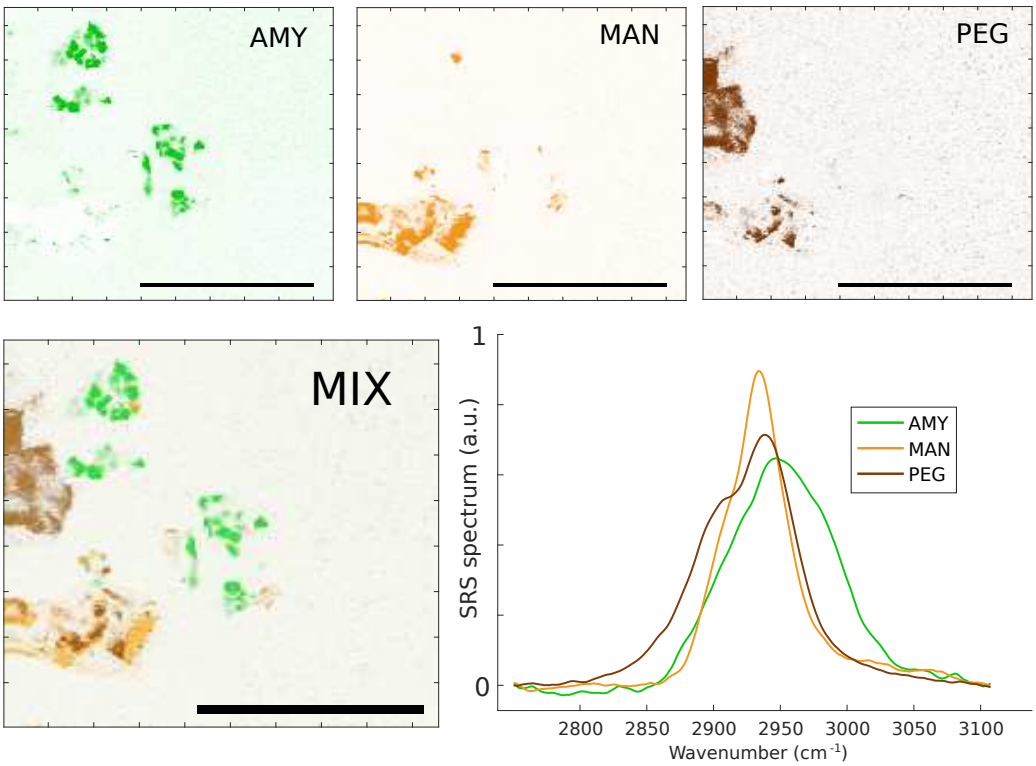

Figure 6.11 – Simultaneous imaging of the three excipients. Upper row, from left to right: Hyperspectral image projection on the Corn starch (AMY), Mannitol (MAN), and Polyethylene glycol (PEG) spectra. Lower row: Superimposed image of the three components (MIX) and spectra of the pure species. The scale bar is 200 µm

Both excipients and API can be identified with distinct spectra. For all species but mannitol, the acquired SRS spectra exhibit the same characteristic features as their spontaneous Raman counterparts. The notable difference is that spectral resolution is lower for SRS, as expected from our study. The sharp peaks in the spontaneous Raman spectra are smoothed in the SRS spectra.

The spectrum of mannitol stands out as notably different from the spontaneous Raman spectrum. This can be explained by the fact that mannitol itself has different polymorph: alpha, beta, and delta. The spontaneous Raman spectrum in Figure 6.10 is that of beta-mannitol, while the mannitol in the sample is mainly the delta form. More details on mannitol and its polymorphs are provided in Section 6.7. In particular, delta mannitol can transform into beta-mannitol upon hydration, with major changes to its SRS spectra. As seen from Figure 6.17, the SRS spectra of beta-mannitol does have two distinct peaks, as expected from its spontaneous Raman spectrum. Those two peaks, centered around 2910 and $2960\,\mathrm{cm}^{-1}$, introduce artefactual signal on the other components, that have contributions around these wavenumbers. This can be seen on Figure 6.11 through cross talk between mannitol and the two other excipients.

To accurately quantify the chemical composition of the sample, the spectrum of beta-mannitol should be measured and used as a fourth component in the orthogonal projection.

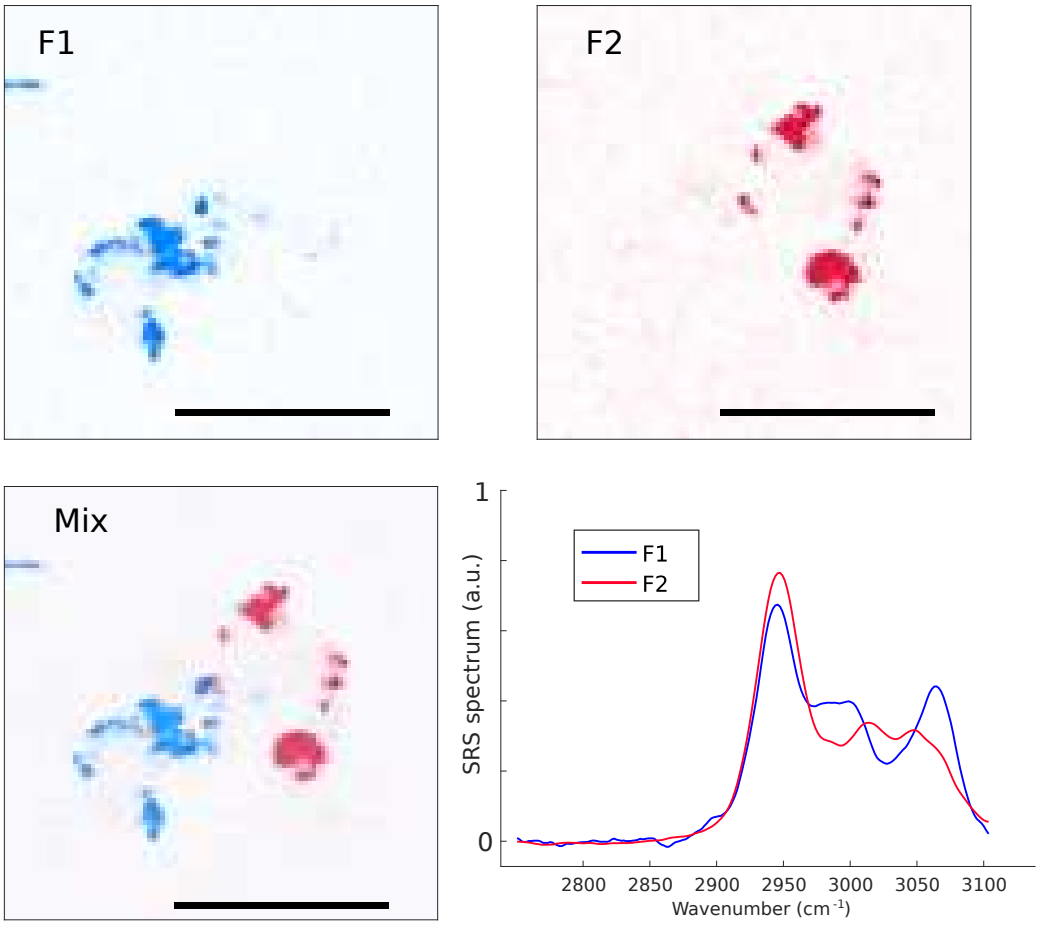

Figure 6.12 – Simultaneous imaging of the two active compounds. Upper row, from left to right: F1 and F2. Lower row: Superimposed image of the two components (MIX) and spectra of the pure species. The scale bar is $100\,\mu m$

The spectra of F1 and F2 match remarkably well their spontaneous Raman counterparts. Both exhibit a peak at $2950\,cm^{-1}$, F1 then has a plateau, drop in spectrum and another peak at $3075\,cm^{-1}$. F2 has the $2950\,cm^{-1}$ peak, followed by a signal drop, and two peaks at 3020 and $3060\,cm^{-1}$. This spectral resolution, down to relatively fine details, emphasizes the importance of centering the spectral window on the range of interest. The first attempt to perform this measurement using the AOPDF centered the spectral region around $2930\,cm^{-1}$, as done for the artificial sample. While this first attempt was successful at spectrally separating the excipients, that have low wavenumber components, it was unsuccessful at discriminating the two API polymorphs.

The size of the spectral window is a limit to spectrally focused SRS. In order to have a significant excitation over a wide range of wavenumbers, 2800 to $3100\,\mathrm{cm}^{-1}$ for the CH-stretch region, the optical pulses would have to be $70\,\mathrm{fs}$ or less. Precise phase control on both pulses to ensure that no third or fourth order phase terms impair the resolution. The use of the AOPDF to control the phase appears as a straightfoward solution to this issue. However, a $70\,\mathrm{fs}$ optical pulse at $800\,\mathrm{nm}$ would have a spectral width of $13.5\,\mathrm{nm}$. Such large spectral width would result in a large acoustic wave inside the AOPDF to diffract all wavelength (Section 6.1.9). The WB crystal would not be able to contain such large acoustic wave, but the HR crystal would. While the AOPDF would be a powerful tool to control the pulse phase, careful engineering would be required to address the full CH-stretch region with ultrashort pulses.

6.5.2 WB AOPDF

The two samples containing the excipients and the API, were imaged using the AOPDF (Figure 6.13 and 6.14).

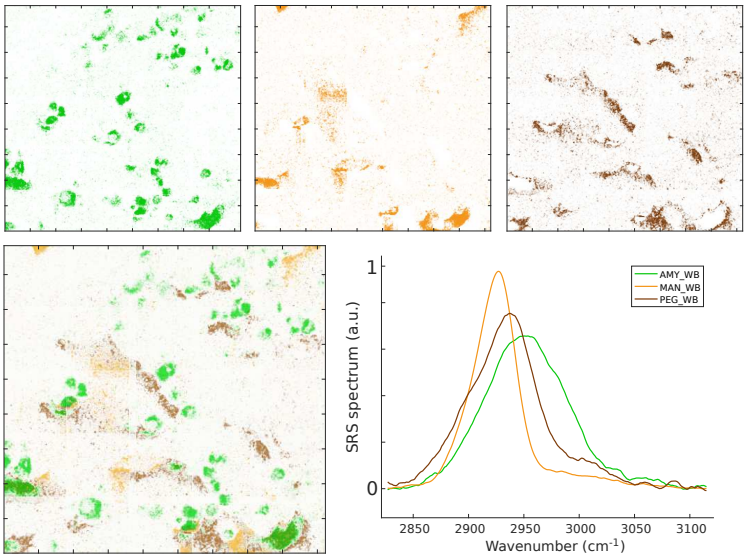

Figure 6.13 – Simultaneous AOPDF imaging of the three excipient. Upper row, from left to right: Hyperspectral image projection on the Corn starch (AMY), Mannitol (MAN), and Polyethylene glycol (PEG) spectra. Lower row: Superimposed image of the three components (MIX) and spectra of the pure species. The scale bar is $50\,\mu\mathrm{m}$.

The spectra of the excipients can still be obtained and discriminated using the AOPDF delay line with the WB crystal. The AMY and PEG spectra are exactly similar to the spectra obtained with the mechanical delay line, and to the spontaneous Raman spectra. This is due to their wide spectrum, for which the slight loss

in resolution does not change the spectrum significantly. The mannitol, however, presents a very different spectrum from one acquired with the mechanical delay line. The spectrum appears to be shifted by $10\,\mathrm{cm}^{-1}$ towards the low wavenumber as compared to the previous one (Figure 6.11). This shift could be explained by a transient change in the OPO center frequency, that would have occurred during the acquisition of the mannitol spectrum in the pure sample. Additional measurement would be required to confirm this hypothesis. If true, it would confirm the need for a less permissive locking of the OPO center frequency.

The effect of an inaccurate spectrum can be seen in the excipient projected images (Figure 6.13). The mannitol component has strong cross talk with both the AMY and PEG components.

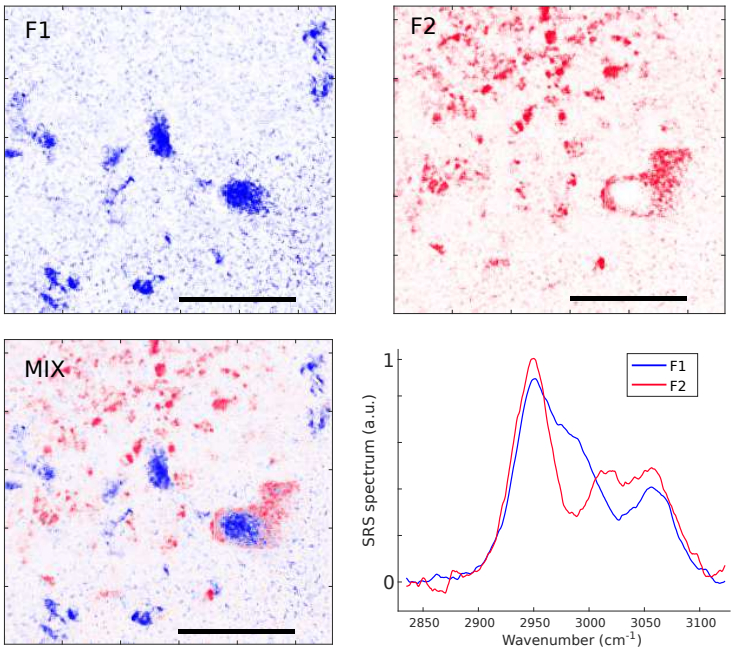

Figure 6.14 – Simultaneous AOPDF imaging of the two active compounds. Upper row, from left to right: F1 and F2. Lower row: Superimposed image of the two components (MIX) and spectra of the pure species. The scale bar is $100\,\mu\mathrm{m}$.

The analysis of the API polymorphs shows that the two species can still be resolved using the AOPDF. The spectra of F1 and F2 still show the typical features of the two species. While the crystals of the two species are clearly separated spatially, a strong F1 and F2 signal can be observed in the bottom right corner of the image. This signal is actually coming from a photo-damaged crystal. Two points can be made from this observation.

First, the orthogonal projection of the hyperspectral image on known spectra can lead to misinterpretation of the signal. During the projection, the spectrum x is expressed as a linear combination of the pure spectra Px (Section 6.3.4), and

an residual component $y = x - Px$. This residual spectral component cannot be expressed using the pure spectra, and should be close to the null vector if the sample only contains the known chemicals. In the case where a spectrum is of a chemically different nature than the pure spectra, we observe that the residual component becomes non-zero. This effect was observed early in this work, often after miss-calibration of the system, of photo-damage of the sample.

Second, in all of the results presented in this work, the amount of power delivered by the OPO on the sample plane was limiting. For shot noise limited measurement, and assuming linear photo-damage, the ideal ratio between the Stokes (modulated) and the pump (unmodulated) average laser power is 2 to 1. In most cases the ratio was inverted, leading to increased photo-damage and sub-optimal SNR. The two main source of OPO power loss are the AOM and the grating pair, with efficiency of 30% and 40% respectively. Significant improvements to both devices will be made in future work, which should allow for 50 to $80\,\mathrm{mW}$ of OPO power at the sample plane.

6.6 Histology

The goal of the present work is to provide chemically resolved imaging in biological samples. Proofs of concept that such imaging was possible has been shown in the past [28]. Contemporary to the work presented here, several research teams have showcased spectral focusing SRS with a fast delay line [24, 23, 56]. However, none of those studies have looked at human tissues.

The Institut Paoli-Calmettes provided Histological samples in the form of frozen sections of the colon and pancreas. These samples consisted of healthy, precancerous, and cancerous tissues from human patient surgery waste.

The section were 10 to $12\,\mu\mathrm{m}$ thick, and about $1\,\mathrm{cm}$ in area. Samples were observed using first phase contrast microscopy which identified the region of interest, then imaged using SF-SRS.

The hyperspectral images of biological samples were acquired on $50\,\mu\mathrm{m}$ fields of view, resolved at $0.25\,\mu\mathrm{m}$ pixel distance. Ten accumulations were performed per image, and 10x10 images were stitched together to form larger fields of view. The full acquisition time was 52 minutes.

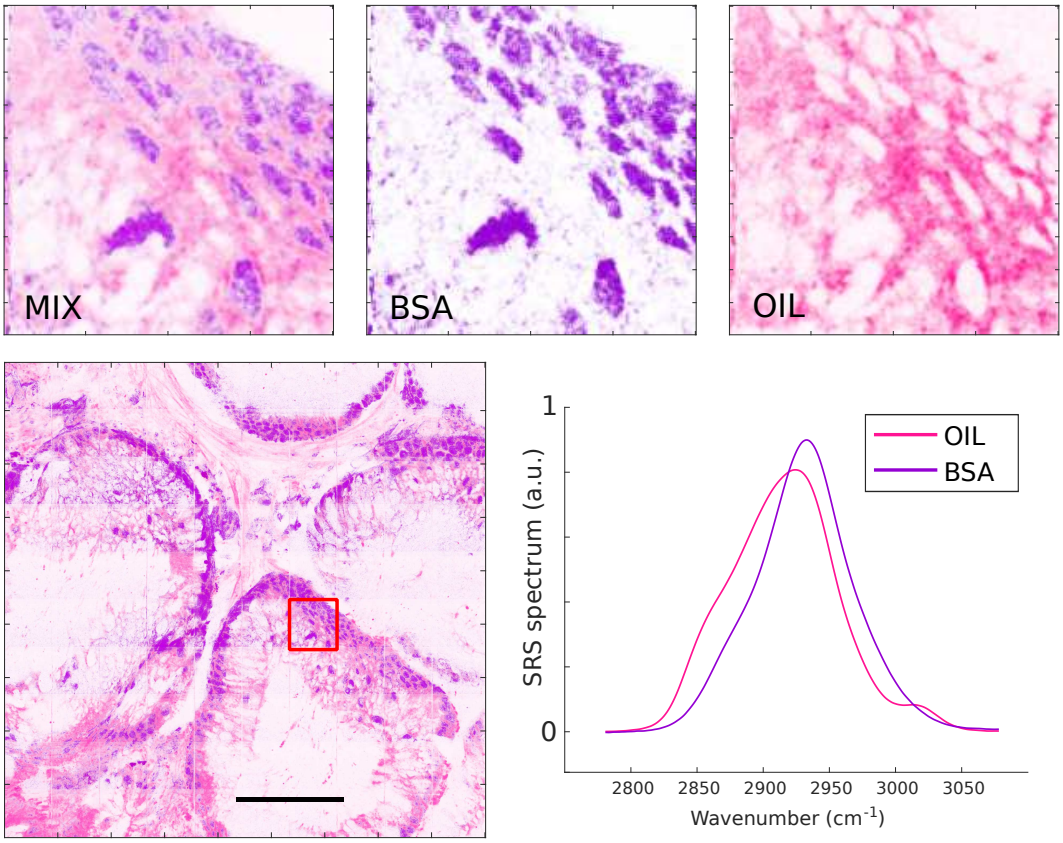

Figure 6.15 – Top row: zoomed in vignettes of a single image, 50 µm wide. From left to right, the mixed image, BSA, and Oil contribution. Bottom left: Histological AOPDF imaging of a frozen section of healthy human colon. The scale bar is 100 µm. The red square is the location of the top row images. Bottom right: Oil and BSA spectra acquired on pure samples.

The hyperspectral images were projected on the spectra of Oil and BSA, which were acquired independently on pure species (6.15). The projected images show very limited crosstalk, suggesting that the spectra of Oil and BSA create a reasonable projection basis for the measurement of "lipid" and "protein" signatures in tissues. This is different from other work, where the spectral components of the image are extracted *a posteriori* using multivariate curve resolution (MCR). While MCR is an interesting tool to extract components from a spectral image, it leads to image-dependent results and requires expert-based interpretation. Such variability should be avoided when *a priori* knowledge is available. Ultimately, SRS imaging would be a way to introduce quantitative analysis and standardize measurement in an otherwise qualitative and subjective analysis that is histology. Such standardization must rely on a well-defined, and not image-specific, spectral basis.

In addition to the BSA and Oil components, one can record the signature of

collagen fibers. An increased density of collagen generates a strong second harmonic signal. The added contrast mechanism provides important chemical information, in particular in the case of histology. The collagen structure arrangement in the extracellular matrix is an important marker of cancer, in addition to the spatial distribution and quantity of DNA in the tissue. Previous research has illustrated the feasibility of DNA monitoring in tissues by monitoring the $2967\,\mathrm{cm}^{-1}$ spectral line. We have not been able to spectrally discriminate proteins and DNA so far, but future research will prioritize these components.

The SHG signal was collected in the epi direction and the signal was averaged during the full acquisition of the pixel. A 450 by $800\,\mu\mathrm{m}$ field of view was acquired on a precancerous colon section, with a 0.5 pixel distance. This measurement took a total of 7 minutes.

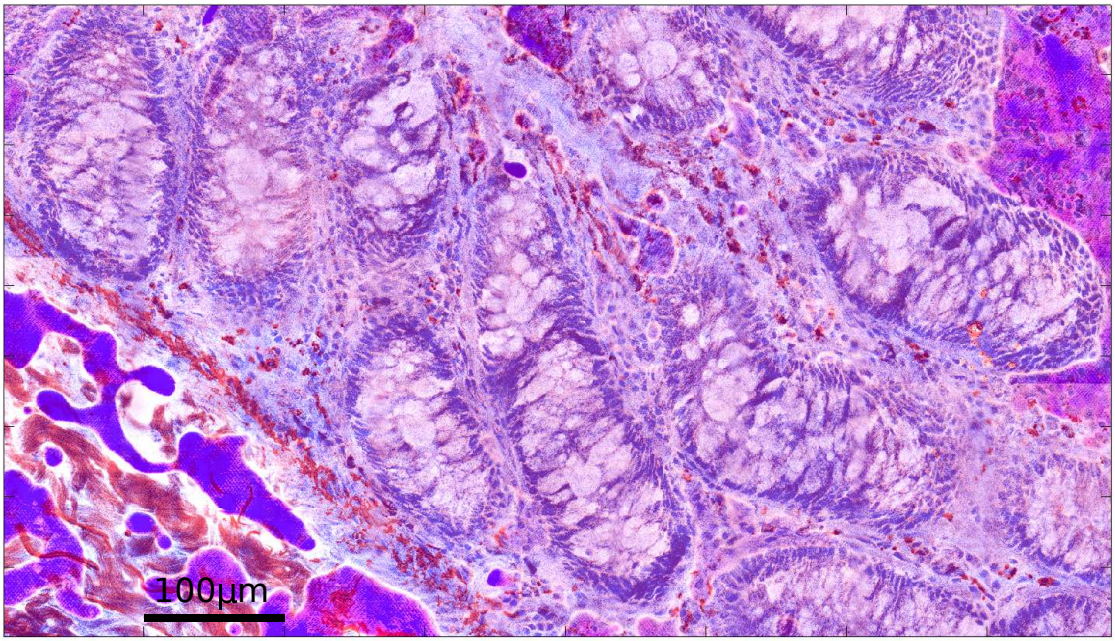

Figure 6.16 – Histological image of a precancerous colon frozen section imaged using SRS and SHG with the AOPDf delay line.

The three component image (Lipid, protein, collagen) is colored to resemble the staining of tissue sections generally used in histology. The cell membranes are colored pink as they would with Eosin, while the cell body and nuclei are violet to match the color of Hematoxylin. Collagen fibers are colored in red to imitate the safran dye.

This choice of color is suboptimal to represent three components, as it does not make use of the full color palette. The green component is almost absent from all three colors, while it could be taken advantage of to offer contrasting colors. Similarly, the choice was made not to show the three components independently. In histology, the dye are all simultaneously showing in the sample, making it

impossible to isolate the contribution of each component. These two choice were made to emphasize the fact that histological images are not designed to provide information is the most intelligible way.

By using spectral imaging, such as the method presented in this work, one has access to digital information on the sample and can choose to represent it in more appropriate ways. Artificial coloring on the different components has the ability to remove the limit set by natural coloring with dyes. Contrasting colors could replace the pink, violet, and red coloring, which can become ambiguous in terms of identification. As spectral imaging is not limited to two or three components, a single RGB image will not be sufficient to represent additional components. Projection of the data on a subset of components will have to be performed.

Additionally, the spectral information extracted from the samples provide more quantitative depth than can be analyzed by the human eye. Over-expression of DNA or collagen fiber orientation, among others metrics, could be extracted from this more quantitative data. These metrics would provide objective and standardized values that would help in the formation of diagnoses.

Ultimately, the physician has the responsibility of establishing a diagnosis, and his or her expertise is based on years of training and diagnostic methods. Spectral imaging opens new ways to address biological imaging that exceeds conventional methods. Collaboration between physicians and physicists is necessary to transform spectral imaging into a novel histological tool.

6.7 Time resolved measurements

The major interest of the AOPDF measurement is the ability to perform fast spectroscopic measurements. This is critical to study dynamic samples, such as live cells or chemical reactions. Using a mechanical delay line, we were unable to perform hyperspectral imaging of the tissues of fruit flies. Each image required several minutes to acquire, and the cells in the tissue under investigation were introducing massive motion artifacts that could not be corrected for. Therefore, Imaging of live tissues using the AOPDF will be the focus of future work.

As mentioned in Section 6.5.1, mannitol has three polymorphic crystal forms, alpha, beta, and delta. Upon hydration, the delta form changes its crystalline structure to become beta-mannitol. This process takes place within a few minutes, and has never been observed before.

In order to observe the transformation, we placed delta-mannitol powder in a chamber between a microscope slide and coverslip. A piece of dry paper was positioned in order to connect the inside and outside of the chamber. The paper was humidified from outside the chamber and introduced humidity in the chamber by capillarity. Introducing water slowly in the chamber with this method made possible the imaging of a single mannitol crystal, without major motion

or loss of focus. Hyperspectral images of mannitol crystals were recorded during the procedure and were projected on the delta and beta mannitol spectral components (Figure 6.17).

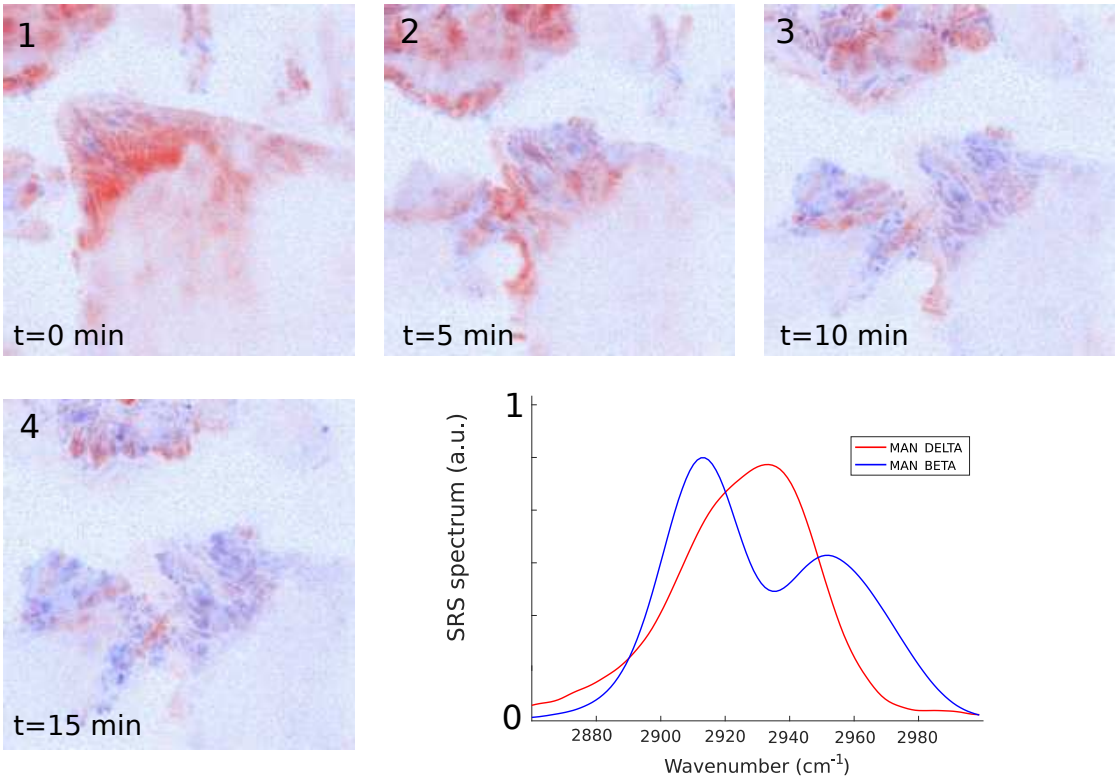

Figure 6.17 – Images 1 to 4, delta-mannitol (red) transformation into beta-mannitol (blue) during hydration. Images are taken at five minute intervals. Bottom right: SRS spectra of pure delta and beta mannitol.

Each image was a 100 by 100 µm field of view, with 0.5 pixel distance. 2 accumulations were done per image. The data projection was performed live, with two color images are directly visualized during acquisition.

The most important aspect of live image processing is the reduction of data. By recording a full spectrum per pixel, the hyperspectral images are typically much larger files than three color images. Saving and manipulating these files can significantly reduce the imaging rate of the system, with more time spent on data handling as opposed to data acquisition. Projecting each spectrum on a well defined basis with few components, the size of the images can be reduced by one or two orders of magnitude. While live data projection doubled the acquisition speed in our study, we anticipate that optimized data manipulation will be necessary in the future to further reduce the acquisition speed.

Transformation of delta-mannitol into beta-mannitol shows that following physico-chemical changes are possible with fast hyperpectral imaging. Two polymorphs

of the same species may have very different physiological effects. For this reason, understanding the transition from one form to the other is critical in drug manufacturing. The strong acidity of the stomach, for instance, can affect polymorphs and undermine the effect of the active compound. Future work will use fast SRS spectral imaging to investigate the effect of different pH levels in the stability of active pharmaceutical compounds.

Conclusion and future developments

This work presented the different aspects of hyperspectral imaging using stimulated Raman scattering, spectral focusing, and an acousto-optic delay line.

By gaining a deep understanding of the noise and signal in SRS, we were able to ensure that our system performed optimally at the shot noise limit. Modeling and experimental assessment of the pulse dispersion led to an optimal signal-resolution trade-off. We characterized and optimized the different components of the system, in particular the AOPDF delay line.

With this understanding, we were able to perform hyperspectral imaging at unprecedented rates, with spectra acquired every $25\,\mu s$. In addition to a higher acquisition rate, the optimized signal and noise allowed measurements of dilute samples such as frozen tissue sections. While further improvements are already envisioned, notably with increased laser power on the Stokes pulse, our work demonstrate the feasibility of stimulated Raman histology with this measurement scheme.

Spectral acquisition rate During the last decade, researchers have developed various schemes to acquire SRS spectra in the fastest way possible. Using an array of detectors, the group of Ji-Xin Cheng was able to measure the CH-stretch spectra of polymer beads and 3T3-L1 cells within $5\,\mu s$. Although this measurement scheme is not compatible with imaging, it sets the current state of the art for SRS spectroscopy. In our work, the effective measurement time per spectra is 10 and $15\,\mu s$ for the HR and WB AOPDF, respectively. The total time per spectra is further stretched to 33 and $25\,\mu s$ due to the formation and propagation of the acoustic wave inside the crystal. This measurement time is unprecedented in imaging of biological samples, and is at the physical limit of what can be achieved in such samples.

Spatial acquisition rate Even with such low acquisition times, the imaging speed for a 200 by $200\,pixel$ image is one second. In order to be compatible with live imaging, the acquisition rate in spectrally-resolved coherent Raman microscopy would still need to increase by one or two orders of magnitude. For this reason, we anticipate that the next significant improvement to this technology will come from spatial multiplexing. The signal acquisition is spatially limited to one focal spot currently, but multifocal measurement schemes have already been demonstrated [71]. Using higher laser power, one should be able to scale up the image acquisition rate, leading to important considerations on laser sources and data handling which are discussed below.

Higher power & broader spectrum Fiber lasers are a compact way to generate high power femtosecond pulses, and are already being used in SRS imaging. The main limitation of fiber lasers in this context is their noise level. Fiber lasers have typically much higher relative intensity noise (RIN) than their bulk counterpart, coming from amplification of the pump laser noise and spontaneous emission. As developed in chapter 3, a higher RIN impairs the signal to noise ratio (SNR) and limits the sensitivity of the SRS system. While balanced detection provides a way to cancel most of the excess laser noise, it introduces additional complexity that may not scale easily in a spatially multiplexed system [41, 38].

The spectral window investigated in this work is $110\,\mathrm{cm}^{-1}$ wide, which is nearly sufficient to acquire the full CH-stretch region. However, increased spectral range will be necessary to address wider spectral windows, in particular the fingerprint region. With wider spectral windows, the need for precise optical phase control will be even more present. The AOPDF might offer a compact way to address this challenge. A low noise, tunable, high power femtosecond laser combined with an AOPDF for fine dispersion control and delay scanning would constitute a compact SRS system suitable for both spatial multiplexing and fast spectral acquisition.

Data handling Live hypespectral imaging generates large streams of data that would require additional processing compared to current implementations. The size of the images acquired with our system is limited by the acquisition software memory to about $20\,\mathrm{MB}$. Ideally, for 30 images per second, 512 by $512\,\mathrm{pixel}$ images, 128 spectra points, and 14 bits samples, the stream of data represents $1.8\,\mathrm{GB/s}$. Capturing and processing such data streaming would require more computing power than is commonly used in SRS. Projection of the data on a known spectral basis, as has been done throughout this work, requires only matrix multiplication and would be scalable to live hyperspectral imaging. More advanced processing, such as spectral total variation (STV) denoising algorithm used by the Cheng group, would likely not be compatible with live imaging but could still be used for post-processing of the data.

Epi-SRS In this study, we have only been interested in transparent or weakly scattering samples, but a number of applications of SRS microspectroscopy are incompatible with forward collection. Imaging in thick or scattering samples, and ultimately in vivo, would require the use of epi-detected SRS and introduce additional challenge. Current work in our group has been focusing on combining coherent Raman with endoscopy, and future work will investigate the use of spectral focusing SRS in combination with this approach.

Multimodal expansion Our work focused on SRS in the CH-stretch region, but the technique is compatible with other non-linear imaging mechanisms. Second

harmonic generation was introduced to image collagen fibers in tissues, but other contrast mechanisms can also be added to the measurement. CARS, for instance, has not been used in this manner, but would provide information redundant with SRS (and would be used to increase the performance of the system).

Final words Over the past two decades, coherent Raman scattering has grown into a powerful and practical tool in various fields, particularly in the field of life science. With increased sensitivity, faster imaging, and spectral sensitivity, the range of application of this technique is still growing, with more challenging applications which incentivize further technological developments and research. The field of CRS microscopy is highly interdisciplinary and dynamic as a research field as it involves the fields of physics, biochemistry, and engineering.

Bibliography

[1] James K. Bowmaker. “Evolution of colour vision in vertebrates”. In: *Eye* 12.3 (May 1998), pp. 541–547. ISSN: 0950-222X. DOI: 10.1038/eye.1998.143. URL: http://www.nature.com/articles/eye1998143 (cit. on p. 9).

[2] Marcus T Cicerone and Charles H. Camp. “Histological coherent Raman imaging: a prognostic review”. In: *The Analyst* 143.1 (2018), pp. 33–59. ISSN: 0003-2654. DOI: 10.1039/C7AN01266G. arXiv: 1709.07325. URL: http://arxiv.org/abs/1709.07325%20http://xlink.rsc.org/?DOI=C7AN01266G (cit. on pp. 10, 11, 33).

[3] C. V. RAMAN and K. S. KRISHNAN. “A New Type of Secondary Radiation”. In: *Nature* 121.3048 (Mar. 1928), pp. 501–502. ISSN: 0028-0836. DOI: 10.1038/121501c0. arXiv: arXiv:1011.1669v3. URL: http://www.nature.com/articles/121501c0 (cit. on p. 12).

[4] Ji Xin Cheng and Xiaoliang Sunney Xie. *Coherent Raman Scattering Microscopy*. October. CRC Press, 2012, p. 603. ISBN: 9781439867655 (cit. on pp. 12, 16, 20, 43).

[5] P. D. Maker, R. W. Terhune, M Nisenoff, et al. “Effects of Dispersion and Focusing on the Production of Optical Harmonics”. In: *Physical Review Letters* 8.1 (Jan. 1962), pp. 21–22. ISSN: 0031-9007. DOI: 10.1103/PhysRevLett.8.21. URL: https://link.aps.org/doi/10.1103/PhysRevLett.8.21 (cit. on p. 13).

[6] R. F. Begley, A. B. Harvey, and R. L. Byer. “Coherent anti-Stokes Raman spectroscopy”. In: *Applied Physics Letters* 25.7 (Oct. 1974), pp. 387–390. ISSN: 0003-6951. DOI: 10.1063/1.1655519. URL: http://aip.scitation.org/doi/10.1063/1.1655519 (cit. on p. 13).

[7] M. D. Duncan, J. Reintjes, and T. J. Manuccia. “Scanning coherent anti-Stokes Raman microscope”. In: *Optics Letters* 7.8 (Aug. 1982), p. 350. ISSN: 0146-9592. DOI: 10.1364/OL.7.000350. URL: https://www.osapublishing.org/abstract.cfm?URI=ol-7-8-350 (cit. on p. 13).

[8] Andreas Zumbusch, Gary R. Holtom, and X. Sunney Xie. “Three-Dimensional Vibrational Imaging by Coherent Anti-Stokes Raman Scattering”. In: *Physical Review Letters* 82.20 (May 1999), pp. 4142–4145. ISSN: 0031-9007. DOI: 10.1103/PhysRevLett.82.4142. arXiv: arXiv:1011.1669v3. URL: https://link.aps.org/doi/10.1103/PhysRevLett.82.4142 (cit. on pp. 13, 33).

[9] C. L. Evans, E. O. Potma, M. Puoris'haag, et al. "Chemical imaging of tissue in vivo with video-rate coherent anti-Stokes Raman scattering microscopy". In: *Proceedings of the National Academy of Sciences* 102.46 (Nov. 2005), pp. 16807–16812. ISSN: 0027-8424. DOI: 10.1073/pnas.0508282102. URL: http://www.pnas.org/cgi/doi/10.1073/pnas.0508282102 (cit. on p. 13).

[10] EJ Woodbury and WK Ng. "Ruby laser operation in near IR". In: *Proceedings of the Institute of Radio Engineers* 50.11 (1962), p. 2367 (cit. on p. 13).

[11] E. Ploetz, S. Laimgruber, S. Berner, et al. "Femtosecond stimulated Raman microscopy". In: *Applied Physics B* 87.3 (May 2007), pp. 389–393. ISSN: 0946-2171. DOI: 10.1007/s00340-007-2630-x. URL: http://link.springer.com/10.1007/s00340-007-2630-x (cit. on p. 13).

[12] Pascal Berto, Esben Ravn Andresen, and Hervé Rigneault. "Background-Free Stimulated Raman Spectroscopy and Microscopy". In: *Physical Review Letters* 112.5 (Feb. 2014), p. 053905. ISSN: 0031-9007. DOI: 10.1103/PhysRevLett.112.053905. URL: http://link.aps.org/doi/10.1103/PhysRevLett.112.053905%20https://link.aps.org/doi/10.1103/PhysRevLett.112.053905 (cit. on pp. 13, 33).

[13] Chi Zhang and Ji-Xin Cheng. "Perspective: Coherent Raman scattering microscopy, the future is bright". In: *APL Photonics* 3.9 (Sept. 2018), p. 090901. ISSN: 2378-0967. DOI: 10.1063/1.5040101. URL: http://aip.scitation.org/doi/10.1063/1.5040101 (cit. on p. 14).

[14] Hervé Rigneault and Pascal Berto. "Tutorial: Coherent Raman light matter interaction processes". In: *APL Photonics* 3.9 (Sept. 2018), p. 091101. ISSN: 2378-0967. DOI: 10.1063/1.5030335. URL: http://aip.scitation.org/doi/10.1063/1.5030335 (cit. on pp. 16, 30, 33, 43).

[15] Robert W. Boyd and Barry R. Masters. "Nonlinear Optics, Third Edition". In: *Journal of Biomedical Optics* 14.2 (2009), p. 029902. ISSN: 10833668. DOI: 10.1117/1.3115345. arXiv: arXiv:1011.1669v3. URL: http://biomedicaloptics.spiedigitallibrary.org/article.aspx?doi=10.1117/1.3115345 (cit. on p. 30).

[16] J.-X. Cheng and X. S. Xie. "Vibrational spectroscopic imaging of living systems: An emerging platform for biology and medicine". In: *Science* 350.6264 (Nov. 2015), aaa8870–aaa8870. ISSN: 0036-8075. DOI: 10.1126/science.aaa8870. arXiv: NIHMS150003. URL: http://www.sciencemag.org/cgi/doi/10.1126/science.aaa8870 (cit. on p. 33).

[17] P. D. Maker and R. W. Terhune. “Study of Optical Effects Due to an Induced Polarization Third Order in the Electric Field Strength”. In: *Physical Review* 137.3A (Feb. 1965), A801–A818. ISSN: 0031-899X. DOI: 10.1103/PhysRev.137.A801. URL: https://link.aps.org/doi/10.1103/PhysRev.137.A801 (cit. on p. 33).

[18] N. Bloembergen. “The Stimulated Raman Effect”. In: *American Journal of Physics* 35.11 (Nov. 1967), pp. 989–1023. ISSN: 0002-9505. DOI: 10.1119/1.1973774. URL: http://aapt.scitation.org/doi/10.1119/1.1973774 (cit. on p. 33).

[19] Christian W. Freudiger, Wei Min, Brian G. Saar, et al. “Label-Free Biomedical Imaging with High Sensitivity by Stimulated Raman Scattering Microscopy”. In: *Science* 322.5909 (Dec. 2008), pp. 1857–1861. ISSN: 0036-8075. DOI: 10.1126/science.1165758. URL: http://www.sciencemag.org/cgi/content/abstract/322/5909/1857%20http://www.sciencemag.org/lookup/doi/10.1126/science.1165758 (cit. on p. 33).

[20] P. Nandakumar, A. Kovalev, and A. Volkmer. “Vibrational imaging based on stimulated Raman scattering microscopy”. In: *New Journal of Physics* 11.3 (Mar. 2009), p. 033026. ISSN: 1367-2630. DOI: 10.1088/1367-2630/11/3/033026. URL: http://stacks.iop.org/1367-2630/11/i=3/a=033026?key=crossref.c6197bc3f484bd8f7b9a8f9d9895d820 (cit. on p. 33).

[21] Ruoyu He, Yongkui Xu, Lili Zhang, et al. “Dual-phase stimulated Raman scattering microscopy for real-time two-color imaging”. In: *Optica* 4.1 (Jan. 2017), p. 44. ISSN: 2334-2536. DOI: 10.1364/OPTICA.4.000044. URL: https://www.osapublishing.org/abstract.cfm?URI=optica-4-1-44 (cit. on pp. 33, 57).

[22] Pascal Berto, Camille Scotté, Frédéric Galland, et al. “Programmable single-pixel-based broadband stimulated Raman scattering”. In: *Optics Letters* 42.9 (May 2017), p. 1696. ISSN: 0146-9592. DOI: 10.1364/OL.42.001696. URL: https://www.osapublishing.org/abstract.cfm?URI=ol-42-9-1696 (cit. on p. 33).

[23] Mohammed S. Alshaykh, Chien-Sheng Liao, Oscar E. Sandoval, et al. “High-speed stimulated hyperspectral Raman imaging using rapid acousto-optic delay lines”. In: *Optics Letters* 42.8 (Apr. 2017), p. 1548. ISSN: 0146-9592. DOI: 10.1364/OL.42.001548. URL: https://www.osapublishing.org/abstract.cfm?URI=ol-42-8-1548 (cit. on pp. 33, 57, 61, 112).

[24] Chien-Sheng Liao, Kai-Chih Huang, Weili Hong, et al. “Stimulated Raman spectroscopic imaging by microsecond delay-line tuning”. In: *Optica* 3.12 (Dec. 2016), p. 1377. ISSN: 2334-2536. DOI: 10.1364/OPTICA.3.001377. URL: http://www.osapublishing.org/optica/abstract.cfm?URI=optica-3-12-1377%7B%5C%%7D5Cnhttps://www.osapublishing.org/

abstract.cfm?URI=optica-3-12-1377%20https://www.osapublishing.org/abstract.cfm?URI=optica-3-12-1377 (cit. on pp. 33, 83, 112).

[25] Chien-Sheng Liao, Ji-Xin Cheng, and Pu Wang. "In Vivo Spectroscopic Imaging by Retrieving Stimulated Raman Signal from Highly Scattered Photons". In: *Frontiers in Optics 2015*. October. Washington, D.C.: OSA, 2015, LTu3H.2. ISBN: 978-1-943580-03-3. DOI: 10.1364/LS.2015.LTu3H.2. URL: http://www.osapublishing.org/abstract.cfm?URI=LS-2015-LTu3H.2%20https://www.osapublishing.org/abstract.cfm?URI=LS-2015-LTu3H.2 (cit. on p. 33).

[26] Chien-Sheng Liao, Mikhail N Slipchenko, Ping Wang, et al. "Microsecond scale vibrational spectroscopic imaging by multiplex stimulated Raman scattering microscopy". In: *Light: Science & Applications* 4.3 (Mar. 2015), e265–e265. ISSN: 2047-7538. DOI: 10.1038/lsa.2015.38. URL: http://www.nature.com/doifinder/10.1038/lsa.2015.38%20http://www.nature.com/articles/lsa201538 (cit. on p. 33).

[27] Christian W. Freudiger, Wenlong Yang, Gary R. Holtom, et al. "Stimulated Raman scattering microscopy with a robust fibre laser source". In: *Nature Photonics* 8.2 (Feb. 2014), pp. 153–159. ISSN: 1749-4885. DOI: 10.1038/nphoton.2013.360. arXiv: NIHMS150003. URL: http://stke.sciencemag.org/cgi/doi/10.1126/scisignal.2001449%20http://www.nature.com/doifinder/10.1038/nphoton.2013.360%20http://dx.doi.org/10.1038/nphoton.2013.360%20http://www.nature.com/articles/nphoton.2013.360 (cit. on pp. 33, 34, 53).

[28] Fa-Ke Lu, Srinjan Basu, Vivien Igras, et al. "Label-free DNA imaging in vivo with stimulated Raman scattering microscopy". In: *Proceedings of the National Academy of Sciences* 112.37 (Sept. 2015), pp. 11624–11629. ISSN: 0027-8424. DOI: 10.1073/pnas.1515121112. URL: http://www.pnas.org.proxy.osti.gov/content/112/37/11624.long%20http://www.pnas.org/lookup/doi/10.1073/pnas.1515121112 (cit. on pp. 33, 102, 112).

[29] Dan Fu, Wenlong Yang, and Xiaoliang Sunney Xie. "Label-free Imaging of Neurotransmitter Acetylcholine at Neuromuscular Junctions with Stimulated Raman Scattering". In: *Journal of the American Chemical Society* 139.2 (Jan. 2017), pp. 583–586. ISSN: 0002-7863. DOI: 10.1021/jacs.6b10727. URL: http://pubs.acs.org/doi/10.1021/jacs.6b10727 (cit. on pp. 33, 57).

[30] Yasuyuki Ozeki, Wataru Umemura, Yoichi Otsuka, et al. "High-speed molecular spectral imaging of tissue with stimulated Raman scattering". In: *Nature Photonics* 6.12 (Dec. 2012), pp. 845–851. ISSN: 1749-4885. DOI: 10.1038/nphoton.2012.263. URL: http://www.nature.com/doifinder/10.1038/nphoton.2012.263%20http://www.nature.com/articles/nphoton.2012.263 (cit. on pp. 33, 57).

[31] Yoshifumi Wakisaka, Yuta Suzuki, Osamu Iwata, et al. “Probing the metabolic heterogeneity of live Euglena gracilis with stimulated Raman scattering microscopy”. In: *Nature Microbiology* 1.10 (Oct. 2016), p. 16124. ISSN: 2058-5276. DOI: 10.1038/nmicrobiol.2016.124. URL: http://dx.doi.org/10.1038/nmicrobiol.2016.124%20http://www.nature.com/articles/nmicrobiol2016124 (cit. on p. 33).

[32] Lu Wei, Zhixing Chen, Lixue Shi, et al. “Super-multiplex vibrational imaging”. In: *Nature* 544.7651 (Apr. 2017), pp. 465–470. ISSN: 0028-0836. DOI: 10.1038/nature22051. arXiv: NIHMS150003. URL: http://dx.doi.org/10.1038/nature22051%20http://www.nature.com/doifinder/10.1038/nature22051 (cit. on p. 33).

[33] Martin Josef Winterhalder and Andreas Zumbusch. “Beyond the borders — Biomedical applications of non-linear Raman microscopy”. In: *Advanced Drug Delivery Reviews* 89 (July 2015), pp. 135–144. ISSN: 0169409X. DOI: 10.1016/j.addr.2015.04.024. URL: http://dx.doi.org/10.1016/j.addr.2015.04.024%20http://linkinghub.elsevier.com/retrieve/pii/S0169409X15000927 (cit. on p. 33).

[34] Minbiao Ji, Spencer Lewis, Sandra Camelo-Piragua, et al. “Detection of human brain tumor infiltration with quantitative stimulated Raman scattering microscopy”. In: *Science Translational Medicine* 7.309 (Oct. 2015), 309ra163–309ra163. ISSN: 1946-6234. DOI: 10.1126/scitranslmed.aab0195. URL: http://stm.sciencemag.org/lookup/doi/10.1126/scitranslmed.aab0195 (cit. on p. 33).

[35] Daniel A. Orringer, Balaji Pandian, Yashar S. Niknafs, et al. “Rapid intraoperative histology of unprocessed surgical specimens via fibre-laser-based stimulated Raman scattering microscopy”. In: *Nature Biomedical Engineering* 1.2 (Feb. 2017), p. 0027. ISSN: 2157-846X. DOI: 10.1038/s41551-016-0027. URL: http://www.nature.com/articles/s41551-016-0027 (cit. on p. 33).

[36] Yasuyuki Ozeki, Fumihiro Dake, Shin’ichiro Kajiyama, et al. “Analysis and experimental assessment of the sensitivity of stimulated Raman scattering microscopy”. In: *Optics Express* 17.5 (Mar. 2009), p. 3651. ISSN: 1094-4087. DOI: 10.1364/OE.17.003651. URL: https://www.osapublishing.org/oe/abstract.cfm?uri=oe-17-5-3651 (cit. on p. 34).

[37] Yasuyuki Ozeki, Yuma Kitagawa, Kazuhiko Sumimura, et al. “Stimulated Raman scattering microscope with shot noise limited sensitivity using subharmonically synchronized laser pulses”. In: *Optics Express* 18.13 (June 2010), p. 13708. ISSN: 1094-4087. DOI: 10.1364/OE.18.013708. URL: https://www.osapublishing.org/abstract.cfm?URI=oe-18-13-13708 (cit. on pp. 34, 45).

[38] Francesco Crisafi, Vikas Kumar, Tullio Scopigno, et al. “In-line balanced detection stimulated Raman scattering microscopy”. In: *Scientific Reports* 7.1 (Dec. 2017), p. 10745. ISSN: 2045-2322. DOI: 10.1038/s41598-017-09839-1. URL: http://dx.doi.org/10.1038/s41598-017-09839-1%20http://www.nature.com/articles/s41598-017-09839-1 (cit. on pp. 34, 53, 119).

[39] WA Gardner. *Statistical Spectral Analysis A Nonprobabilistic Theory*. 1986. URL: http://linkinghub.elsevier.com/retrieve/pii/016516849090084C%7B%5C%%7D5Cnhttp://dl.acm.org/citation.cfm?id=19260 (cit. on p. 36).

[40] Franklyn Quinlan, Tara M Fortier, Haifeng Jiang, et al. “Analysis of shot noise in the detection of ultrashort optical pulse trains”. In: *Journal of the Optical Society of America B* 30.6 (June 2013), p. 1775. ISSN: 0740-3224. DOI: 10.1364/JOSAB.30.001775. arXiv: 1302.6206. URL: http://arxiv.org/abs/1302.6206%7B%5C%%7D5Cnhttp://www.nature.com/nphoton/journal/vaop/ncurrent/full/nphoton.2013.33.html%20https://www.osapublishing.org/abstract.cfm?URI=josab-30-6-1775%20http://arxiv.org/abs/1302.6206%7B%5C%%7D5Cnhttp://www.nature.com/nphoton/journal/vaop/ncu (cit. on p. 37).

[41] Keisuke Nose, Yasuyuki Ozeki, Tatsuya Kishi, et al. “Sensitivity enhancement of fiber-laser-based stimulated Raman scattering microscopy by collinear balanced detection technique”. In: *Optics Express* 20.13 (June 2012), p. 13958. ISSN: 1094-4087. DOI: 10.1364/OE.20.013958. URL: https://www.osapublishing.org/oe/abstract.cfm?uri=oe-20-13-13958 (cit. on pp. 53, 119).

[42] Sandro Heuke, Barbara Sarri, Xavier Audier, et al. “Simultaneous dual-channel stimulated Raman scattering microscopy demultiplexed at distinct modulation frequencies”. In: *Optics Letters* 43.15 (Aug. 2018), p. 3582. ISSN: 0146-9592. DOI: 10.1364/OL.43.003582. URL: https://www.osapublishing.org/abstract.cfm?URI=ol-43-15-3582 (cit. on p. 53).

[43] Jue Su, Ruxin Xie, Carey K. Johnson, et al. “Single-fiber-laser-based wavelength tunable excitation for coherent Raman spectroscopy”. In: *Journal of the Optical Society of America B* 30.6 (June 2013), p. 1671. ISSN: 0740-3224. DOI: 10.1364/JOSAB.30.001671. URL: https://www.osapublishing.org/abstract.cfm?URI=josab-30-6-1671 (cit. on pp. 55, 68).

[44] B. Broers, L. D. Noordam, and H. B. Van Linden Van Den Heuvell. “Diffraction and focusing of spectral energy in multiphoton processes”. In: *Physical Review A* 46.5 (1992), pp. 2749–2756. ISSN: 10502947. DOI: 10.1103/PhysRevA.46.2749 (cit. on p. 55).

[45] E Gershgoren, R a Bartels, J T Fourkas, et al. “Simplified setup for high-resolution spectroscopy that uses ultrashort pulses”. In: *Optics Letters* 28.5 (Mar. 2003), p. 361. ISSN: 0146-9592. DOI: 10.1364/OL.28.000361. URL: https://www.osapublishing.org/abstract.cfm?URI=ol-28-5-361 (cit. on p. 55).

[46] Thomas Hellerer, Annika M.K. Enejder, and Andreas Zumbusch. “Spectral focusing: High spectral resolution spectroscopy with broad-bandwidth laser pulses”. In: *Applied Physics Letters* 85.1 (July 2004), pp. 25–27. ISSN: 00036951. DOI: 10.1063/1.1768312. URL: http://aip.scitation.org/doi/10.1063/1.1768312%20http://scitation.aip.org/content/aip/journal/apl/85/1/10.1063/1.1768312 (cit. on p. 57).

[47] Israel Rocha-Mendoza, Wolfgang Langbein, Peter Watson, et al. “Differential coherent anti-Stokes Raman scattering microscopy with linearly chirped femtosecond laser pulses”. In: *Optics Letters* 34.15 (Aug. 2009), p. 2258. ISSN: 0146-9592. DOI: 10.1364/OL.34.002258. URL: https://www.osapublishing.org/abstract.cfm?URI=ol-34-15-2258 (cit. on p. 57).

[48] F. Adrian Pegoraro, Andrew Ridsdale, Une Lausten, et al. “All-fiber multimodal cars microscopy of live cells”. In: *CLEO/Europe - EQEC 2009 - European Conference on Lasers and Electro-Optics and the European Quantum Electronics Conference* 17.23 (Nov. 2009), p. 20700. ISSN: 21622701. DOI: 10.1109/CLEOE-EQEC.2009.5191479. URL: https://www.osapublishing.org/abstract.cfm?URI=oe-17-23-20700 (cit. on p. 57).

[49] Israel Rocha-Mendoza, Wolfgang Langbein, Paola Borri, et al. “Single source coherent anti-Stokes Raman microspectroscopy using spectral focusing”. In: *Applied Physics Letters* 95.8 (Nov. 2009), pp. 800–808. ISSN: 00036951. DOI: 10.1063/1.3216073. URL: http://doi.wiley.com/10.1002/jrs.2264%20http://aip.scitation.org/doi/10.1063/1.3216073%20http://aip.scitation.org/doi/10.1063/1.3028346 (cit. on p. 57).

[50] Bi-Chang Chen, Jiha Sung, Xiaoxi Wu, et al. “Chemical imaging and microspectroscopy with spectral focusing coherent anti-Stokes Raman scattering”. In: *Journal of Biomedical Optics* 16.2 (2011), p. 021112. ISSN: 10833668. DOI: 10.1117/1.3533315. URL: http://biomedicaloptics.spiedigitallibrary.org/article.aspx?doi=10.1117/1.3533315 (cit. on p. 57).

[51] Paul J. Wrzesinski, Sukesh Roy, and James R. Gord. “Interference-free coherence dynamics of gas-phase molecules using spectral focusing”. In: *Optics Express* 20.21 (2012), p. 23390. ISSN: 1094-4087. DOI: 10.1364/OE.20.023390. URL: https://www.osapublishing.org/oe/abstract.cfm?uri=oe-20-21-23390 (cit. on p. 57).

[52] Esben Ravn Andresen, Pascal Berto, and Hervé Rigneault. “Stimulated Raman scattering microscopy by spectral focusing and fiber-generated soliton as Stokes pulse”. In: *Optics Letters* 36.13 (July 2011), p. 2387. ISSN: 0146-9592. DOI: 10.1364/OL.36.002387. URL: https://www.osapublishing.org/abstract.cfm?URI=ol-36-13-2387 (cit. on p. 57).

[53] Hope T. Beier, Gary D. Noojin, and Benjamin a. Rockwell. “Stimulated Raman scattering using a single femtosecond oscillator with flexibility for imaging and spectral applications”. In: *Optics Express* 19.20 (Sept. 2011), p. 18885. ISSN: 1094-4087. DOI: 10.1364/OE.19.018885. URL: https://www.osapublishing.org/oe/abstract.cfm?uri=oe-19-20-18885 (cit. on p. 57).

[54] Delong Zhang, Mikhail N. Slipchenko, and Ji Xin Cheng. “Highly sensitive vibrational imaging by femtosecond pulse stimulated raman loss”. In: *Journal of Physical Chemistry Letters* 2.11 (June 2011), pp. 1248–1253. ISSN: 19487185. DOI: 10.1021/jz200516n. URL: http://pubs.acs.org/doi/abs/10.1021/jz200516n%20http://pubs.acs.org/doi/10.1021/jz200516n (cit. on p. 57).

[55] Dan Fu, Gary Holtom, Christian Freudiger, et al. “Hyperspectral Imaging with Stimulated Raman Scattering by Chirped Femtosecond Lasers”. In: *The Journal of Physical Chemistry B* 117.16 (Apr. 2013), pp. 4634–4640. ISSN: 1520-6106. DOI: 10.1021/jp308938t. arXiv: NIHMS150003. URL: http://www.ncbi.nlm.nih.gov/pubmed/23256635%20http://pubs.acs.org/doi/abs/10.1021/jp308938t%20http://linkinghub.elsevier.com/retrieve/pii/S0734975011001534%20http://pubs.acs.org/doi/10.1021/jp308938t (cit. on p. 57).

[56] Ruoyu He, Zhiping Liu, Yongkui Xu, et al. “Stimulated Raman scattering microscopy and spectroscopy with a rapid scanning optical delay line”. In: *Optics Letters* 42.4 (Feb. 2017), p. 659. ISSN: 0146-9592. DOI: 10.1364/OL.42.000659. URL: https://www.osapublishing.org/abstract.cfm?URI=ol-42-4-659%20https://www.ncbi.nlm.nih.gov/pubmed/28198892 (cit. on pp. 57, 61, 112).

[57] Hermann A. Haus. “Theory of mode locking with a fast saturable absorber”. In: *Journal of Applied Physics* 46.7 (1975), pp. 3049–3058. ISSN: 00218979. DOI: 10.1063/1.321997 (cit. on p. 57).

[58] Herman A. Haus. “Mode-locking of lasers”. In: *IEEE Journal on Selected Topics in Quantum Electronics* 6.6 (2000), pp. 1173–1185. ISSN: 1077260X. DOI: 10.1109/2944.902165 (cit. on p. 57).

[59] E. B. Treacy. “Optical Pulse Compression With Diffraction Gratings”. In: *IEEE Journal of Quantum Electronics* 5.9 (1969), pp. 454–458. ISSN: 0018-9197. DOI: 10.1109/JQE.1969.1076303 (cit. on p. 63).

[60] P Lazaridis, G Debarge, and P Gallion. “Time-bandwidth product of chirped sech(2) pulses: application to phase-amplitude-coupling factor measurement.” In: *Optics letters* 20.10 (1995), pp. 1160–1162. ISSN: 0146-9592. DOI: 10.1364/OL.21.000164 (cit. on p. 66).

[61] Wayde N. Martens, Ray L. Frost, Janos Kristof, et al. “Raman spectroscopy of dimethyl sulphoxide and deuterated dimethyl sulphoxide at 298 and 77 K”. In: *Journal of Raman Spectroscopy* 33.2 (Feb. 2002), pp. 84–91. ISSN: 0377-0486. DOI: 10.1002/jrs.827. URL: http://doi.wiley.com/10.1002/jrs.827 (cit. on p. 71).

[62] F. Verluise, V. Laude, Z. Cheng, et al. “Amplitude and phase control of ultrashort pulses by use of an acousto-optic programmable dispersive filter: pulse compression and shaping”. In: *Optics Letters* 25.8 (Apr. 2000), p. 575. ISSN: 0146-9592. DOI: 10.1364/OL.25.000575. URL: https://www.osapublishing.org/abstract.cfm?URI=ol-25-8-575 (cit. on p. 73).

[63] Jzsef Seres, Alexander Müller, Enikö Seres, et al. “Sub-10-fs, terawatt-scale Ti:sapphire laser system”. In: *Optics Letters* 28.19 (Oct. 2003), p. 1832. ISSN: 0146-9592. DOI: 10.1364/OL.28.001832. URL: https://www.osapublishing.org/abstract.cfm?URI=ol-28-19-1832 (cit. on p. 73).

[64] D. Kaplan and P. Tournois. “Theory and performance of the acousto optic programmable dispersive filter used for femtosecond laser pulse shaping”. In: *Journal de Physique IV (Proceedings)* 12.5 (2002), pp. 69–75. ISSN: 1155-4339. DOI: 10.1051/jp4:20020098 (cit. on p. 73).

[65] Frédéric Verluise, Vincent Laude, Jean-Pierre Huignard, et al. “Arbitrary dispersion control of ultrashort optical pulses with acoustic waves”. In: *Journal of the Optical Society of America B* 17.1 (2000), p. 138. ISSN: 0740-3224. DOI: 10.1364/JOSAB.17.000138. URL: https://www.osapublishing.org/abstract.cfm?URI=josab-17-1-138 (cit. on pp. 73, 75).

[66] O Schubert, M Eisele, V Crozatier, et al. “Rapid-scan acousto-optical delay line with 34 kHz scan rate and 15 as precision”. In: *Optics Letters* 38.15 (Aug. 2013), p. 2907. ISSN: 0146-9592. DOI: 10.1364/OL.38.002907. URL: http://www.ncbi.nlm.nih.gov/pubmed/23903176%20https://www.osapublishing.org/abstract.cfm?URI=ol-38-15-2907 (cit. on pp. 80, 83).

[67] I Znakovskaya, E Fill, N Forget, et al. “Dual frequency comb spectroscopy with a single laser”. In: *Optics Letters* 39.19 (Oct. 2014), p. 5471. ISSN: 0146-9592. DOI: 10.1364/OL.39.005471. URL: http://www.ncbi.nlm.nih.gov/pubmed/25360905%20https://www.osapublishing.org/abstract.cfm?URI=ol-39-19-5471 (cit. on p. 80).

[68] Xavier Audier, Naveen Balla, and Hervé Rigneault. “Pump-probe microspectroscopy by means of an ultra-fast acousto-optics delay line”. In: *Optics Letters* 42.2 (Jan. 2017), p. 294. ISSN: 0146-9592. DOI: 10.1364/OL.42.000294. URL: https://www.osapublishing.org/abstract.cfm?URI=ol-42-2-294 (cit. on pp. 81, 83, 89).

[69] Eun Hee Lee. “A practical guide to pharmaceutical polymorph screening & selection”. In: *Asian Journal of Pharmaceutical Sciences* 9.4 (Aug. 2014), pp. 163–175. ISSN: 18180876. DOI: 10.1016/j.ajps.2014.05.002. URL: http://dx.doi.org/10.1016/j.ajps.2014.05.002%20https://linkinghub.elsevier.com/retrieve/pii/S1818087614000245 (cit. on p. 106).

[70] John Haleblian and Walter McCrone. “Pharmaceutical Applications of Polymorphism”. In: *Journal of Pharmaceutical Sciences* 58.8 (Aug. 1969), pp. 911–929. ISSN: 00223549. DOI: 10.1002/jps.2600580802. URL: http://linkinghub.elsevier.com/retrieve/pii/S0022354915369562 (cit. on p. 106).

[71] Sandro Heuke, Barbara Sarri, Alberto Lombardini, et al. “Dual-focus stimulated Raman scattering microscopy: a concept for multi-focus scaling”. In: *Optics Letters* 43.19 (Oct. 2018), p. 4763. ISSN: 0146-9592. DOI: 10.1364/OL.43.004763. URL: http://www.osapublishing.org/abstract.cfm?URI=ol-43-19-4763%7B%5C%%7D0Ahttps://www.osapublishing.org/abstract.cfm?URI=ol-43-19-4763%20https://www.osapublishing.org/abstract.cfm?URI=ol-43-19-4763 (cit. on p. 118).